Strål
säkerhets
myndigheten
Swedish Radiation Safety Authority

Authors: Digby D. Macdonald
Samin Sharifi-Asl
G.R. Engelhardt

Technical Note

2014:57

Issues in the Corrosion of Copper in a Swedish High Level Nuclear Waste Repository

Phase III. Role of Sulphide Ion in Anodic and Cathodic Processes -Research report

Report number: 2014:57 **ISSN:** 2000-0456
Available at www.stralsakerhetsmyndigheten.se

SSM perspektiv

Bakgrund

I Sverige planeras slutförvaringen av det använda kärnbränslet och metoden som har utvecklats kallas för KBS-3 och bygger på tre skyddsbarriärer: kopparkapslar, bentonitlera och det svenska urberget. I den aktuella KBS-3 utformningen, kommer det använda bränslet placeras i en insats av gjutjärn som finns i en 50 mm tjock kopparkapsel som ska deponeras i ett kristallint bergförvar i Forsmark på ett djup av ca 500 m. Gjutjärnsinsatsen ger mekanisk hållfasthet och strålskydd, medan kopparkapselns roll är att skydda mot korrosion. I utvärderingen av KBS-3-systemet är förståelsen för långtids-utveckling av processer som kan påverka kapseln, inklusive degradering via korrosion, mycket viktig.

Det nuvarande forskningsarbetet (fas III) är en fortsättning av de forskningsprojekt som utfördes i fas I och II, och syftar till att ge en bättre och noggrannare definition av de förutsättningar och de korrosionsprocesser som kan förekomma i förvaret under den planerade lagringsperioden på mer än 100 000 år.

De termodynamiska förutsättningarna för korrosion av koppar i vatten har definierats i våra tidigare projekt. För många praktiska ändamål är kopparn inte en ädelmetall, förutom möjligen i mycket rent vatten, som inte kommer att finnas i ett slutförvar. Det har visat sig att miljön i det föreslagna området för slutförvaret innehåller långt ifrån rent vatten; den innehåller korrosiva ämnen som kan aktivera kopparn mot korrosion. Därför anser Svensk Kärnbränslehantering AB (SKB) att, i miljöer som är relevanta för slutförvaret såsom den som finns i Forsmark, är koppar inte immunt. Förståelse för parametrarna som kan ha betydelse för korrosionshastigheten i relevant miljö för slutförvaret är således en viktig och komplicerad uppgift.

Förutsägelsen av degraderingsprocesser inklusive korrosion av kopparkapseln för tider som är experimentellt otillgängliga med en stor faktor (t.ex. över 10^3 till 10^6 år) är mycket viktigt vid bedömningen av robustheten hos konceptet för slutförvaring av det använda kärnbränslet.

Projektets syfte

Syftet med detta forskningsprojekt är att göra fullständiga mätningar av parametrarna som behövs för ”mixed potential model” (MPM) som kommer att användas för att uppskatta redoxpotentialen i slutförvaret samt korrosionspotentialen och korrosionshastigheten av kopparkapseln över hela den ”korrosionsevolutionära utvecklingen” (CEP) av förvaret. Dessa mätningar kommer att inkludera följande:

- Att undersöka de elektroniska egenskaperna hos den passiva filmen av sulfid som bildas på kopparytan
- Mätning av parametrar som igår i Point Defect Model, PDM, för bildandet av Cu_2S
- Mätning av upplösningshastigheten för den passiva Cu_2S-filmen på kopparytan

- Mätning av kinetiska parametrar för utvecklingen av väte från korrosion av koppar
- Fortsätta utveckla Mixed Potential-modellen
- Implementering av parametervärdena i Mixed potential-modellen
- Prediktering av redoxpotentialen, korrosionspotentialen, korrosionshastigheten och korrosion-relaterad degradering över hela den ”korrosionsevolutionära utvecklingen” (CEP) av förvaret.

Med hjälp av mera avancerade fysikaliska-elektrokemiska modeller kommer arbetet även ge möjlighet för att jämföra korrosionspotentialen och korrosionshastigheten för kopparkapseln med SKB:s senaste resultat.

Författarnas sammanfattning

De viktigaste resultaten från detta forskningsprojekt visar att:

1. För fallet när bentonitbufferten mellan kopparkapseln och berget är intakt, är risken för degradering av kapseln via allmänkorrosion försumbar och detta bör inte vara ett hot mot kapselns integritet under minst 100 000 år. Om bentonitbufferten är skadad och inte längre fungerar som en barriär samt om det finns direkt tillgång för korrosiva ämnen till kapselytan, t.ex. sulfider, skulle det kunna generera degradering av kapseln inom en period av upp till 48 000 år. Ett mycket osannolikt scenario inkluderar degradering av kapseln i fall med allvarligt skadat buffert/saknad buffert direkt efter deponering i kombination med hög temperatur vilket genererade en degraderingstid för kopparkapseln på upp till 8500 år. Detta resultat betonar vikten av det initiala tillståndet för alla barriärerna (granitiskt berget/initialtillståndet av deponeringshålet, bentonitbufferten och kopparkapseln) för att säkerställa långsiktig stabilitet av KBS-3 systemet.

2. Modellprognoser visar att i princip kan kapseln vara skyddad av en minskning av porositeten hos det yttre skiktet av den passiva filmen genom kompression orsakad av direkt inverkan av det växande korrosionsproduktskiktet mot bufferten. Modellberäkningar visar också att den tangentiella spänningen vid det yttre skiktet/bentonitgränssnittet kan bli större än draghållfastheten av bentoniten och sprickbildning av bentoniten kan inträffa. Sådan sprickbildning kan orsaka till exempel förekomst av ”genvägar” mellan kapseln och berget, som kan leda till accelererad korrosion av kapseln. Men alla uppskattningar som utfördes kan endast anses vara teoretiska till sin natur, eftersom inga experimentella data för de elastiska egenskaperna, initial porositet av bentoniten och yttre skikt av den passiva filmen i detta system har använts för att kontrollera resultatet av denna modell.

3. Det viktigaste resultatet av denna analys är att allmänkorrosion av kopparkapseln kan vara självbegränsande på grund av att kompressionen av det yttre skiktet av den passiva filmen och närområdets buffert samt porositeten hos en eller båda faser kommer att sjunka och bli noll och därigenom hindra tillträdet av vatten och sulfidjoner till kapselytan, som krävs för att korrosion ska fortsätta.

Behov av ytterligare forskning

Intressanta resultat skulle kunna uppnås genom att jämföra jämviktspotentialen med de kritiska potentialerna för olika lokaliserade korrosionsprocesser, såsom gropfrätning, spänningskorrosion och spaltkorrosion för att indikera om någon av dessa lokaliserade korrosionsprocesser kan förekomma i förvaret. För att kunna utföra en sådan jämförelse måste motsvarande modeller för att uppskatta de kritiska potentialerna för lokaliserade korrosionsprocesser utvecklas tillsammans med respektive experimentella undersökningar, alternativt att de kritiska potentialerna skulle kunna utvärderas via direkta mätningar.

Projektinformation

Kontaktperson på SSM: Clara Anghel
Diarienummer: SSM2012-481
Aktivitetsnummer: 3030044-09

SSM perspective

Background

The Swedish plan for disposal of High-Level Nuclear Waste (HLNW) implies the encapsulation of spent fuels and deposition of the canisters holding the spent fuel in a crystalline bedrock repository at a depth of about 500 m. In the current KBS-3 design, the spent fuel will be emplaced in an inner cast iron insert that is contained in a copper canister with a 50 mm wall thickness. The role of the cast iron insert is to provide mechanical strength as well as radiation shielding, while the copper canister's (the outer layer) role is to provide corrosion protection, thus for the evaluation of the performance of the KBS-3 system, understanding of the long-term development of the processes that can affect the canister including degradation via corrosion is very important.

The proposed work (Phase III) is a continuation of the research project performed in Phases I and II, in order to provide a better and more accurate definition of the conditions and the corrosion processes that could occur as the repository evolves over the planned storage period of more than 100,000 years.

The thermodynamic conditions for the corrosion of copper in water have been defined in previous projects. For many practical purposes copper is not a noble metal, except possibly in very pure water, which will not exist in a repository. It has been shown that the environment in the proposed repository is far from being pure water; it contains species that can activate copper towards corrosion. Thus the Swedish Nuclear Fuel and Waste Management Company, SKB, recognizes that, in representative repository environment, such as that which exists at Forsmark, copper is not immune. Understanding the parameters that could control the corrosion rate in relevant environment for the repository is thus an important and complex task. The prediction of degradation processes including corrosion damage for exposure periods that are experimentally inaccessible by a large factor (e.g., to over 10^3 to 10^6 years) is vitally important in assessing the robustness of the concept for the disposal of HLNW.

Objectives

The objectives of the proposed research work are the measurement of the full slate of parameters for the mixed potential models (MPMs) that will be used to estimate the redox potential of the repository, the corrosion potential and the corrosion rate of the copper canister in the repository over the corrosion evolutionary path (CEP). These measurements will include the following:

- Determination of Electronic Character of Cu_2S on Cu
- Measurement of Values for Parameters in the Point Defect Model, PDM, for the formation of Cu_2S
- Measurement of the Dissolution Rate of the Passive Cu_2S film on Copper
- Measurement of Kinetic Parameters for the Evolution of Hydrogen on Copper

- Continued Development of the Mixed Potential Models
- Insertion of the Parameter Values into the Mixed Potential Models
- Prediction of the Redox Potential, Corrosion Potential, Corrosion Rate, and Corrosion damage over the Corrosion Evolutionary Path.

Using more advanced physico-electrochemical models, the work will also yield the corrosion potential and the corrosion rate that can be compared with those predicted by SKB in their modeling program.

Summary of the results by the author

The most important findings of this research project show that:

1. In the case when the bentonite buffer between the copper canister and the granitic rock is not damaged, we can neglect the possibility of general corrosion damage being a threat to canister integrity over a 100,000 year storage period. However, if the bentonite buffer is damaged for any reason, and does not act as an engineered barrier, it is predicted that the direct access of sulphide species to the canister surface could degrade the canister within a period of up to 48,000 years. An analysis of a highly unlikely event considering high temperature degradation of the canister together with seriously damaged buffer/missing buffer directly after emplacement generated a degradation time of up to 8,500 years for the copper canister. This result highlights the importance of the initial state of all the barriers (the granitic rock / the initial condition of the deposition hole, the bentonite buffer and the copper canister) for the long term stability of the KBS-3 system.

2. Model predictions show that, in principle, the canister can be protected by the reduction of porosity of the outer layer of the passive film by compression caused by impingement of the growing corrosion product layer against the buffer. Model calculations show also that the tangential (hoop) stress on the outer layer/bentonite interface can become greater than the tensile strength of the bentonite and cracking of the bentonite may occur. Such cracking can cause, for example, the appearance of "shortcuts" between the canister and the rock, which might lead to accelerated corrosion. However, all estimates that were performed can be considered as being only "model" in nature, because no experimental data on the elastic properties and initial porosity of bentonite and outer layer of the passive film in this system have been used to verify the outcome of the model.

3. The most important finding of this analysis is that general corrosion of the copper canister may be self-limiting, because of the compression of the outer layer of the passive film and the near-field buffer, resulting in the porosity of one or both phases going to zero and thereby denying access of water and sulphide ion to the canister surface, which is required for continued corrosion.

Need for further research

Interesting results could be obtained by comparing the equilibrium potential with the critical potentials for various localized corrosion processes, such as pitting corrosion, stress corrosion cracking, and crevice corrosion, in order to indicate whether any of these localized corrosion processes are likely to occur in the repository. In order to perform such comparison, the corresponding models for estimating the critical potentials for the localized corrosion processes must be developed along with the respective experimental investigations or the critical potentials must be measured directly.

Project information

Contact person SSM: Clara Anghel
Reference number: SSM2012-481
Activity number: 3030044-09

Strål
säkerhets
myndigheten
Swedish Radiation Safety Authority

Authors: Digby D. Macdonald[1], Samin Sharifi-Asl[1] and G.R. Engelhardt[2]

[1] Department of Materials Science and Engineering
University of California at Berkeley
Berkeley, CA 94720, USA

[2] OLI Systems
108 American Rd.
Morris Plains, NJ 07950

Technical Note 72

2014:57

Issues in the Corrosion of Copper in a Swedish High Level Nuclear Waste Repository

Phase III. Role of Sulphide Ion in Anodic and Cathodic Processes -Research report

Date: November, 2014
Report number: 2014:57 **ISSN:** 2000-0456
Available at www.stralsakerhetsmyndigheten.se

This report was commissioned by the Swedish Radiation Safety Authority (SSM). The conclusions and viewpoints presented in the report are those of the author(s) and do not necessarily coincide with those of SSM.

Content

Abstract **3**

Introduction **4**

1. Anodic Reaction **9**

2. Cathodic Reactions **9**

3. Summary of Mixed Potential Model Parameter Values and Properties of Corroding Copper in Sulphide-Containing Simulated Repository Environments **11**

4. References **13**

Research Objectives **15**

Task 1: Determination of Electronic Character of Cu_2S on Cu **15**

Task 2: Measurement of Values for Parameters in the PDM for the Formation of Cu_2S **16**

Task 3: Measurement of the Dissolution Rate of the Passive Cu_2S Film on Copper **16**

Task 4: Measurement of Kinetic Parameters for the Evolution of Hydrogen on Copper **16**

Task 5: Continued Development of the Mixed Potential Models **17**

Task 6: Insertion of the Parameter Values into the Mixed Potential Models **17**

Task 7: Prediction of the Redox Potential, Corrosion Potential, Corrosion Rate, and Corrosion damage Over the Corrosion Evolutionary Path **17**

References **18**

Investigation of the Kinetics and Mechanism of the Hydrogen Evolution Reaction on Copper **19**

1. Introduction **19**

2. Experimental **20**

3. Results and Discussion **22**

3.1. Calculation of the electrochemical kinetic parameters 22
3.2. Effect of Temperature 23
3.3. Effect of Hydrogen Pressure 23
3.4. Effect of pH 25
3.5. Optimization 25
3.6. Effect of HS^- 28
3.7. Impedance Model 29
3.8. Extraction of Model Parameters Values from EIS data 33

4. Summary and Conclusions **40**

5. References **41**

Corrosion of Copper in Sodium Chloride Solution Containing Sulphide Species **43**

1. Introduction **43**

2. Experimental.....46

3. Results and Discussion 47

3.1. Potential-pH diagrams 47
3.2. Potentiodynamic polarization.....49
3.2.1. Effect of chloride concentration 49
3.2.2. Effect of temperature 50
3.2.3. Effect of sulphide concentration 51
3.3. Mott-Schottky Analysis 53
3.4. XPS Analysis of the Sulphide Passive Film on Copper 56
3.5. Electrochemical impedance spectroscopy 59
3.5.1. Validation of impedance data 59
3.5.2. Effect of Formation Potential 67
3.5.3. Effect of temperature 70
3.5.4. Effect of sulphide concentration 71
3.6. Impedance model: Point Defect Model 73
3.6.1. Calculation of $YF0$.....77
3.6.2. Calculation of $\boldsymbol{\Delta Ci0\Delta U}$.....78
3.6.3. Calculation of $\boldsymbol{\Delta CvL\Delta U}$ 79
By analogy it can be shown that:.....79
3.7. Extraction of model parameter values from EIS data.....81
3.8. Sensitivity Analysis 94

4. Summary and conclusions 96

5. References.....97

Estimation of Maximum Possible Values of Corrosion Current Density and Corrosion Potential under Conditions of Copper Corrosion in a Swedish High Level Nuclear Waste Repository 100

1. Introduction 100

1.1. Anodic reaction 100
1.2. Cathodic reactions 101
1.3. Homogeneous reactions.....101

2. Estimation of maximum possible value of corrosion current density …… 102

3. Estimation of maximum possible value of corrosion potential 112

4. Corrosion of copper in the confined space between the canister and the bentonite.....120

5. Summary and Conclusions.....124

6. References.....125

Abstract

The corrosion of pure copper in sulphide-containing aqueous solutions that are typical of crystalline rock repositories in Sweden and Finland for the isolation of High Level Nuclear Waste has been studied using potentiostatic and potentiodynamic polarization, Mott-Schottky analysis, and electrochemical impedance spectroscopy. The results, which are interpreted in terms of the Point Defect Model, indicate that a bi-layer sulphide film forms, comprising a p-type barrier layer of Cu_2S and probably an outer layer of CuS, which is n-type in electronic character. The outer layer is not observed to form at 25°C and at 50°C, but is observed to form intermittently at 75°C. Thus, the outer layer is unstable and frequently disappears from the surface by sloughing, resulting in large excursions of the corrosion potential. This phenomenon is found to induce considerable instability in the electrochemical response of the system, such as that under potentiodynamic polarization.

We have, in this study, also studied the effects of temperature, solution pH, and hydrogen pressure on the kinetics of hydrogen electrode reaction (HER) by means of steady-state polarization measurements on copper in borate buffer solution. In order to obtain electro-kinetic parameters, such as the exchange current density and cathodic Tafel slope, two stages of optimization have been performed. From the optimization process, the apparent activation energy (E_{ac}) of HER on copper was obtained as 32(kJ/mol). Moreover, the exchange current density $i_0(H_2)$ and the cathodic transfer coefficient were obtained on copper as a function of temperature, solution pH, and hydrogen pressure. Sulphide ion is found not to have a significant effect on the values of the electro-kinetic parameters of the HER, including the exchange current density and the Tafel constants.

Electrochemical impedance spectroscopic (EIS) studies of the HER on copper in borate buffer solution was carried out. The impedance spectra were modeled using a proposed mechanism based upon the Volmer-Heyrovsky-Tafel steps for hydrogen evolution and by considering the electrochemical adsorption of hydrogen atoms and hydroxyl groups onto the copper surface. By using mathematical optimization of the electro-kinetic model on the experimental impedance spectroscopic data, a single set of kinetic parameters, including the rate constants and transfer coefficients, has been proposed for each pH. The results reveal that HER might proceed through the Volmer-Heyrovsky-Tafel mechanism with the Volmer reaction being the rate determining step. A good correlation was achieved between the experimental and calculated steady-state current, as a function of potential showing the viability of the proposed mechanism. Sulphide ion is found not to have a significant effect on the mechanism and the values of the electro-kinetic parameters of the HER, including the exchange current density and the Tafel constants, as determined by EIS, in agreement with the electrochemical kinetic study referred to above.

Finally, the most important finding of this analysis is that general corrosion of the copper canister may be self-limiting, because of the compression of the outer layer of the passive film and the near-field buffer, resulting in the porosity of one or both phases going to zero and thereby denying access of water and sulphide ion to the canister surface, which is required for continued corrosion. Taking into account this phenomenon, it is likely that the corrosion of copper will become self-limiting and that the copper canisters will remain intact until the storage horizon of 100,000 years and, perhaps, much longer.

Introduction

In Phase II of this research program, which is currently underway, mixed potential models (MPMs) are being developed to predict the redox potential of the repository environment and the corrosion potential and corrosion rate (expressed as the corrosion current density) of copper canisters contained in the granitic rock repository being developed in Sweden for the disposal of high level nuclear waste (HLNW). These models are designed to provide estimates of E_{redox}, E_{corr}, and i_{corr} as the system evolves along the corrosion evolutionary path. Comparison of E_{redox} and E_{corr} with critical potentials for various localized corrosion processes, such as pitting corrosion, stress corrosion cracking, and crevice corrosion, is expected to indicate whether any of these localized corrosion processes are likely to occur in the repository. Integration of the corrosion current density and use of Faraday's law will yield the weight loss of copper and the dimensional change of the canister due to corrosion. The models being developed are known technically as "Mixed Potential Models (MPMs), which stem from the author's work [1] on modeling the heat transport circuits of boiling water (nuclear) reactors (BWRs), where they have been spectacularly successful in describing the electrochemical properties and corrosion behaviors of stainless steels in the primary coolant circuits.

Recognizing that copper metal loses much of its corrosion resistance in the presence of sulphide ion and other sulphur-containing species [2-7], with the metal forming Cu_2S,

$$2Cu + HS^- \rightarrow Cu_2S + H^+ + 2e^- \quad (1)$$

which has a sufficiently negative equilibrium potential that hydrogen evolution from the reduction of water becomes a viable cathodic reaction (see below).

$$H_2O + e^- = \frac{1}{2}H_2 + OH^- \quad (2)$$

The equilibrium potentials for these two reactions in the repository are readily calculated from the Nernst equations as

$$E_a^e = E_a^0 - \frac{2.303RT}{2F} log\left(\frac{a_{HS^-}}{a_{H^+}}\right) \quad (3)$$

and

$$E_c^e = E_c^0 - \frac{2.303RT}{F} log\left(p_{H_2}^{1/2} a_{OH^-}\right) \quad (4)$$

where a_i is the activity of Species i R is the universal gas constant (R = 8.3142 J/K.mol), and F is Faraday's constant (F = 96,487 C/equiv.). The full cell reactions for these two processes are given as

$$Cu_2S + H_2 = 2Cu + H^+ + HS^- \quad (5)$$

and

$$H_2O = H^+ + OH^- \quad (6)$$

Noting that the partial pressure of hydrogen in the repository is 7×10^{-9} bar and the pH is about 8, and using values for the standard potentials for the partial anodic reaction [Eq. (1) written in the reduction sense] and the partial cathodic reaction

[Reaction (2)] and the standard Gibbs energy changes for the full cell reactions, we are able to estimate the equilibrium potentials as presented in Table 1 and plotted in Figure 1.

Table 1. Changes in standard Gibbs energy and standard and equilibrium potentials for Reactions (1) and (2) as a function of temperature. p_{H_2} = 7×10^{-9} bar, pH = 8, [HS^-] = 1.39×10^{-5} M (0.5 ppm).

Reaction	T/°C	ΔG^0/kJ.mol^{-1}	E^0/V$_{she}$	E^e/V$_{she}$
$Cu_2S + H^+ + 2e^- = 2Cu + HS^-$	0	93.567	-0.485	-0.570
	25	96.192	-0.499	-0.592
	50	99.152	-0.514	-0.615
	75	102.391	-0.531	-0.640
	100	105.889	-0.549	-0.665
	125	109.649	-0.569	-0.693
$H_2O + e^- = 1/2H_2 + OH^-$	0	78.098	-0.810	-0.264
	25	79.855	-0.828	-0.232
	50	82.074	-0.851	-0.205
	75	84.650	-0.878	-0.182
	100	87.548	-0.908	-0.162
	125	90.761	-0.941	-0.145

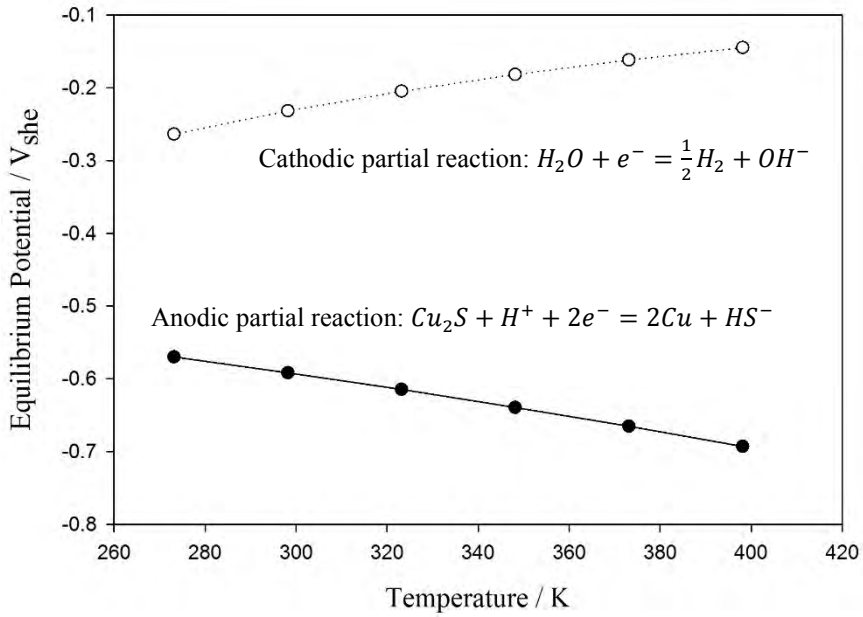

Figure 1. Plots of the equilibrium potentials for the partial anodic and cathodic reactions for the corrosion of copper in aqueous solution in the presence of sulphide ion.

Clearly, from Figure 1, the potential of the *Cu/Cu$_2$S* reaction is sufficiently negative that the hydrogen evolution reaction, Reaction (7), is thermodynamically viable, according to the criterion derived from the Second Law of Thermodynamics, which states that for a corrosion process to be viable then $E_a^e < E_{corr} < E_c^e$; that is, the corrosion potential must lie between the two lines plotted in Figure 1. Theory shows that the corrosion potential lies closest to the equilibrium potential for that partial process that is characterized by the highest exchange current density. We do not currently know the exchange current densities for the two partial reactions, so that it

is not yet possible to indicate where in the range defined by the two lines in Figure 1 the ECP might lie.

The Point Defect Model [8,9] representation of the formation of Cu_2S is given as:

Metal	Barrier Layer, Cu_2S	Solution/Precipitated Outer Layer
(1) $Cu + V_{Cu}^{1'} \overset{k_1}{\rightarrow} Cu_{Cu} + v_{Cu} + e^-$		(4) $Cu_{Cu} \overset{k_4}{\rightarrow} Cu_s^+ + V_{Cu}^{1'}$
(2) $Cu \overset{k_2}{\rightarrow} Cu_i^+ + v_{Cu} + e^-$		(5) $Cu_i^+ \overset{k_5}{\rightarrow} Cu_s^+$
(3) $Cu \overset{k_3}{\rightarrow} Cu_{Cu} + \frac{1}{2}V_S^{\circ\circ} + e^-$		(6) $V_S^{\circ\circ} + HS^- \overset{k_6}{\rightarrow} S_S + H^+$
		(7) $CuS_{1/2} + \frac{1}{2}H^+ \overset{k_7}{\rightarrow} Cu^+ + \frac{1}{2}HS^-$

Figure 2. Point Defect Model representation of the formation of Cu_2S on copper. Note that the Cu^+ cations that are transmitted through the barrier layer via cation vacancy movement through Reactions (1) and (4) and as interstitials via Reactions (2) and (5) will react with additional HS^- to form the precipitated, outer later with the overall stoichiometry being described by Reaction (13).

The rate constants for these reactions have been derived using the method of partial charges and the expressions are summarized in Tables 2 and 3 [8-10].

Table 2. Rate constants $\boldsymbol{k_i = k_i^0 e^{a_i V} e^{b_i L} e^{c_i pH}}$ for the interfacial defect generation and annihilation reactions employed in the Point Defect Model.

Reaction	$a_i(V^{-1})$	$b_i(cm^{-1})$	c_i
(1) $Cu + V_{Cu}^{1'} \overset{k_1}{\rightarrow} Cu_{Cu} + v_{Cu} + e^-$	$\alpha_1(1-\alpha)\gamma$	$-\alpha_1\varepsilon\gamma$	$-\alpha_1\beta\gamma$
(2) $Cu \overset{k_2}{\rightarrow} Cu_i^+ + v_{Cu} + e^-$	$\alpha_2(1-\alpha)\gamma$	$-\alpha_2\varepsilon\gamma$	$-\alpha_2\beta\gamma$
(3) $Cu \overset{k_3}{\rightarrow} Cu_{Cu} + \frac{1}{2}V_S^{\circ\circ} + e^-$	$\alpha_3(1-\alpha)\gamma$	$-\alpha_3\varepsilon\gamma$	$-\alpha_3\beta\gamma$
(4) $Cu_{Cu} \overset{k_4}{\rightarrow} Cu_s^+ + V_{Cu}^{1'}$	$\alpha_4\alpha\gamma$		$\alpha_4\beta\gamma$
(5) $Cu_i^+ \overset{k_5}{\rightarrow} Cu_s^+$	$\alpha_5\alpha\gamma$		$\alpha_5\beta\gamma$
(6) $V_S^{\circ\circ} + HS^- \overset{k_6}{\rightarrow} S_S + H^+$	$2\alpha_6\alpha\gamma$		$2\alpha_6\beta\gamma$
(7) $CuS_{1/2} + \frac{1}{2}H^+ \overset{k_7}{\rightarrow} Cu^+ + \frac{1}{2}HS^-$	0		0

Table 3. Definition of the standard rate constants for the interfacial defect generation and annihilation reactions employed in the Point Defect Model. Note that the base rate constant for the ith reaction is designated $\boldsymbol{k_i^{00}}$.

Reaction	k_i^0
(1) $Cu + V_{Cu}^{1'} \overset{k_1}{\rightarrow} Cu_{Cu} + v_{Cu} + e^-$	$k_1^{00} e^{-\alpha_1\gamma\varphi_{f/s}^0} e^{\frac{-E_{a,1}}{RT}\left(\frac{1}{T}-\frac{1}{T_0}\right)}$
(2) $Cu \overset{k_2}{\rightarrow} Cu_i^+ + v_{Cu} + e^-$	$k_2^{00} e^{-\alpha_2\gamma\varphi_{f/s}^0} e^{\frac{-E_{a,2}}{RT}\left(\frac{1}{T}-\frac{1}{T_0}\right)}$
(3) $Cu \overset{k_3}{\rightarrow} Cu_{Cu} + \frac{1}{2}V_S^{\circ\circ} + e^-$	$k_3^{00} e^{-\alpha_3\gamma\varphi_{f/s}^0} e^{\frac{-E_{a,3}}{RT}\left(\frac{1}{T}-\frac{1}{T_0}\right)}$
(4) $Cu_{Cu} \overset{k_4}{\rightarrow} Cu_s^+ + V_{Cu}^{1'}$	$k_4^{00} e^{-\alpha_4\gamma\varphi_{f/s}^0} e^{\frac{-E_{a,4}}{RT}\left(\frac{1}{T}-\frac{1}{T_0}\right)}$
(5) $Cu_i^+ \overset{k_5}{\rightarrow} Cu_s^+$	$k_5^{00} e^{\alpha_5\gamma\varphi_{f/s}^0} e^{\frac{-E_{a,5}}{RT}\left(\frac{1}{T}-\frac{1}{T_0}\right)}$
(6) $V_S^{\circ\circ} + HS^- \overset{k_6}{\rightarrow} S_S + H^+$	$k_6^{00} e^{2\alpha_6\gamma\varphi_{f/s}^0} e^{\frac{-E_{a,6}}{RT}\left(\frac{1}{T}-\frac{1}{T_0}\right)}$
(7) $CuS_{1/2} + \frac{1}{2}H^+ \overset{k_7}{\rightarrow} Cu^+ + \frac{1}{2}HS^-$	$k_7^{00} e^{\frac{-E_{a,7}}{RT}\left(\frac{1}{T}-\frac{1}{T_0}\right)}$

As noted elsewhere [10], the rate of change of the barrier layer thickness for a barrier layer that forms irreversibly on a metal or alloy surface can be expressed as

$$\frac{dL}{dt} = \Omega k_3^0 e^{a_3 V} e^{b_3 L} e^{c_3 pH} - \Omega k_7^0 \left(\frac{C_{H^+}}{C_{H^+}^0}\right)^n e^{a_7 V} e^{c_7 pH} \qquad (7)$$

where $a_3 = \alpha_3(1-\alpha)\gamma$, $a_7 = 0$, $b_3 = -\alpha_3 \varepsilon \gamma$, $c_3 = -\alpha_3 \beta \gamma$, and $c_7 = 0$ (Table 2). In these expressions, Ω is the mole volume of the barrier layer per cation, ε is the electric field strength within the barrier layer (postulated to be a constant and independent of the applied voltage in the steady state, because of the buffering action of Esaki tunneling [8,9]), k_i^0 and $\alpha_i$are the standard rate constant and transfer coefficient, respectively, for the appropriate reactions depicted in Figure 2 [i.e., Reactions (3) and (7)], α is the polarizability of the barrier layer/solution (outer layer) interface, (i.e., the dependence of the voltage drop across the interface, $\phi_{f/s}$, on the applied voltage, V), β is the dependence of $\phi_{f/s}$ on pH (assumed to be linear), $\gamma = F/RT$, C_{H^+} is the concentration of hydrogen ion, $C_{H^+}^0$ is the standard state concentration, and n is the kinetic order of the barrier layer dissolution reaction with respect to H^+. Note that the rate of the dissolution reaction is voltage dependent if the oxidation state of copper in the barrier layer were different from the oxidation state of copper in the solution. Under anoxic conditions, the oxidation state of copper in both phases is +1. Thus, the rate of dissolution is considered to be voltage independent.

By setting the left side of Eq. (7) equal to zero, the steady state thickness of the barrier layer, L_{ss}, is readily derived as

$$L_{ss} = \left[\frac{1-\alpha}{\varepsilon}\right] V + \left[\frac{2.303n}{\alpha_3 \varepsilon \chi \gamma} - \frac{\beta}{\varepsilon}\right] pH + \frac{1}{\alpha_3 \varepsilon \chi \gamma} ln\left(\frac{k_3^0}{k_7^0}\right) \qquad (8)$$

where the parameters are as previously defined. Note that in deriving these expressions, the convention has been adopted that, for the rate of barrier layer dissolution, $C_{H^+}$and $C_{H^+}^0$ have units of mol/cm^3, but when used for defining pH, the units are the conventional mol/l. Thus, the standard states for the dissolution reaction [second term on the right side of Eq. (7)] and for the pH are 1.0 mol/cm^3 and 1.0 mol/l, respectively. The introduction of a standard state into the dissolution rate renders the units of k_7^0 independent of the kinetic order, n, without altering the numerical value of the rate.

The steady state passive current density is readily derived [8-10] as:

$$I_{ss} = F\left[k_2^0 e^{a_2 V} e^{b_2 L_{ss}} e^{c_2 pH} + k_4^0 e^{a_4 V} e^{c_4 pH} + k_7^0 e^{a_7 V} e^{c_7 pH} \left(\frac{C_{H^+}}{C_{H^+}^0}\right)^n\right] \qquad (9)$$

where the first, second, and third terms arise from the generation and transport of cation interstitials, cation vacancies, and oxygen vacancies, respectively, with the term due to the latter being expressed in terms of the rate of dissolution of the barrier layer [1]. This expression is derived in part by noting that the fluxes of a given defect at the two defects under steady state conditions are equal; in this way the expression of the current can be formulated so as to avoid the defect concentrations at the interfaces. It is Eq. (9) that must be inserted into Eq. (8) to define the quantity i_a.

Because metal interstitials and oxygen vacancies are electron donors, and recognizing that the barrier later is a highly-doped, defect semi-conductor, the barrier layer will display n-type conductivity if either interstitials and/or oxygen vacancies are the dominant defects in the system. On the other hand, if the cation vacancy, which is an electron acceptor, dominates, the film will display p-type conductivity. With regard to Eq. (9), n-type conductivity would imply that the second or third terms

dominate the current, in which case the expression for the passive current density can be reduced to

$$I_{ss} = F\left[k_2^0 e^{a_2 V} e^{b_2 L_{ss}} e^{c_2 pH} + k_7^0 e^{a_7 V} e^{c_7 pH}\left(\frac{C_{H^+}}{C_{H^+}^0}\right)^n\right] \quad (10)$$

Noting that $a_7 = 0$ and that $a_2V + b_2L_{ss} = 0$, the passive current is predicted to be

$$I_{SS} = F\left[k_2^0 e^{c_2 pH} + k_7^0 e^{c_7 pH}\left(\frac{C_{H^+}}{C_{H^+}^0}\right)^n\right] \quad (11)$$

which is voltage-independent. On the other hand, if the film is p-type, then cation vacancies dominate and the expression for the passive current density reduces to

$$I_{SS} = F\left[k_4^0 e^{a_4 V} e^{c_4 pH} + k_7^0 e^{c_7 pH}\left(\frac{C_{H^+}}{C_{H^+}^0}\right)^n\right] \quad (12)$$

The electronic type of the Cu_2S passive film does not appear to have been determined, even though it is a straight forward matter to do so using Mott-Schottky analysis [8,9]. If the film was found to be n-type the passive current density, which would be incorporated into Eq. (8) would have the form

$$i_a = A \quad (13)$$

where, $A = F\left[k_2^0 e^{c_2 pH} + k_7^0 e^{c_7 pH}\left(\frac{C_{H^+}}{C_{H^+}^0}\right)^n\right]$ but if it is found to be p-type the functional form would be:

$$i_a = Ae^{a_4 V} + B \quad (14)$$

where $A = Fk_4^0 e^{c_4 pH}$ and $B = Fk_7^0 e^{c_7 pH}\left(\frac{C_{H^+}}{C_{H^+}^0}\right)^n$. In both cases, the current must go to zero at the equilibrium potential for the partial anodic process. Substituting these expressions into Eq. (8) and assuming, as a first approximation, that under anoxic conditions the only important cathodic partial reaction is hydrogen evolution via water reduction, we obtain the following:

$$A - \frac{e^{(V-E_{HER}^e)/b_a} - e^{-(V-E_{HER}^e)/b_c}}{\frac{1}{i_{0,R/O}} + \frac{e^{(V-E_{HER}^e)/b_a}}{i_{l,f,R/O}} - \frac{e^{-(V-E_{HER}^e)/b_c}}{i_{l,r,R/O}}} = 0 \qquad \text{(n-type)} \quad (15)$$

and

$$Ae^{a_4 V} + B - \frac{e^{(V-E_{HER}^e)/b_a} - e^{-(V-E_{HER}^e)/b_c}}{\frac{1}{i_{0,R/O}} + \frac{e^{(V-E_{HER}^e)/b_a}}{i_{l,f,R/O}} - \frac{e^{-(V-E_{HER}^e)/b_c}}{i_{l,r,R/O}}} = 0 \qquad \text{(p-type)} \quad (16)$$

These equations can be solved iteratively to yield $V = E_{corr}$. More sophisticated models may be devised by including additional cathodic reactions in the model, in which case the CoC becomes:

$$A - \sum_{i=l}^{N} \frac{e^{(V-E^e_{HER})/b_a} - e^{-(V-E^e_{HER})/b_c}}{\frac{1}{i_{0,R/O}} + \frac{e^{(V-E^e_{HER})/b_a}}{i_{l,f,R/O}} - \frac{e^{-(V-E^e_{HER})/b_c}}{i_{l,r,R/O}}} = 0 \quad \text{(n-type)} \qquad (17)$$

and

$$Ae^{a_4 V} + B - \sum_{i=l}^{N} \frac{e^{(V-E^e_{HER})/b_a} - e^{-(V-E^e_{HER})/b_c}}{\frac{1}{i_{0,R/O}} + \frac{e^{(V-E^e_{HER})/b_a}}{i_{l,f,R/O}} - \frac{e^{-(V-E^e_{HER})/b_c}}{i_{l,r,R/O}}} = 0 \quad \text{(p-type)} \qquad (18)$$

where the cathodic term is summed over the *N* cathodic reactions in the system.
For estimating the redox potential ($E_{redox} = E_h$), the equation that needs to be solved is:

$$\sum_{i=l}^{N} \frac{e^{(V-E^e_{HER})/b_{a,i}} - e^{-(V-E^e_{HER})/b_{c,i}}}{\frac{1}{i_{0,R/O,i}} + \frac{e^{(V-E^e_{HER})/b_{a,i}}}{i_{l,f,R/O,i}} - \frac{e^{-(V-E^e_{HER})/b_{c,i}}}{i_{l,r,R/O,i}}} = 0 \qquad (19)$$

assuming that the substrate is inert (e.g., gold). The authors note that it is common practice in the geochemical arena to estimate the redox potential using the Nernst equation. This procedure is incorrect, unless a single redox reaction dominates the electrochemistry of the system and that reaction is demonstrably at equilibrium. In the more general case, two or more redox reactions contribute to determining the potential and the potential is a mixed potential, not an equilibrium potential, as has been argued elsewhere [1].

1. Anodic Reaction

It is evident that, in order to solve for the corrosion potential using Eq. (18) it is necessary to know the values for A, B, and a_4, which are defined above, but which are repeated here for convenience.

$$A = F\left[k_2^0 e^{c_2 pH} + k_7^0 e^{c_7 pH}\left(\frac{C_{H^+}}{C^0_{H^+}}\right)^n\right] \qquad \text{(n-type film)} \qquad (20)$$

$$A = F k_4^0 e^{c_4 pH} \qquad \text{(p-type film)} \qquad (21)$$

$$B = F k_7^0 e^{c_7 pH}\left(\frac{C_{H^+}}{C^0_{H^+}}\right)^n \qquad \text{(n- and p-type film)} \qquad (22)$$

These terms contain the parameters k_2^0, k_7^0, k_4^0, c_2, c_4, c_7, and n. No data are available for these parameters in the scientific literature. The parameter values are, however, readily measured using electrochemical impedance spectroscopy (EIS), and a proposal to SSM is being prepared to do exactly that. Thus, complete prediction of the corrosion potential must await the measurement of those values.

2. Cathodic Reactions

A search of the literature revealed that there is little information available that can be used to calculate the corrosion potential, E_{corr}. While a great deal of data are available for the electrochemical dissolution of copper in chloride-containing media and while significant studies of the electrochemistry of copper in sulphide-containing aqueous have been reported, particularly by Shoesmith and co-workers [3-6] and

King [7], few of these data are directly relevant. For example, it is apparent that no Mott-Schottky analyses or photo-electrochemical studies have been performed to determine the electronic character of the Cu_2S film on copper in slightly-alkaline, sulphide-containing aqueous media, which are required to identify the dominant defect in the film and hence to choose between Eqs. (15) and (16) for calculating the corrosion potential and hence the corrosion rate. Furthermore, the state of knowledge of the hydrogen evolution reaction on copper in relevant environments is very poor. Thus, the exchange current density for the HER in neutral/alkaline solutions, $H_2O + e^- \leftrightarrow \frac{1}{2}H_2 + OH^-$, is written from electrochemical theory [11] as:

$$i_0 = i_0^0 C_{H_2}^{1-\alpha} C_{OH^-}^{\alpha} \quad (23)$$

where α is the transfer coefficient. The value for α is currently not known in the relevant environments, nor is the value of the standard exchange current density, i_0^0. Without these data, which must be determined experimentally, it is not possible to accurately calculate the exchange current density which is used in the MPM to estimate the redox potential, the corrosion potential, and the corrosion current density. Likewise, no data are available for the parameters in the PDM for copper. These data can only be obtained by optimizing the theoretical impedance expression obtained from the PDM on experimental electrochemical impedance data measured over a wide frequency range and at various voltages within the passive range, as we have done previously for a number of other metals and alloys (e.g., Fe [12]). These data must be determined experimentally in carefully designed experiments that faithfully emulate the physico-chemical characteristics of the system and that are amenable to quantitative analysis in order to extract quantitative data.

The limiting current densities, $i_{l,f,R/O,i}$ and $i_{l,r,R/O,i}$ are calculated assuming diffusion limitation in a porous medium (the bentonite buffer). The diffusion limit corresponds to the situation where the concentration of the reactant at the canister surface is equal to zero, corresponding to the situation where every water molecule that reached the surface is immediately reduced to hydrogen. Thus, for the forward and reverse directions are, respectively:

$$i_{l,f,R/O,i} = 2F\widehat{D}_{H_2} C_{H_2}^{b/r} / L_B \quad (24)$$

and

$$i_{l,r,R/O,i} = 2F\widehat{D}_{H_2O} C_{H_2O}^{b/r} / L_B \quad (25)$$

where $\widehat{D}_i$ is the diffusivity of the indicated species in the porous buffer, $C_{H_2O}^{b/r}$ is the concentration of water at the buffer/rock interface (0.0555 mol/cm^3), L_B is the thickness of the buffer (38 cm), and $C_{H_2}^{b/}$ is the concentration of water at the buffer/rock interface (10^{-8} mol/cm^3). The diffusivities for H_2O and H_2 are given by the theory of mass transport in porous media as

$$\widehat{D}_i = D_i^0 \frac{\hat{\varepsilon}}{\tau^2} \quad (26)$$

where D_i^0 is the diffusivity in bulk water, $\hat{\varepsilon}$ is the porosity, and τ is the tortuosity factor. Values for $\frac{\hat{\varepsilon}}{\tau^2}$ for saturated bentonite are about 10^{-3}. Noting that the self diffusion coefficient for H_2O in bulk water and that for molecular hydrogen in water are 3×10^{-5} cm^2/s and 5×10^{-5} cm^2/s], respectively, we estimate the diffusivities of these species in the buffer as 3×10^{-8} cm^2/s and 5×10^{-8} cm^2/s, respectively. Thus, the limiting current densities for the forward and reverse directions of the HER [Reac-

tion (7)] are estimated to be 2.98×10^{-5} A/cm^2 and 1.52×10^{-12} A/cm^2, respectively. The latter value is probably several orders too low, because it is based upon a simple self-diffusion model and ignores convection in the pores induced by the consumption of water at the copper surface. Defining realistic values for the limiting currents will be a major goal of the project.

Due to the lack of appropriate input data, particularly with respect to the kinetic parameters for the evolution of hydrogen, the reduction of oxygen, and the electrodissolution of copper in the presence of sulphide it was not possible to perform meaningful simulations of the redox potential of the repository and the corrosion potential of the canister upon completion of Phase II of this program. It is for this reason that a proposal was submitted to SSM to measure these data and a significant body of data has already been obtained.

3. Summary of Mixed Potential Model Parameter Values and Properties of Corroding Copper in Sulphide-Containing Simulated Repository Environments

In Table 4, we summarize the data related to the Mixed Potential Model in this study. These parameters comprise those for the hydrogen evolution reaction, representing the cathodic process under anoxic conditions, and the Point Defect Model, which describes the partial anodic process.

Table 4. Summary of Mixed Potential Model Parameter Values and Properties of Corroding Copper in Sulphide-Containing, Simulated Repository Environments.

Parameter	Value	Conditions	Units	Comments
$E^{o}_{HER,}$, Standard potential for the HER.	0	At all temperatures.	V	Defined by thermodynamics
E^{e}_{HER}, Equilibrium potential for the HER.	Variable	Depends on T, pH, and p_{H2}.	V	Calculated from the Nernst Eq.
i^{0}_{0}, standard exchange current density	Variable	Depends on T, pH and p_{H2}.	A/cm^2	Measured in this work.
i_0, Exchange current density.	Variable as calculated from i^{0}_{0}.	Depends on T, pH and p_{H2}	A/cm^2	Obtained from this study.
α, β, Tafel Constants for HER	Variable.	Depends on T.	V^{-1}	Obtained from this study.
Effective diffusivities of H^+, Cu^+, HS^-, and H_2 in Bentonite.	Variable.	Depends on T. and on the porosity and tortuosity of the bentonite buffer.	cm^2/s	Obtained from the literature.
Porosity and tortuosity of bentonite.	Variable.	Depends on density and degree of hydration of bentonite, temperature.	None	Obtained from the literature.
Rate constants for reactions in PDM.	Variable	Depends on temperature.		Obtained by optimization of PDM on EIS data.
Transfer coefficients for reactions in PDM.	Variable	Depends on temperature.		Obtained by optimization of PDM on EIS data.
α, polarizability of f/s interface.		Constant.	None	Obtained by optimization of PDM on EIS data.
β, Dependence of potential drop across f/s interface on pH.		Constant.	V	Obtained by optimization of PDM on EIS data.
ε, electric field strength	1 – 5×10^6	Constant.	V/cm	Obtained by optimization of PDM on EIS data.
$\varphi^{0}_{f/s}$, value of φf/s under standard conditions	± 1	Constant	V	Obtained by optimization of PDM on EIS data.
Identity of crystallographic defect type	Cation and oxygen vacancies, and metal interstitials	Depends on system.	None	Mott-Schottky analysis.
Defect concentration	Variable.	Depends on T.	#/cm^3	Mott-Schottky analysis.
i_{ss}, passive current density.	Variable.	Depends on T, V, pH, $[S^{2-}]$, and possibly on $[Cl^-]$.	A/cm^2	Experiment and by optimization of PDM on EIS data.
L_{bl}, thickness of barrier layer.	Variable.	Depends on T, V, pH, $[S^{2-}]$, and possibly on $[Cl^-]$.	cm	Experiment and by optimization of PDM on EIS data.
L_{ol}, thickness of outer layer	Variable.	Depends on T, V, pH, $[S^{2-}]$, and possibly on $[Cl^-]$.		Experiment and by optimization of PDM on EIS data.
σ, Warburg coefficient for defect transport.	Variable	Depends on T.	Ω.s$^{1/2}$	Optimization of PDM on EIS data.
D, defect diffusivity.	Variable.	Depends on T.	cm^2/s	Estimated from the Warburg coefficient.

Table 5. Typical parameters values obtained by the optimization of the PDM model on experimental impedance data for carbon steel in saturated solution of $Ca(OH)_2$ + $NaOH$, pH 13.5 after 128 days at 80°C as a function of applied potential.

E_{app} (V_{SHE})	-0.07	0.13	0.33	0.53	0.63
Current density (A.cm^{-2})	1.66×10^{-6}	6.57×10^{-7}	8.44×10^{-7}	1.77×10^{-6}	1.60×10^{-6}
Thickness of barrier layer (nm)	1.23	1.72	1.83	1.94	2.17
CPE-Y (S.sec$^{\alpha}$.cm^{-2})	3.46×10^{-5}	2.87×10^{-5}	2.87×10^{-5}	2.30×10^{-5}	2.36×10^{-5}
CPE-α	0.89	0.89	0.90	0.89	0.89
Electric field (ε)	3×10^{6}	3×10^{6}	3×10^{6}	3×10^{6}	3×10^{6}
Warburg coefficient (σ)	2.18×10^{4}	3.27×10^{5}	2.15×10^{5}	2.83×10^{4}	5.47×10^{4}
D (cm^2.s^{-1})	2.21×10^{-17}	7.81×10^{-16}	5.56×10^{-16}	4.25×10^{-17}	1.30×10^{-16}
Polarizability of the BOI (α)	0.724	0.724	0.724	0.724	0.724
Transfer coeff. reaction 1 (α_1)	0.10	0.19	0.18	0.17	0.12
Transfer coeff. reaction 2 (α_2)	0.08	0.02	0.06	0.02	0.05
k^0_1 (mol.cm^{-2}.s^{-1})	1.65×10^{-12}	1.41×10^{-12}	1.26×10^{-12}	1.82×10^{-12}	3.98×10^{-12}
k^0_2 (mol.cm^{-2}.s^{-1})	5.15×10^{-16}	5.20×10^{-16}	6.37×10^{-16}	4.50×10^{-16}	8.57×10^{-16}
k^0_5 (mol.cm^{-2}.s^{-1})	3.32×10^{-9}	2.40×10^{-9}	2.53×10^{-9}	2.36×10^{-9}	3.28×10^{-9}
R_s (ohm.cm^2)	7.9	9.87	9.1	7.7	9.9
$\Phi^0_{f/s}$	-0.1	-0.1	-0.1	-0.1	-0.1
β	-0.03	-0.03	-0.03	-0.03	-0.03
C_{dl} (F.cm^{-2})	4.41×10^{-7}	5.99×10^{-7}	1.88×10^{-7}	2.00×10^{-6}	1.17×10^{-6}
R_{ct} (ohm.cm^2)	1.35×10^{9}	1.31×10^{9}	1.45×10^{9}	2.29×10^{9}	3.48×10^{9}

4. References

1. D. D. Macdonald. "Viability of Hydrogen Water Chemistry for Protecting In-Vessel Components of Boiling Water Reactors". *Corrosion*, **48**(3), 194-205 (1992).

2. D. D. Macdonald and S. Sharifiasl, "Is Copper Immune When in Contact With Water and Aqueous Solutions", TR 2011:09, SSM, Stockholm, Sweden, 2011, Phase I report

3. J. Smith, Z. Qin, F. King, L. Werme, and D. W. Shoesmith, "The electrochemistry of copper in aqueous sulphide solutions"**,** Scientific *Basis for Nuclear Waste Management XXIX. Symposium (Materials Research Society Symposium Proceedings* **932**, 869-75 (2006).

4. J. Chen, Z. Qin, and D. W. and Shoesmith, "Rate controlling reactions for copper corrosion in anaerobic aqueous sulphide solutions", *Corrosion Engineering Science and Technology*, **46**(2), 138-141 (2011).

5. J. Smith, Z. Qin, D. W. Shoesmith, F. King, and L. Werme, “Source: Corrosion of copper nuclear waste containers in aqueous sulphide solutions”**,** *Scientific Basis for Nuclear Waste Management XXVII (Materials Research Society Symposium Proceedings Vol.824)*, p 45-50, 2004

6. J. Chen, Z. Qin, and D. W. Shoesmith, “Long-term corrosion of copper in a dilute anaerobic sulphide solution”**,** *Electrochimica Acta*, **56**(23), 7854-7861 (2011).

7. F. King, L. Ahonen, C. Taxén, U. Vuorinen, L. Werme, **“**Copper corrosion under expected conditions in a deep geologic repository”, Swedish Nuclear Fuel and Waste Management Co., Report, Technical Report, SKB TR-01-23 (2001).

8. D. D. Macdonald, “Passivity: The Key to Our Metals-Based Civilization”, *Pure Appl. Chem*., **71**, 951-986 (1999).

9. D. D. Macdonald. “The Point Defect Model for the Passive State”. *J. Electrochem. Soc*., **139**(12), 3434-3449 (1992).

10. D. D. Macdonald. “On the Existence of our Metals-Based Civilization: I. Phase Space Analysis,” *J. Electrochem. Soc.*, **153**(7), B213 (2006).

11. D. D. Macdonald, “Transient Techniques in Electrochemistry”, Plenum Press, NY, 1977.

12. J. Liu, B. M. Marx and D. D. Macdonald. "Analysis of Electrochemical Impedance Data for Iron in Borate Buffer Solutions," *Nuclear Waste Management: Accomplishments of the Environmental Management Science Program*, Wang, P., Zachry, T., Eds.; ACS Symposium Series 943; American Chemical Society: Washington, DC, (2006).

Research Objectives

The objectives of the proposed research are the measurement of the full slate of parameters for the mixed potential models (MPMs) that will be used to estimate the redox potential of the repository and the corrosion potential and the corrosion rate of the copper canister in the repository over the corrosion evolutionary path. These measurements will include the following:

- Determination of Electronic Character of Cu_2S on Cu
- Measurement of Values for Parameters in the Point Defect Model, PDM, for the Formation of Cu_2S
- Measurement of the Dissolution Rate of the Passive Cu_2S Film on Copper
- Measurement of Kinetic Parameters for the Evolution of Hydrogen on Copper
- Continued Development of the Mixed Potential Models
- Insertion of the Parameter Values into the Mixed Potential Models
- Prediction of the Redox Potential, Corrosion Potential, Corrosion Rate, and Corrosion damage Over the Corrosion Evolutionary Path.

Details of these activities are given below.

The proposed, Phase III work follows on that accomplished in Phases I and II, in order to provide a better and more accurate definition of the conditions and the corrosion processes that are expected to exist as the repository evolves over the planned storage period of more than 100,000 years. Using more advanced physico-electrochemical models, the work will also yield the corrosion potential and the corrosion rate that can be compared with those predicted by SKB in their modeling program [1].

Task 1: Determination of Electronic Character of Cu_2S on Cu

Our initial task will be to determine the general electrochemical behavior of copper in contact with sulphide-containing, simulated repository water, followed by performing Mott-Schottky analyses to ascertain the electronic type of the Cu_2S passive film on copper. This will be done by using two methods; (1) By measuring the capacitance of the interface at a suitably high frequency as a function of voltage under steady-state conditions, and; (2) By growing the film to a steady-state at a constant "film formation", followed by sweeping the potential in the negative direction, while measuring the capacitance via a superimposed sinusoidal voltage excitation. The voltage sweep rate will be sufficiently high that neither the thickness of the film, nor the distribution of defects will change perceptibly during the time of measurement. These latter measurements will be made for film formation potentials that span the passive range. By plotting C^{-2} versus V we will be able to ascertain whether the film is n-type or p-type and identify the dominant defects (cation vacancies for p-type and copper interstitials and/or oxygen vacancies for n-type). It is likely, as in the case of Cu_2O on Cu that the electronic type will change with volt-

age. Determining the electronic type is essential, because it is the only way of ascertaining what defects should be incorporated into the model.

Task 2: Measurement of Values for Parameters in the PDM for the Formation of Cu_2S

By using wide-band (10^4 Hz to 10^{-3} Hz) electrochemical impedance spectroscopy (EIS) and by optimizing the theoretical expression for the impedance derived from the PDM (the "object function") on the experimental impedance data, we will ascertain values for all of the unknown parameters for the PDM for the passive Cu_2S film on *Cu*. This procedure will follow exactly our current studies of the passive state for iron, where we have used this procedure with great success. These studies will be carried out as a function of the voltage across the passive range and as a function of pH and sulphide concentration. All impedance data will be validated using the Kramers-Kronig transformations.

Task 3: Measurement of the Dissolution Rate of the Passive Cu_2S Film on Copper

Over the past few years, we have developed a sensitive method for measuring the dissolution rate of the passive film on metals. This method relies upon measuring the capacitance of the film while simultaneously stepping the potential in the negative direction, in order to shut down growth of the film into the metal via Reaction (3), Figure 1. By calculating the thickness of the film (L) from the measured capacitance using the parallel plate capacitance expression, it is possible to obtain L as a function of time. The film thins, because of continues dissolution of the film at the film/solution interface and hence the rate can be determined. This method is capable of determining dissolution rates as low as 10^{-5} nm/s.

Task 4: Measurement of Kinetic Parameters for the Evolution of Hydrogen on Copper

In this task, we will measure the kinetic parameters for the reduction of water to evolve hydrogen. The parameters, the exchange current density, i_0, the forward and reverse transfer coefficients, and the kinetic orders with respect to the reactants and products. These data will be measured using rotating ring-disk voltammetry, in the presence of sulphide to detect any catalysis, if it exists, and will be measured at temperatures from 25°C to 90°C, in order to derive activation energies. These data will be used to derive standard exchange current densities. In this task, we will also develop more realistic methods for estimating the limiting current densities for the forward and reverse directions of the hydrogen electrode reaction. This will be done

by employing more sophisticated models for mass transport in porous media, taking into account pore flow and diffusion.

Task 5: Continued Development of the Mixed Potential Models

The current mixed potential models (MPMs) being developed for estimating the redox potential of the repository environment and the corrosion potential and corrosion rate of copper in that environment will continue to be developed in the light of the data obtained in this study. For example, if it is found that the Cu_2S passive film is p-type that will require a different treatment of the passive state than if it is found to be n-type, as embodied in Eqs. (24) and (25), respectively. If Cu_2S is like Cu_2O, it may be necessary to tailor the model to different potential ranges across the passive range, because the electronic type may change as a function of voltage (e.g., Cu_2O is found to be p-type, then n-type, and back to p-type as the voltage is increased)

Task 6: Insertion of the Parameter Values into the Mixed Potential Models

In this penultimate task, we will convert the data into a form that is required for use by the MPMs. Thus, the data may be included as input vectors or matrices or may be expressed as empirical equations (e.g., as Arrhenius' equation for rate constant versus temperature data).

Task 7: Prediction of the Redox Potential, Corrosion Potential, Corrosion Rate, and Corrosion damage Over the Corrosion Evolutionary Path

This final task will entail using the MPMs to calculate the redox potential of the repository environment and the corrosion potential and corrosion rate of copper in that environment over the corrosion evolutionary path. The calculated data will be compared with experimentally-measured data, where possible. We will also perform sensitivity studies to identify those model parameters that have the greatest impact on the calculated redox potential of the repository environment and the corrosion potential and corrosion rate of copper in that environment. Finally, a comparison will be made with the same data predicted by SKB and we will attempt to reconcile any differences as well as to articulate the consequences for corrosion damage to the canister because of the differences.

References

1. J. Smith, Z. Qin, D. W. Shoesmith, F. King, and L. Werme, "Source: Corrosion of copper nuclear waste containers in aqueous sulphide solutions"**,** *Scientific Basis for Nuclear Waste Management XXVII (Materials Research Society Symposium Proceedings,* **824**, 45-50 (2004).

Investigation of the Kinetics and Mechanism of the Hydrogen Evolution Reaction on Copper

1. Introduction

The hydrogen electrode reaction (HER) is one of the most thoroughly studied of electrochemical processes [1-4]. However, the reported experimental data from different groups do not agree very well, and the mechanisms for some systems are not completely understood. Since cathodic hydrogen evolution is a heterogeneous reaction, the state of the electrode surface plays a dominant role in determining the kinetics of the reaction. This reaction plays an important role on the corrosion of metals in acidic solution [5-9] as well as on the fuel side of H_2-air fuel cells. Among different electrochemical techniques, electrochemical impedance spectroscopy (EIS) undoubtedly is the most powerful tool for exploring the mechanisms of electrode reactions and for extracting values for the related kinetic parameters. In the last two to three decades, many research articles have been published on the mechanism of the hydrogen electrode reaction (HER) on materials that have shown promise as electro-catalysists of the HER, such as nickel [10], platinum [11], nickel-aluminum alloys [12], nickel-zinc alloys [2], etc. However, the only mechanistic study of the HER on copper is the classical work of Bockris et al. in both acidic and alkaline aqueous media [13].

Historically, the mechanism of the HER is regarded as being quite simple and comprises following steps:

(1) Electrochemical adsorption of hydrogen (Volmer reaction)

$$H^+ + M + e^- \rightleftharpoons MH(ads) \quad \text{(in acidic solution)} \qquad (1)$$

or

$$H_2O + M + e^- \rightleftharpoons MH(ads) + OH^- \quad \text{(in alkaline solution)} \qquad (2)$$

(2) Electrochemical desorption (Heyrovsky reaction)

$$MH(ads) + H^+ + e^- \rightleftharpoons M + H_2 \quad \text{(in acidic solution)} \qquad (3)$$

or

$$MH(ads) + H_2O + e^- \rightleftharpoons M + H_2 + OH^- \quad \text{(in alkaline solution)} \qquad (4)$$

(3) Chemical desorption (Tafel reaction)

$$2MH(ads) \rightleftharpoons M + H_2 \qquad (5)$$

As a result, the rate of the reaction (or the exchange current density) should depend on the energy of *H* adsorption on the given metal [14].

Copper has been selected as the material for fabricating the canisters for isolating high-level nuclear waste (HLNW) in Sweden's HLNW repository. It is postulated that, during the anoxic period, as a result of the presence of sulphide ions at the canister surface, the corrosion potential of the system will shift to more negative values than the hydrogen electrode reaction (HER) equilibrium potential under the prevailing conditions of temperature, pH, and partial pressure of hydrogen. This is due to the fact that sulphide activates copper, giving rise to an anodic process (Cu/Cu_2S) at a potential that is more negative than the HER equilibrium potential, thereby rendering hydrogen evolution to be a viable cathodic partial reaction in copper corrosion. Therefore, knowledge of the kinetic parameters for the reduction of water (evolution of hydrogen, HER) and its mechanism on the copper surface is vital for identifying those factors that control the kinetics of the overall corrosion reaction and that determining the evolution of the corrosion potential. The prediction of the electrochemical corrosion potential (ECP) depends on a number of parameters that arise from various physicochemical processes that are predicted to occur in the system. Since most of these parameters cannot be calculated theoretically, their values must be derived experimentally. The principal parameters needed for the calculation of the ECP during the anoxic period are the exchange current densities, $i_0(H_2)$, and the Tafel constants for the HER, and for the anodic oxidation of copper.

It is generally accepted that pH, temperature and H_2 gas pressure [15-19] are the most important factors governing the kinetics of the HER. Therefore, in this study, in order to obtain the electrokinetic parameters of the HER on copper, we conducted potentiostatic polarization experiments using a rotating disk electrode (RDE) as a function of temperature, pH and hydrogen pressure. An analytical expression describing the kinetics of the HER reaction on copper has been proposed and the kinetic parameters for the reactions have been extracted from simulating the impedance response of the system based upon the proposed model.

2. Experimental

The electrochemical measurements were performed in a conventional three-electrode cell (double walled, in order to maintain constant temperature of the test medium with a water inlet and outlet connected to a thermostatic bath), using a rotating disk working electrode (*Pine Instruments*®, area = 0.283 cm^2) made from pure copper rod (*Puratronic*®, 99.999% *Alfa Aesar*®). A *Ag/AgCl*(4 M *KCl*) and *Pt* wire were employed as reference and counter electrodes, respectively. The reference electrode was connected to the cell through a non-isothermal electrolyte bridge/Luggin capillary probe filled with saturated *KCl* solution and since it was placed outside the glass cell a thermal liquid junction potential (TLJP) exists, due to the fact that the tip of the Luggin probe in the cell and the reference electrode are at different temperatures (maximum difference of 60 ^oC). The development of the TLJP in *KCl* solutions (but not in saturated *KCl*) has been extensively studied [20] and, based upon the existing data, we conclude that the TLJP would be no more than a few millivolts at the highest cell temperature. Accordingly, the TLJP was ignored.

In order to suppress any contamination of the system by the reactions occurring on the counter electrode surface, the WE and CE compartments were separated from

the cell by means of a glass frit (Figure 1). The surface of the working electrode was abraded first with different grades of emery papers (800-1200 grit size) and was then polished with diamond suspension down to 0.25 μm, in order to obtain a mirror-like surface. After polishing, the electrode was cleaned ultrasonically for 5 minutes in ethanol and was then rinsed with acetone and distilled water. The electrolyte was 0.03 M H_3BO_3 and 0.15 M *NaOH* solution was added yield the desired pH. All solutions were prepared from de-ionized water (milli-Q system, 18.3 MΩ-cm). The prepared solution was saturated by ultra-high purity hydrogen gas. Saturation began at least 24 h before starting an experiment. Before initiating the electrochemical measurements, a constant cathodic voltage of -1.5 V *vs. Ag/AgCl*(4 M *KCl*) was applied for 30 min., in order to remove any oxide layer that may have formed during the polishing process and subsequent exposure to air, and to promote the acquisition of reproducible results.

Steady-state potentiostatic polarization measurements were performed using a Gamry Instruments (PC3/300 Potentiostat/Galvanostat/ZRA). All of the measurements were made after the current reached the steady-state plateau. The measurements were performed in the direction from negative to positive potential with an interval of 0.1 V between each step while applying, sequentially, four rotation speeds (100, 400, 900 and 1600 rpm) at each potential step.
The kinetic currents were calculated based on the Koutecky–Levich equation,

$$\frac{1}{i} = \frac{1}{i_k} + \frac{1}{i_D} = \frac{1}{i_k} + \frac{1}{BC_0\omega^{1/2}} \qquad (6)$$

where i is the measured current, i_k is the kinetic current, i_D is the diffusion limited current, ω is the rotation velocity (rad. s^{-1}), and BC_0 is a constant related to the number of electrons transferred in the reaction, the gas concentration, and diffusivity, as well as the electrolyte kinematic viscosity [21]. The steady-state cathodic polarization curves were plotted for three different pH values of 5.72, 8.00 and 9.20 at room temperature, four different hydrogen pressures of 1, 0.3, 0.5 and 0.1 (atm), and four different temperatures of 20, 40, 60 and 80 ^oC.

Electrochemical Impedance Spectroscopy (EIS) measurements were carried out by using a Gamry Instrument (PC3/300 Potentiostat/Galvanostat/ZRA). The amplitude of the perturbation voltage was 10 mV peak-to-peak over a 5 kHz to 0.01Hz frequency range using 10 measurement points per decade. The working electrode prior to the impedance measurements was potentiostatically polarized at each potential until it reached a steady-state as indicated by the constancy of the current. All of the collected impedance data were validated by Kramers-Kronig transformation [22].

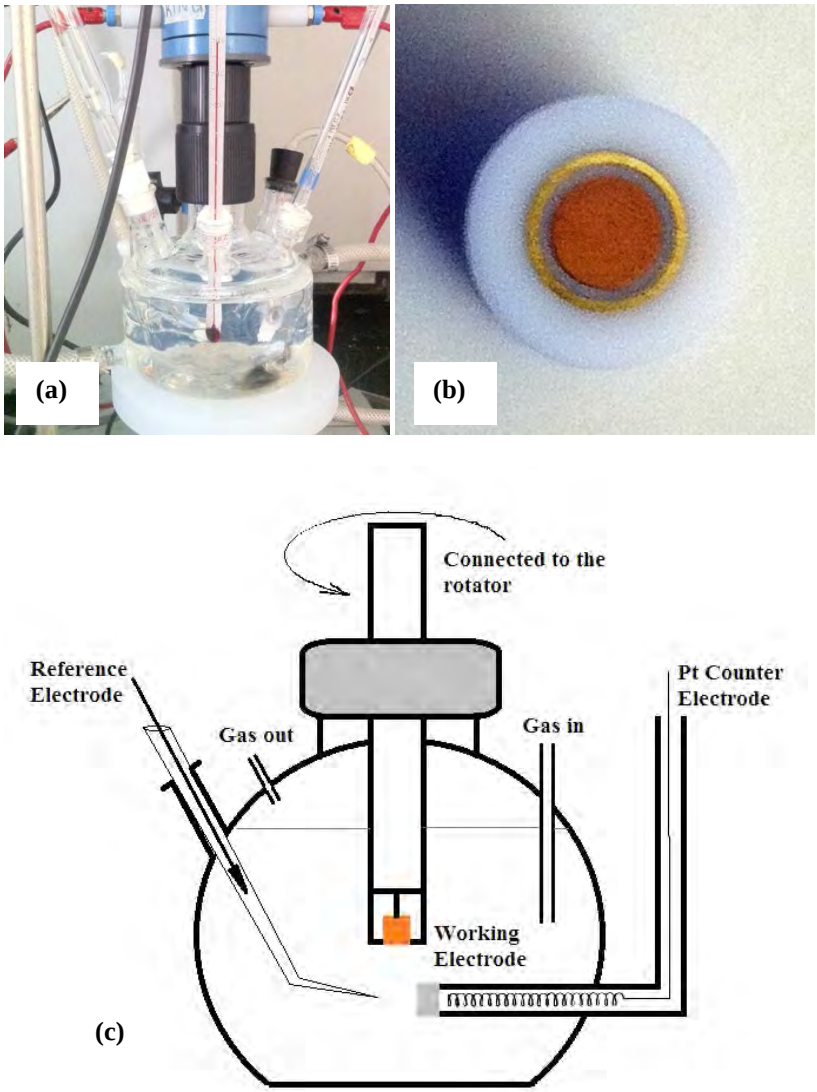

Figure 1.(a) A photograph of the cell filled with borate buffer solution, (b) working electrode (RDE) (c) schematic of the electrochemical cell.

3. Results and Discussion

3.1. Calculation of the electrochemical kinetic parameters

The correlation between the exchange current density ($i_0(H_2)$), dissolved hydrogen gas concentration ([H_2]), solution pH ([H^+]), and temperature (T) can be expressed as,

$$i_0(H_2,T) = i_0^0(H_2,T)[H_2]^{\beta}[H^+]^{\alpha} \quad (7)$$

in which the standard exchange current density, $i_0^0(H_2,T)$ (A cm^{-2}), is a function of the temperature through the activation energy,

$$i_0^0(H_2,T) = i_0^{0'}(H_2,298.15K)e^{\frac{-E_{ac}}{R}(\frac{1}{T}-\frac{1}{298.15})} \quad (8)$$

where $i_0^{0'}(H_2, 298.15)$ is the standard exchange current density at 298.15K (A cm^{-2}), E_{ac} is the activation energy of the hydrogen reduction reaction (kJ mol^{-1}), R is the gas constant (8.314 J K^{-1} mol^{-1}), and T is the Kelvin temperature (K). Generally, the current density of a charge transfer reaction is given by the generalized Butler-Volmer equation,

$$i = \frac{e^{\frac{\eta}{\beta a}} - e^{-\frac{\eta}{\beta c}}}{\frac{1}{i_0} + \frac{e^{\frac{\eta}{\beta a}}}{i_{l,a}} - \frac{e^{-\frac{\eta}{\beta c}}}{i_{l,c}}} \quad (9)$$

where i is the current density (A cm^{-2}), η is an overpotential expressed as the difference between the applied potential (E), and the equilibrium potential (E^{eq}), β_a and β_c are the anodic and cathodic Tafel constants, respectively, and $i_{l,a}$ and $i_{l,c}$ are the anodic and cathodic limiting current densities (A cm^{-2}). Since, in this study, we only consider the cathodic reaction, and because the limiting cathodic current density, corresponding to the reduction of water is very high, Eq. (9) will be simplified to the cathodic Tafel equation expressed as Eq. (10),

$$i = -i_0(e^{-\frac{\eta}{\beta c}}) \quad (10)$$

and this equation has been used in the first stage of optimization, in order to extract the exchange current density (i_0), and cathodic Tafel constant from the experimental results.

3.2. Effect of Temperature

Figure 2 shows the effect of temperature on the kinetics of the HER on copper at pH = 8.00 and P_{H2} = 1 atm. As can be seen, increasing the temperature results in increasing the current density for the same potential. Another effect of temperature is on the equilibrium potential. Increasing the temperature shifts the equilibrium potential to more negative values, which is in agreement with the Nernst equation and thermodynamics. Temperature also affects the overpotential of the reaction at a constant current density for kinetic reasons. As can be seen from Figure 2, increasing the temperature results in a decrease in the overpotential, resulting from an increase in the exchange current density. Similar behavior has been reported by other researchers for different materials [15,16].

3.3. Effect of Hydrogen Pressure

It is generally accepted that increasing the hydrogen pressure will shift the HER equilibrium potential in the negative direction, which is sometimes referred to as "activation", and increase the exchange current density [17]. The typical effect of hydrogen gas pressure on the kinetics of the hydrogen evolution reaction on copper at pH= 8.00 and T = 20 ^{o}C is shown in Figure 3.

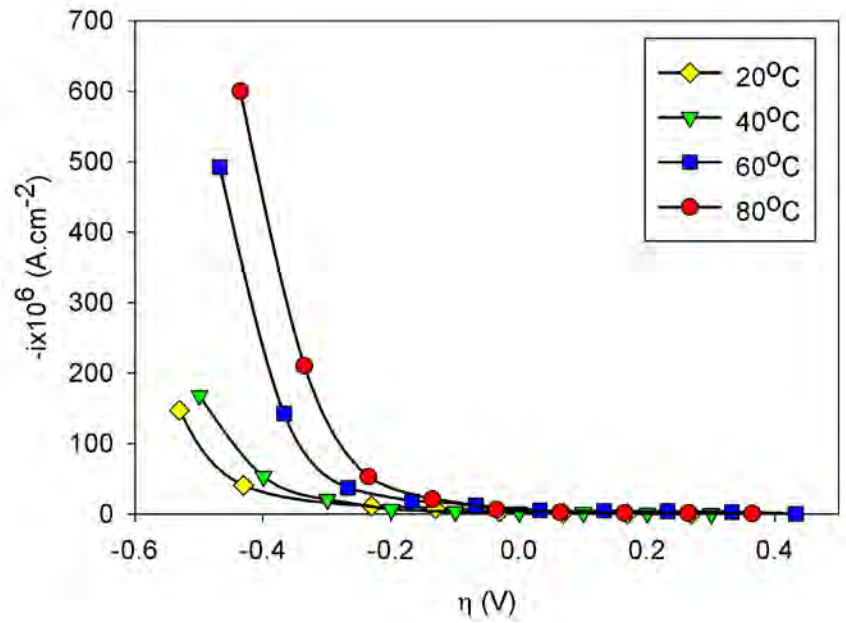

Figure 2. Steady-state polarization curves for the HER on copper as a function of temperature at p_{H2} =1atm, pH = 8.00.

As can be seen, the effect of hydrogen gas pressure on the current density is most pronounced at high overpotentials. A Similar trend has been reported for nickel-based super alloys (Alloys 600 and 690) in high temperature aqueous solutions [17]. It should be noted that, in the optimization, only the data from the high (negative) overpotential region down to the equilibrium potential have been considered; no data for the oxidation of hydrogen was included.

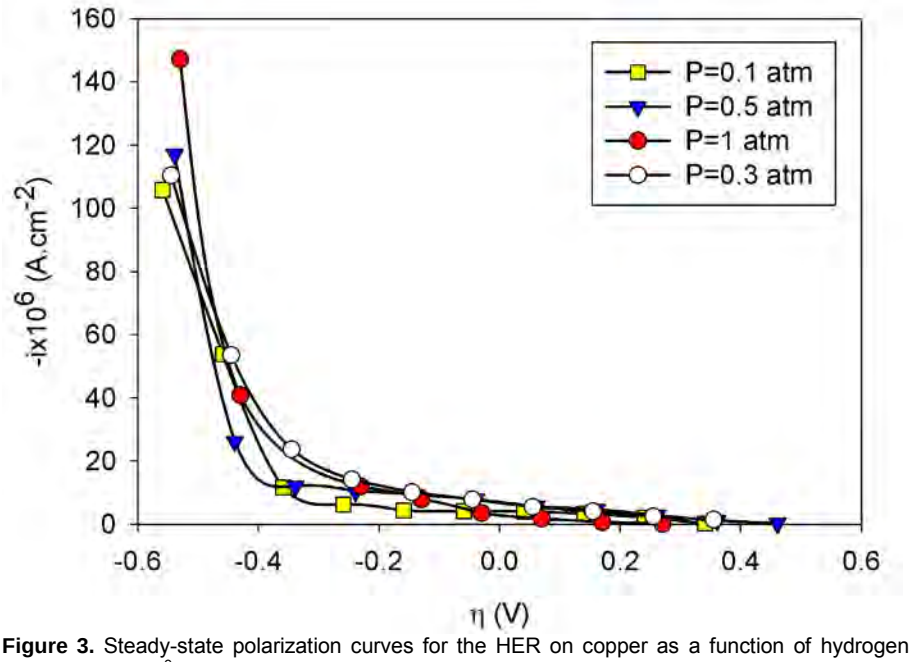

Figure 3. Steady-state polarization curves for the HER on copper as a function of hydrogen pressure at T=20°C, pH = 8.00.

3.4. Effect of pH

Figure 4 displays the impact of pH on the kinetics of the HER on copper at T = 20°C and P_{H2} = 1 (atm). As we show later, the kinetic data for this pH range are consistent with the reaction proceeding via the reduction of water instead of protons. Therefore, the change of pH has only a small effect on the kinetics of the reaction. On the other hand, the pH has a prominent effect on the equilibrium potential, because of the linear proportionality of the equilibrium potential with pH in the Nernst equation.

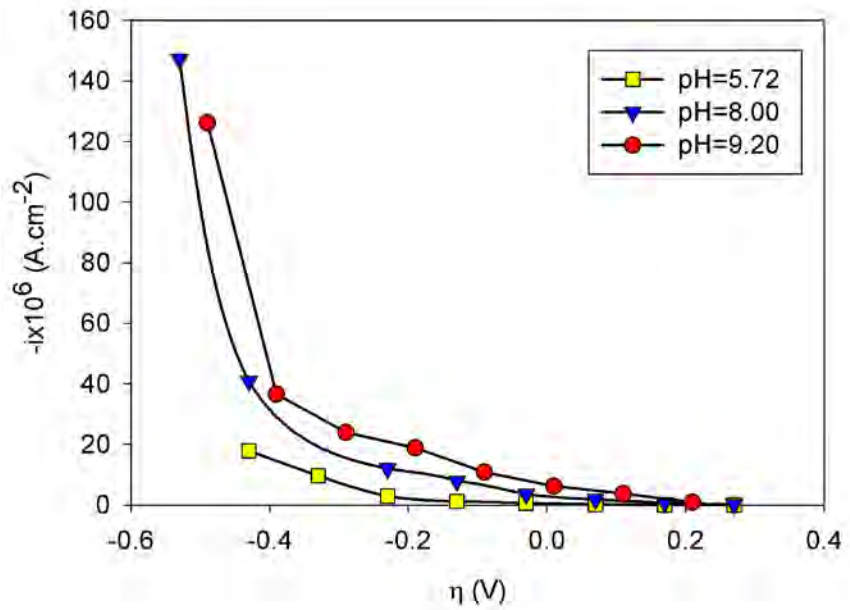

Figure 4. Steady-state polarization curves for the HER on copper as a function of solution pH at p_{H2} = 1atm, T = 20°C.

3.5. Optimization

Optimization was carried out in two stages. In the first stage, the exchange current density, $i_0(H_2)$, and the cathodic Tafel constant, β_c, were extracted from fitting the cathodic Tafel equation [Eq. (10)] to the experimental data. Table 1 lists the values obtained for these parameters for wide ranges of temperatures, solution pH, and hydrogen gas pressures. The cathodic transfer coefficient (α_c) can be calculated from Eq. (11) using the obtained cathodic Tafel constant,

$$\beta_c = \frac{RT}{\alpha_c nF} \qquad (11)$$

In the second stage of the optimization, the obtained electrokinetic parameters were used again in order to obtain the kinetic orders of the HER with regard to the hydrogen gas concentration and solution pH ($[H^+]$). Also, from the dependence of the exchange current density on temperature, the activation energy of the HER on copper and the standard exchange current density at 298.15 K were obtained. Figures 5(a) to (d) show the results of the second stage of the optimization process.

Table 1. Kinetic parameters for the HER on Cu obtained from optimization at different T, pH and Hydrogen partial pressure.

Temperature(°C)	*pH*	$P(H_2)$(atm)	$E^{eq}(V_{SHE})$	i_0(A.cm^{-2})	βc(mV/dec)
20	5.72	1	-0.331	3.46×10^{-7}	120
20	8.00	1	-0.465	6.76×10^{-7}	98
20	9.20	1	-0.535	1.01×10^{-6}	100
20	8.00	0.5	-0.456	5.34×10^{-7}	100
20	8.00	0.3	-0.450	4.73×10^{-7}	100
20	8.00	0.1	-0.436	3.28×10^{-7}	95
40	8.00	1	-0.497	7.76×10^{-7}	90
60	8.00	1	-0.529	3.84×10^{-6}	96
80	8.00	1	-0.560	4.52×10^{-6}	87

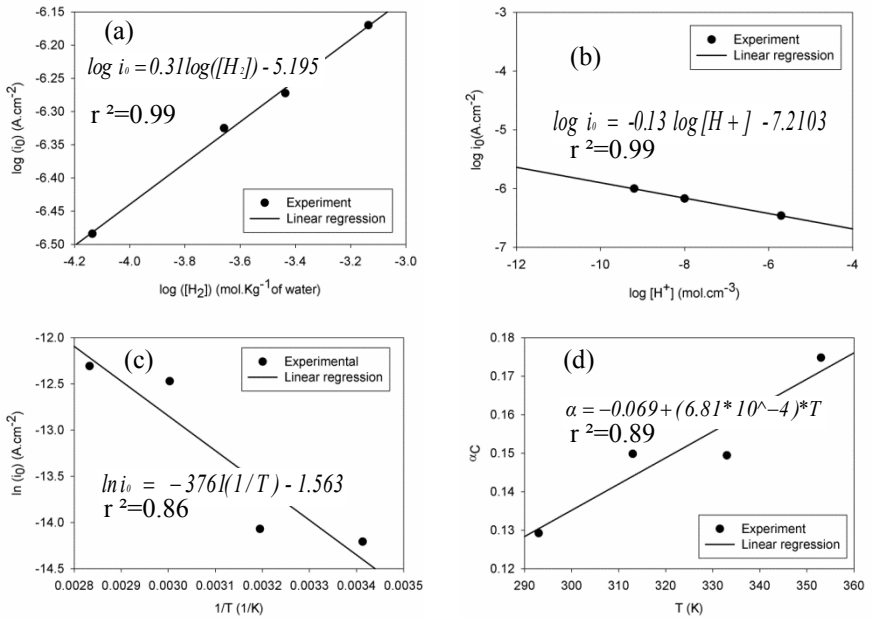

Figure 5. Plots of logarithm of the exchange current density for the HER on copper as a function of (a) hydrogen gas concentration in solution, (b) H^+ ions concentration in solution (c) reciprocal of Kelvin temperature and (d) the cathodic transfer coefficient for the HER on copper as a function of Kelvin temperature.

From the plot of *ln* i_0 versus *1/T* [Figure 5(c)], the activation energy of the HER on copper was calculated to be ≈ 32 kJ mol^{-1}. Collecting all of the electrokinetic parameters from the second stage of the optimization enabled us to develop an analytical equation for the kinetics of the HER on copper as a function of hydrogen gas concentration, solution pH, and temperature,

$$i_0(H_2) = 0.2\exp(-\frac{31268.9}{RT})[H_2]^{0.31}[H^+]^{-0.13} \qquad (12)$$

where $i_0(H_2)$ is the exchange current density (A cm^{-2}), $[H_2]$ is hydrogen gas concentration in solution (mol Kg^{-1} of water), $[H^+]$ is the concentration of hydronium ions in solution (mol cm^{-3}), R is the gas constant (8.314 J K^{-1} mol^{-1}), and T is the Kelvin temperature (K). The derived analytical expression has then been used to calculate

the exchange current density as a function of temperature and to compare the results with the original experimental data. As can be seen from Figure 6, reasonable agreement exists between the calculated results and those obtained from the experiments, thereby illustrating the viability of the derived expression.

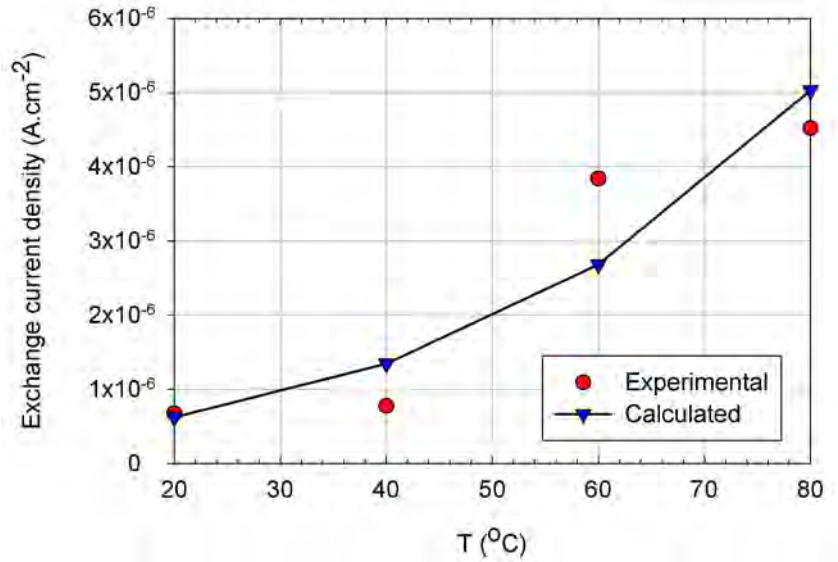

Figure 6. Comparison of the exchange current density of experimental data and calculated data using derived correlation of copper (p_{H2}=1atm, pH=8.00)

Finally, we introduce a cathodic Tafel equation based upon the parameters obtained from the optimization part (Eq. 13), which enables us to compare the cathodic polarization curves derived from this equation with those obtained experimentally.

$$i(H_2) = 0.2\exp(-\frac{31268.9}{RT})[H_2]^{0.31}[H^+]^{-0.13}\exp((-(-0.069 + 6.81 \times 10^{-4}T)nF\eta/RT)) \quad (13)$$

Figure 7 shows the results obtained from this analysis for a range of temperature between 20-80 °C, pH = 8.00, and the hydrogen gas pressure equal to 1 (atm). It is seen that Eq. (13) can reproduce the experimental results very well.

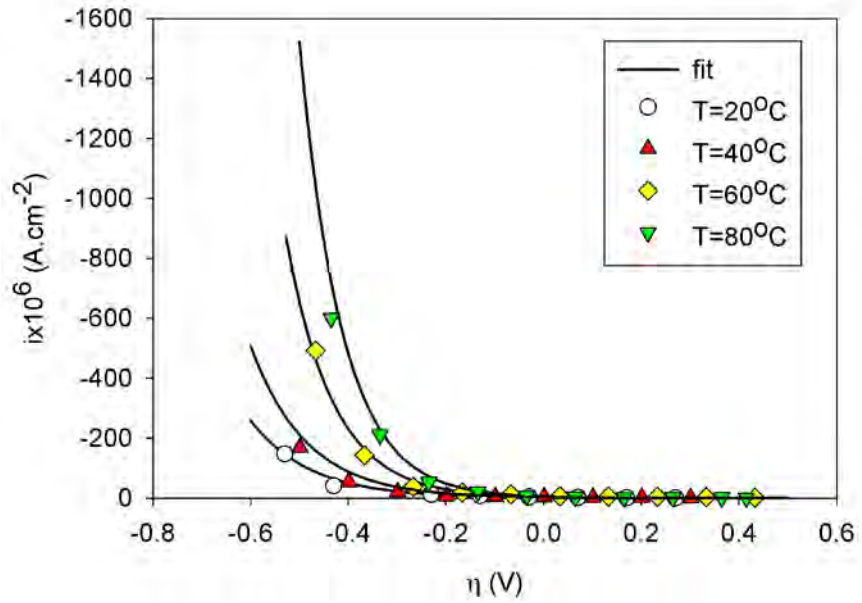

Figure 7. Steady-state polarization diagram for copper as a function of temperature, pH=8.00, p_{H2}=1atm. The experimental results (symbols) are compared with data calculated from Eq. (13) (lines)

3.6. Effect of *HS*$^-$

Figure 8 displays the effect of sulphide on the kinetics of HER on copper at T = 20 ^oC and p_{H2} = 1 (atm). Sulphide concentrations in electrolyte were varied by addition of different amount of $Na_2S.9H_2O$, relevant to the condition in the repository. It is known that, presence of sulphide ions in aqueous solution can accelerate localized corrosion of metal through the chemisorptions to the metal surfaces and hindering of passivation [24]. This adsorbed layer could block the metal surface and affect the rate of hydrogen evolution too [24]. However, as can be seen from Figure 8, addition of sulphide up to 2×10^{-5}M (the relevant concentration in the repository) seems not to have any effect on the kinetics of HER on copper. Obtained kinetics parameters from optimization of cathodic Tafel equation listed in Table 2 confirm this hypothesis. On the other hand, upon increasing the concentration of sulphide ions in solution (up to 2×10^{-3}M) an increase in the kinetics of HER can readily be detected. However, reader should be noted that once we increased the concentration of sulphide in solution, a black film immediately formed on the surface of copper electrode so the observed current not necessarily could be attributed to the HER only but to a system under the mixed control.

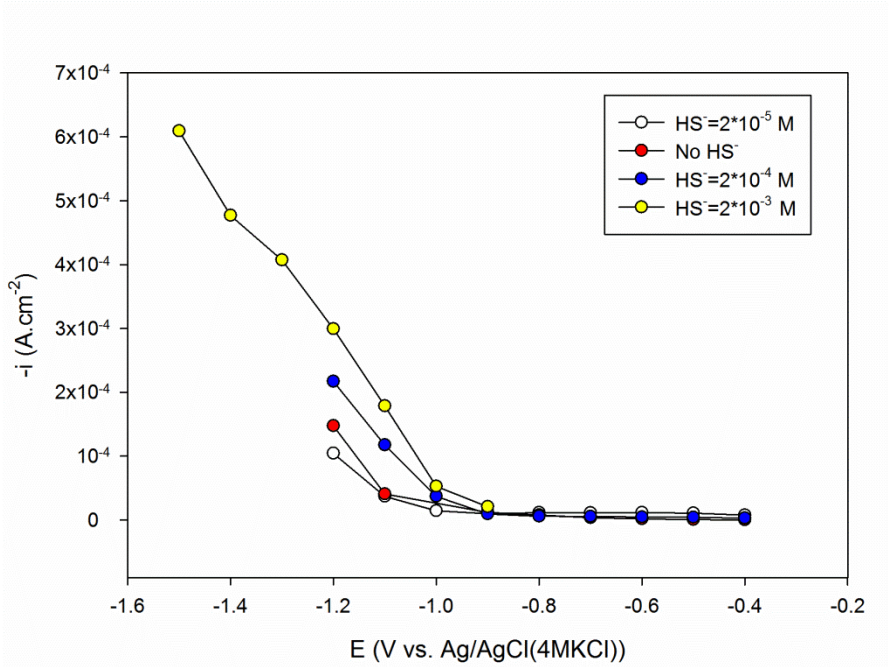

Figure 8. Steady-state polarization curves for HER on copper as a function of sulphide concentration at p_{H2} = 1atm, T = 20°C.

Table 2. Kinetic parameters for HER on *Cu* obtained from optimization at different [*HS*-].

Temperature(°C)	*[HS⁻], M*	i_0(A.cm^{-2})	βc(mV/decade)
20	-	6.76×10^{-7}	98
20	2×10^{-5}	5.87×10^{-7}	102
20	2×10^{-4}	2.74×10^{-6}	121
20	2×10^{-3}	4.35×10^{-5}	305

3.7. Impedance Model

It is well-understood that the HER proceeds through three elementary steps: the Volmer, Heyrovsky, and Tafel reactions [23]. It is also known that adsorption of hydrogen and oxygen species (oxygen atoms or hydroxyl groups) on the metal surface play an important role on the corrosion of metals under both oxic and anoxic conditions [17]. Copper is the least noble metal of the Group 11 elements of the periodic table and is the most hydro- and oxo-phillic metal of that group [24]. Hydrogen can be adsorbed onto the surface of copper from gaseous hydrogen and calculations have divulged that the hydroxyl group can be adsorbed onto the surface of copper more strongly than for any other transition metals [24]. The work of Protopopoff and Marcus [24] on developing potential-pH diagrams incorporating adsorbed *H* and *OH* species on copper surface has shown that for a given pH, there should be a layer of adsorbed hydrogen at a potential slightly above the H^+/H_2 equilibrium potential at 1 atm and that this layer will be replaced with adsorbed water molecules and hydroxyl groups when going to more positive potentials. In addition, in situ STM (Scanning Tunneling Microscopy), SERS (Surface-Enhanced Raman Spectroscopy) and EQCM (Electrochemical Quartz Crystal Microbalance) results reported by several researchers have revealed the adsorption of hydroxyl group upon

the cathodic polarization of copper in alkaline media [25-30]. As a result, we propose the following mechanism, in order to explain the kinetic behavior of the HER on copper:

$$Cu(SS) + OH^- \underset{k_{-1}}{\overset{k_1}{\rightleftharpoons}} CuOH_{ads} + e^- \tag{14}$$

$$CuOH_{ads} + OH^- \underset{k_{-2}}{\overset{k_2}{\rightleftharpoons}} Cu(OH)_2^- + SS \tag{15}$$

$$Cu(SS) + H_2O + e^- \underset{k_{-3}}{\overset{k_3}{\rightleftharpoons}} CuH_{ads} + OH^- \tag{16}$$

$$CuH_{ads} + H_2O + e^- \underset{k_{-4}}{\overset{k_4}{\rightleftharpoons}} Cu(SS) + H_2 + OH^- \tag{17}$$

$$2CuH_{ads} \underset{k_{-5}}{\overset{k_5}{\rightleftharpoons}} 2Cu(SS) + H_2 \tag{18}$$

where the indexes "*ads*" and "*SS*" denote adsorbed species and unoccupied surface sites respectively, and the k_i*'s* are the rate constants of the *i*'th forward or backward reaction. In this study, we assumed that: (i) Charge transfer reactions obey the Tafel equation; (ii) Mass transfer effects are negligible (by applying high rotation speed, e.g. 2000 rpm); and (iii) Surface adsorption obeys the Langmuir adsorption isotherm. From mass balance, we have:

$$\beta \frac{d\theta_1}{dt} = \{k_1[OH^-][Cu(SS)] + k_{-2}[OH^-][Cu(OH)_2^-]\}(1-\theta_1-\theta_2) - \{k_{-1} + k_2[OH^-]\}\theta_1 \tag{19}$$

$$\beta \frac{d\theta_2}{dt} = \{k_3[H_2O] + k_{-4}[OH^-][H_2] + 2k_{-5}[H_2](1-\theta_1-\theta_2)\}(1-\theta_1-\theta_2) - \{k_{-3}[OH^-] - k_4[H_2O] - 2k_5\theta_2\}\theta_2 \tag{20}$$

where β is the total number of sites calculated from the surface atomic density (=2×10^{-9} mol cm^{-2}), $k_i = k_i^0 \exp(-b_i f\eta)$, $k_{-i} = k_{-i}^0 \exp((1-b_i)f\eta)$, θ_1 and θ_2 are surface coverage of adsorbed *OH* and *H* species, respectively. In order to simplify the mathematics, the concentration terms were included into the definitions of the rate constants, where appropriate:

$$\vartheta_1 = \bar{k}_1(1-\theta_1-\theta_2)e^{-b1f\eta} - \bar{k}_{-1}\theta_1 e^{(1-b1)f\eta} \tag{21}$$

$$\vartheta_2 = \bar{k}_2\theta_1 - \bar{k}_{-2}(1-\theta_1-\theta_2) \tag{22}$$

$$\vartheta_3 = \bar{k}_3(1-\theta_1-\theta_2)e^{-b2f\eta} - \bar{k}_{-3}\theta_2 e^{(1-b2)f\eta} \tag{23}$$

$$\vartheta_4 = \bar{k}_4\theta_2 e^{-b3f\eta} - \bar{k}_{-4}(1-\theta_1-\theta_2)e^{(1-b3)f\eta} \tag{24}$$

$$\vartheta_5 = 2\bar{k}_5\theta_2^2 - 2\bar{k}_{-5}(1-\theta_1-\theta_2)^2 \tag{25}$$

Therefore, we can re-write Eqs. (19) and (20) using the new definitions as:

$$\beta \frac{d\theta_1}{dt} = \vartheta_1 - \vartheta_2 = r_1 \tag{26}$$

$$\beta \frac{d\theta_2}{dt} = \vartheta_3 - \vartheta_4 - 2\vartheta_5 = r_2 \quad (27)$$

All the reactions involved in transferring electrons contribute to the observed steady-state current (e.g. Reactions 14, 16 and 17):

$$i = i_1 - i_3 - i_4 \quad (28)$$

where,

$$i_1 = F\{\bar{k}_1(1-\theta_1-\theta_2)e^{-b1f\eta} - \bar{k}_{-1}\theta_1 e^{(1-b1)f\eta}\} \quad (29)$$

$$i_3 = F\{\bar{k}_3(1-\theta_1-\theta_2)e^{-b2f\eta} - \bar{k}_{-3}\theta_2 e^{(1-b2)f\eta}\} \quad (30)$$

$$i_4 = F\{\bar{k}_4\theta_2 e^{-b3f\eta} - \bar{k}_{-4}(1-\theta_1-\theta_2)e^{(1-b3)f\eta}\} \quad (31)$$

Upon rearranging, we have:

$$i = F(\vartheta_1 - \vartheta_3 - \vartheta_4) = F(r_0) \quad (32)$$

Knowing that, under steady-state conditions, $\frac{d\theta_1}{dt} = \frac{d\theta_2}{dt} = 0$, we can calculate the values of θ_1 and θ_2, and then of i, in Eqs. (26), (27) and (32). Taking into account that r_0, r_1, and r_2 are functions of η, θ_1 , and θ_2 , the linearization of Eqs. (26), (27), and (32) and introducing them in phasor representation, gives,

$$\tilde{\imath} = F\left\{\left(\frac{\partial r_0}{\partial \eta}\right)_{\theta_1,\theta_2}\tilde{\eta} + \left(\frac{\partial r_0}{\partial \theta_1}\right)_{\theta_2,\eta}\tilde{\theta}_1 + \left(\frac{\partial r_0}{\partial \theta_2}\right)_{\theta_1,\eta}\tilde{\theta}_2\right\} \quad (33)$$

$$j\omega\beta\tilde{\theta}_1 = \left\{\left(\frac{\partial r_1}{\partial \eta}\right)_{\theta_1,\theta_2}\tilde{\eta} + \left(\frac{\partial r_1}{\partial \theta_1}\right)_{\theta_2,\eta}\tilde{\theta}_1 + \left(\frac{\partial r_1}{\partial \theta_2}\right)_{\theta_1,\eta}\tilde{\theta}_2\right\} \quad (34)$$

$$j\omega\beta\tilde{\theta}_2 = \left\{\left(\frac{\partial r_2}{\partial \eta}\right)_{\theta_1,\theta_2}\tilde{\eta} + \left(\frac{\partial r_2}{\partial \theta_1}\right)_{\theta_2,\eta}\tilde{\theta}_1 + \left(\frac{\partial r_2}{\partial \theta_2}\right)_{\theta_1,\eta}\tilde{\theta}_2\right\} \quad (35)$$

As a result, we have three equations in three unknowns, which upon solution will give us the value of $\frac{\tilde{\theta}_1}{\tilde{\eta}}$, $\frac{\tilde{\theta}_2}{\tilde{\eta}}$ and then $\frac{\tilde{\imath}}{\tilde{\eta}}$

$$\frac{\tilde{\theta}_1}{\tilde{\eta}} = -\frac{\left(\frac{\partial r_1}{\partial \theta_2}\right)_{\theta_1,\eta}\left(\frac{\partial r_2}{\partial \eta}\right)_{\theta_1,\theta_2} - \left(\frac{\partial r_1}{\partial \eta}\right)_{\theta_1,\theta_2}\left(\frac{\partial r_2}{\partial \theta_2}\right)_{\theta_1,\eta} + \left(\frac{\partial r_1}{\partial \eta}\right)_{\theta_1,\theta_2} j\omega\beta}{\left(\frac{\partial r_1}{\partial \theta_2}\right)_{\theta_1,\eta}\left(\frac{\partial r_2}{\partial \theta_1}\right)_{\theta_2,\eta} - \left(\frac{\partial r_1}{\partial \theta_1}\right)_{\theta_2,\eta}\left(\frac{\partial r_2}{\partial \theta_2}\right)_{\theta_1,\eta} + j\omega\beta\left[\left(\frac{\partial r_1}{\partial \theta_1}\right)_{\theta_2,\eta} + \left(\frac{\partial r_2}{\partial \theta_2}\right)_{\theta_1,\eta}\right] + \beta^2\omega^2} \quad (36)$$

and

$$\frac{\tilde{\theta}_2}{\tilde{\eta}} = -\frac{-\left(\frac{\partial r_1}{\partial \theta_1}\right)_{\theta_2,\eta}\left(\frac{\partial r_2}{\partial \eta}\right)_{\theta_1,\theta_2} + \left(\frac{\partial r_1}{\partial \eta}\right)_{\theta_1,\theta_2}\left(\frac{\partial r_2}{\partial \theta_1}\right)_{\theta_2,\eta} + \left(\frac{\partial r_2}{\partial \eta}\right)_{\theta_1,\theta_2} j\omega\beta}{\left(\frac{\partial r_1}{\partial \theta_2}\right)_{\theta_1,\eta}\left(\frac{\partial r_2}{\partial \theta_1}\right)_{\theta_2,\eta} - \left(\frac{\partial r_1}{\partial \theta_1}\right)_{\theta_2,\eta}\left(\frac{\partial r_2}{\partial \theta_2}\right)_{\theta_1,\eta} + j\omega\beta\left[\left(\frac{\partial r_1}{\partial \theta_1}\right)_{\theta_2,\eta} + \left(\frac{\partial r_2}{\partial \theta_2}\right)_{\theta_1,\eta}\right] + \beta^2\omega^2} \quad (37)$$

and by substitution of these values into the Eq. (33) we obtain the faradaic admittance of the system as follow

$$Y_f = \frac{\tilde{\imath}}{\tilde{\eta}} = F\left\{\left(\frac{\partial r_0}{\partial \eta}\right)_{\theta_1,\theta_2} + \left(\frac{\partial r_0}{\partial \theta_1}\right)_{\theta_2,\eta}\frac{\tilde{\theta}_1}{\eta} + \left(\frac{\partial r_0}{\partial \theta_2}\right)_{\theta_1,\eta}\frac{\tilde{\theta}_2}{\eta}\right\} \quad (38)$$

which can be re-written in a more convenient format as follow:

$$Y_f = A + \frac{B + j\omega C}{D + j\omega E + \beta^2\omega^2} \quad (39)$$

where,

$$A = F\left(\frac{\partial r_0}{\partial \eta}\right)_{\theta_1,\theta_2} \quad (40)$$

$$B = \left\{-\left(\frac{\partial r_0}{\partial \theta_1}\right)_{\theta_2,\eta}\left(\frac{\partial r_1}{\partial \theta_2}\right)_{\theta_1,\eta}\left(\frac{\partial r_2}{\partial \eta}\right)_{\theta_1,\theta_2} + \left(\frac{\partial r_0}{\partial \theta_1}\right)_{\theta_2,\eta}\left(\frac{\partial r_1}{\partial \eta}\right)_{\theta_1,\theta_2}\left(\frac{\partial r_2}{\partial \theta_2}\right)_{\theta_1,\eta} + \left(\frac{\partial r_0}{\partial \theta_2}\right)_{\theta_1,\eta}\left(\frac{\partial r_1}{\partial \theta_1}\right)_{\theta_2,\eta}\left(\frac{\partial r_2}{\partial \eta}\right)_{\theta_1,\theta_2} - \left(\frac{\partial r_0}{\partial \theta_2}\right)_{\theta_1,\eta}\left(\frac{\partial r_1}{\partial \eta}\right)_{\theta_1,\theta_2}\left(\frac{\partial r_2}{\partial \theta_1}\right)_{\theta_2,\eta}\right\} \quad (41)$$

$$C = -\beta\left\{\left(\frac{\partial r_0}{\partial \theta_1}\right)_{\theta_2,\eta}\left(\frac{\partial r_1}{\partial \eta}\right)_{\theta_1,\theta_2} + \left(\frac{\partial r_0}{\partial \theta_2}\right)_{\theta_1,\eta}\left(\frac{\partial r_2}{\partial \eta}\right)_{\theta_1,\theta_2}\right\} \quad (42)$$

$$D = \left\{\left(\frac{\partial r_1}{\partial \theta_2}\right)_{\theta_1,\eta}\left(\frac{\partial r_2}{\partial \theta_1}\right)_{\theta_2,\eta} - \left(\frac{\partial r_1}{\partial \theta_1}\right)_{\theta_2,\eta}\left(\frac{\partial r_2}{\partial \theta_2}\right)_{\theta_1,\eta}\right\} \quad (43)$$

$$E = \beta\left\{\left(\frac{\partial r_1}{\partial \theta_1}\right)_{\theta_2,\eta} + \left(\frac{\partial r_2}{\partial \theta_2}\right)_{\theta_1,\eta}\right\} \quad (44)$$

Accordingly, the total impedance of the system, which comprises all of the contributory interfacial phenomena, including the double layer capacitance and the resistance of the solution, can be represented by an electrical equivalent circuit. Figure 9 shows the equivalent circuit for the system that we used for analyzing the impedance of the HER on copper.

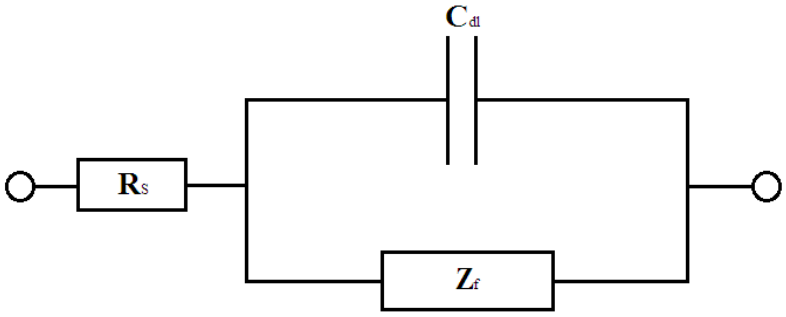

Figure 9. Equivalent electrical circuit describing the total impedance of the system under the study, C_{dl} represents the double layer capacitance, Z_f represents the faradaic impedance and R_s represents the solution resistance.

The total impedance of the system can then be expressed by Eq. (45):

$$Z_T = R_S + \left[\frac{1}{Z_f} + \frac{1}{Z_{C_{dl}}}\right]^{-1} \quad (45)$$

where Z_f is faradaic impedance associated with the HER, as given by the inverse of the interfacial admittance, Eq. (39), Z_{Cdl} is the impedance of the double layer capacitance and R_s is the uncompensated solution resistance. Since, on solid electrodes, most frequently, depressed semicircles are observed in the Nyquist plane, as we have found in this study, the double layer capacitance in the circuit was replaced by a constant phase element. The rationale for doing this is that the inhomogeneity of the polycrystalline electrode surface results in a distribution of capacitive states and hence in a distribution in relaxation time. The impedance of the CPE is defined as:

$$Z_{CPE} = \frac{1}{(j\omega)^{\varphi} Y_0} \tag{46}$$

where φ corresponds to a depression angle and Y_0 is a constant related to the electrode capacitance.

3.8. Extraction of Model Parameters Values from EIS data

The Genetic curve fitting approach was selected for optimizing the proposed model onto the experimental EIS data, in order to extract values for the model parameters. Briefly, curve fitting ("optimization") is the process for obtaining a representation of a multi-variate data set by an "objective function" that describes a physico-electrochemical system, at least as employed here. The main objective of optimization is to find the set of parameter values that minimize the total error determined from the difference between the observed dependent variable values, $Z(\omega)$, and those calculated from the derived parameter values over the considered data set. After selecting a functional form and setting up the error metrics, curve fitting becomes an optimization problem. It is a common method used to reconcile models to observations and for developing optimal solutions to different kinds of problems, such as simulation and statistical inference [31,32]. Even though there have been many ways proposed to approach curve fitting ("optimization") problems, there are few general techniques for complex functions with no derivative information and/or that are non-linear in form. Differential Evolution (DE) is a popular technique in evolutionary computation research. It is capable of handling a large number of parameters and a rotated, multi-modal solution space. Evolutionary computation (EC) techniques seek to emulate the evolution of natural biological systems in order to find an optimal solution for a given problem. Genetic Algorithms (GA) are used for the optimization of complicated problems in a wide range of applications, such as in engineering design, economic decisions, etc. Holland was the first to employ genetic algorithms, as described in the ground-breaking book on genetic algorithms, "Adaptation in Natural and Artificial Systems" [30]. A GA has been used in very few prior cases to optimize impedance data, most notably by VanderNoot and Abrahams [33] and Kanoun et al. [34]. GA is not commonly used to optimize impedance models, because they are computationally taxing and the functions are generally simple, making a gradient method more convenient. This is not the case with the complex models, however.

The optimization procedure ends if the result satisfies the selected convergence criteria and the following requirements: (1) All the parameter values are physically reasonable and exist within known bounds; (2) The calculated $Z'(\omega)$ and $Z''(\omega)$ agree with their respective experimental results in both the Nyquist and Bode planes; and (3) The calculated steady-state current density, as estimated from the parameter values obtained from the optimization, is in reasonable agreement with the experimental values; note that no "steady-state ($f = 0$) data are involved in the optimiza-

tion, and hence this represents a powerful, independent test of the optimization technique. The *Igor Pro* (*Version 6.2.1.0, ©1988-2010 WaveMetrics, Inc*.) software with a custom software interface powered by Andrew Nelson's "gencurvefit" [35] package was used in this work for optimization, so as to obtain values for the standard rate constants (k_i), transfer coefficients (α_i) (for the *i* elementary interfacial reactions), and double layer capacitance (C_{dl}). A freely distributed interface is now available to effectively leverage gencurvefit for the optimization of complex impedance functions [36].

Figures 10 to 12 show typical experimental electrochemical impedance spectra for the HER on copper in borate buffer solution [0.03M H_3BO_3 + 0.15M *NaOH*, as appropriate] (pH = 5.74, 8.00 and 10.00 at room temperature) in the form of Nyquist and bode plots as a function of potential. The Nyquist plots show one well-formed semi-circle at all applied potentials except for the case of E = -0.9 V *vs. Ag/AgCl*(4M *KCl*) at pH = 5.74, where another semi-circle at low frequencies was observed. As can be seen, increasing the pH (= 10.00) causes the magnitude of the impedance to become lower, meaning that a smaller energy barrier exists against the charge transfer reaction, which is in agreement with higher exchange current density measured at higher pH, as shown earlier in the potentiostatic polarization results.

The lower impedance at higher pH could also be attributed to the higher electrical conductivity of the solution and, in fact the solution resistance obtained from the modeling confirmed this postulate. The best-fit results, as calculated from the proposed mechanism, are also included in these figures as solid lines. It can be seen that the agreement between the experimental results and those calculated from the model is very good, indicating that the proposed mechanism and associated parameter values provide a reasonable account of the experimental data. The averages of the extracted kinetic parameters for all applied potentials at different pH are listed in Table 3. It should be noted that the proposed mechanism and obtained parameters are not necessarily unique and other mechanisms might provide equally good simulations of the experimental data.

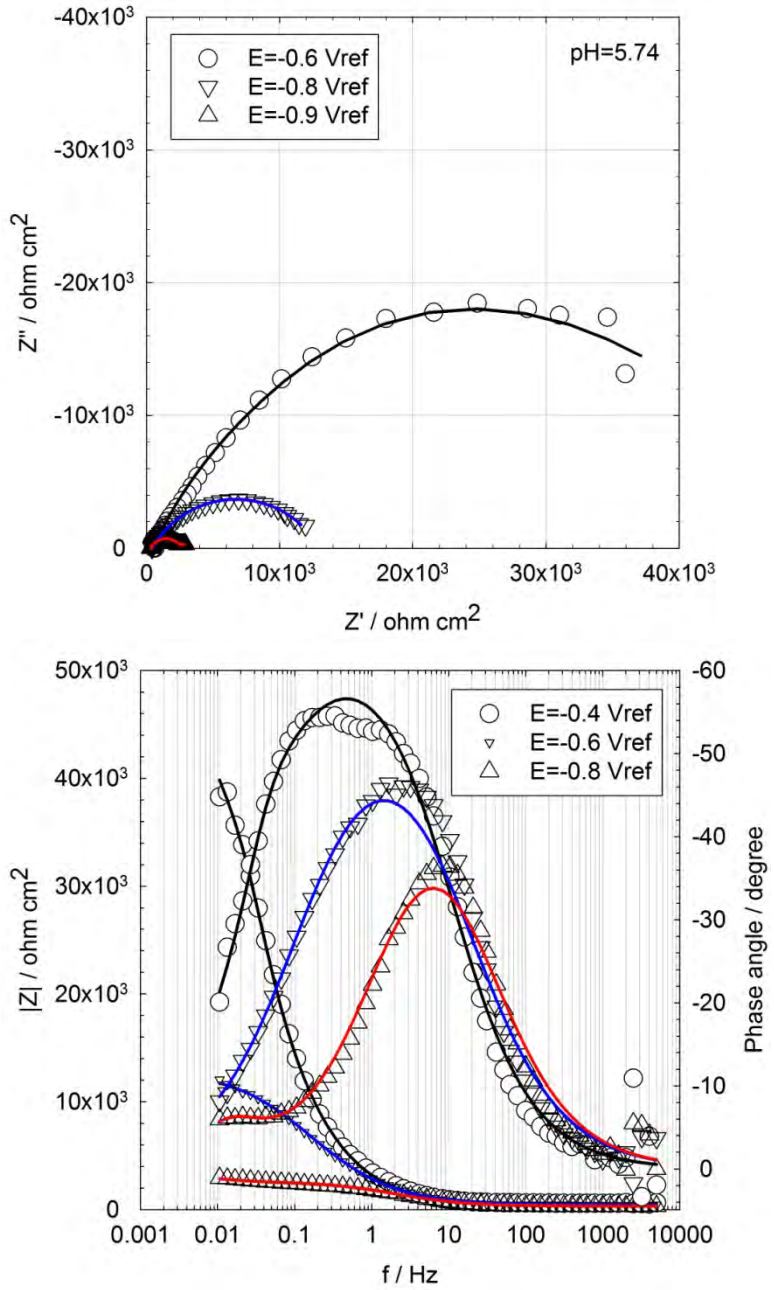

Figure 10. Experimental and simulated impedance spectra for the HER on copper in 0.03M H_3BO_3/0.15M *NaOH*, as appropriate, pH=5.74 at room temperature as a function of applied potential.(rpm=2000)

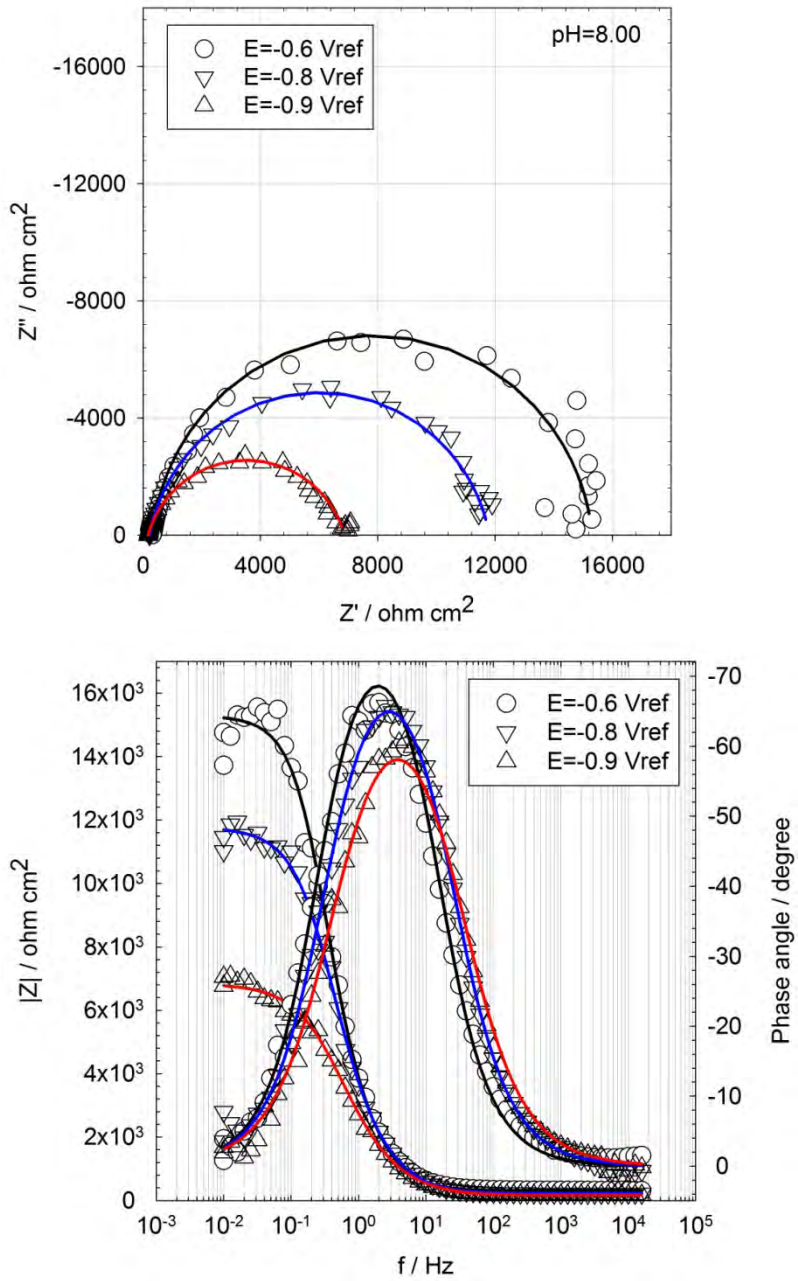

Figure 11. Experimental and simulated impedance spectra for the HER on copper in 0.03M H_3BO_3 / 0.15M *NaOH*, as appropriate, pH=8.00 at room temperature as a function of applied potential.(rpm=2000)

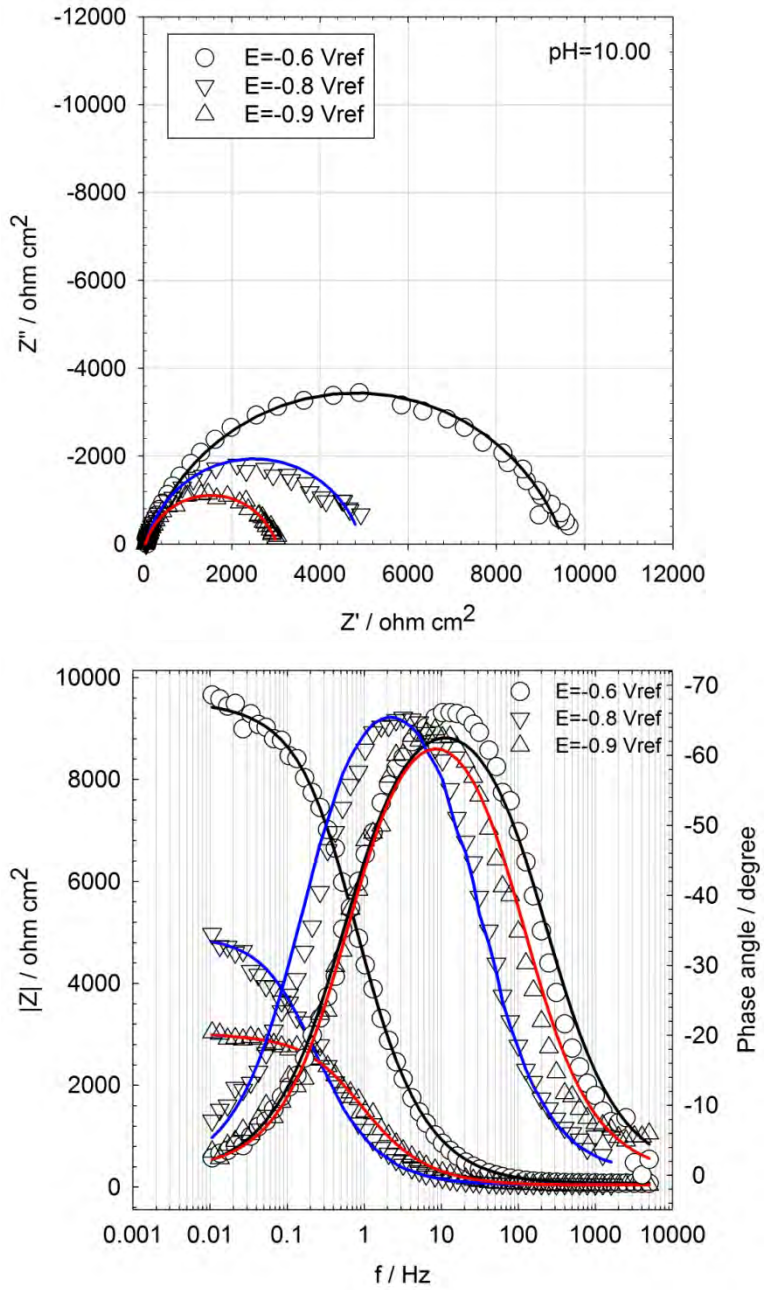

Figure 12. Experimental and simulated impedance spectra for the HER on copper in 0.03M H_3BO_3 / 0.15M *NaOH*, as appropriate, pH=10.00 at room temperature as a function of applied potential. (rpm=2000)

A successful model must reproduce not only the general features of observed impedance plots, but also the features of the steady-state current/potential curves. Figure 13 (a-c) shows a comparison between the experimentally-measured steady-state current density and that calculated from the kinetic parameters obtained by optimization. As can be seen, there is a good agreement between the experimental and calculated data with a major discrepancy at E = -0.9 V *vs. Ag/AgCl*(4M *KCl*) at pH = 5.74, which may be a result of the assumptions behind the proposed mechanism, such as the use of the Langmuir adsorption isotherm.

Table 3. Averaged kinetic parameters obtained from optimization of proposed model for the HER on copper.

	pH=5.74	pH=8.00	pH=10.00
$\bar{k}_1$ (mol cm^{-2} s^{-1})	6.07×10^{-12}	1.91×10^{-11}	1.01×10^{-11}
$\bar{k}_{-1}$ (mol cm^{-2} s^{-1})	2.74×10^{-9}	3.97×10^{-9}	9.28×10^{-10}
$\bar{k}_2$ (mol cm^{-2} s^{-1})	2.45×10^{-12}	3.73×10^{-13}	2.09×10^{-11}
$\bar{k}_{-2}$ (mol cm^{-2} s^{-1})	2.75×10^{-12}	5.00×10^{-12}	2.60×10^{-12}
$\bar{k}_3$ (mol cm^{-2} s^{-1})	1.68×10^{-16}	6.61×10^{-15}	7.71×10^{-15}
$\bar{k}_{-3}$ (mol cm^{-2} s^{-1})	7.22×10^{-12}	1.91×10^{-11}	1.54×10^{-11}
$\bar{k}_4$ (mol cm^{-2} s^{-1})	1.67×10^{-9}	4.16×10^{-10}	2.84×10^{-10}
$\bar{k}_{-4}$ (mol cm^{-2} s^{-1})	1.69×10^{-12}	3.22×10^{-11}	7.02×10^{-11}
$\bar{k}_5$ (mol cm^{-2} s^{-1})	4.26×10^{-9}	4.43×10^{-9}	9.07×10^{-10}
$\bar{k}_{-5}$ (mol cm^{-2} s^{-1})	3.94×10^{-7}	3.52×10^{-6}	2.25×10^{-6}
α_1	0.18	0.31	0.25
α_2	0.23	0.46	0.36
α_3	0.08	0.05	0.09

Based upon the results obtained from simulation (Table 3), the forward rate constants of the Volmer (k_3) and Tafel (k_5) reactions are found to have the lowest and highest values, respectively, meaning the Volmer reaction could be the rate-determining step. Another notable feature of the data listed in Table 3, is the smaller value of the transfer coefficient of the Heyrovsky reaction compared with the other two. By theory, it is predicted that transfer coefficient can in fact have any value between 0 and 1, based upon the energy states on the reaction coordinate. In terms of the partial charge concept within activated complex theory, the transfer coefficient is a measure of the fraction of the path from the initial state to the final state at which the activated complex occurs. Thus, the activated complex is judged to be more "initial state"-like than "final state"-like. Such a small value for the transfer coefficient has been reported previously in the literature [37].
Double layer capacitance can be calculated by using Eq. (47), as proposed by Hsu and Mansfeld [38],

$$C = Y_0(\omega_m^{"})^{\varphi-1} \qquad (47)$$

In Eq. (47), $\omega_m^{"}$ is the frequency at which the imaginary part of the impedance (Z'') has a maximum value, and Y_0 and φ are CPE-constant and depression angle, respectively, obtained from the simulation results. Table 4 summarizes the double layer capacitance obtained from optimization and calculated based upon Eq. (47) as a function of applied potential for pH = 5.74, 8.00 and 10.00. It can be seen that the magnitude of the double layer capacitance is a little higher compared with the typical values for smooth metallic electrode (e.g. 25 μF cm^{-2}), which could be related to the adsorbed species (i.e., a pseudo-capacitance) on the surface of the electrode or to differences in the roughness of the electrode surface. In fact, if we assume the typical double layer capacitance value of the smooth metallic surface equal to 25 μF cm^{-2} the roughness factor of about 1.22-3.2 for pH=8.00, 10.00 and 1.69-5.38 for pH=5.74 can be readily calculated.

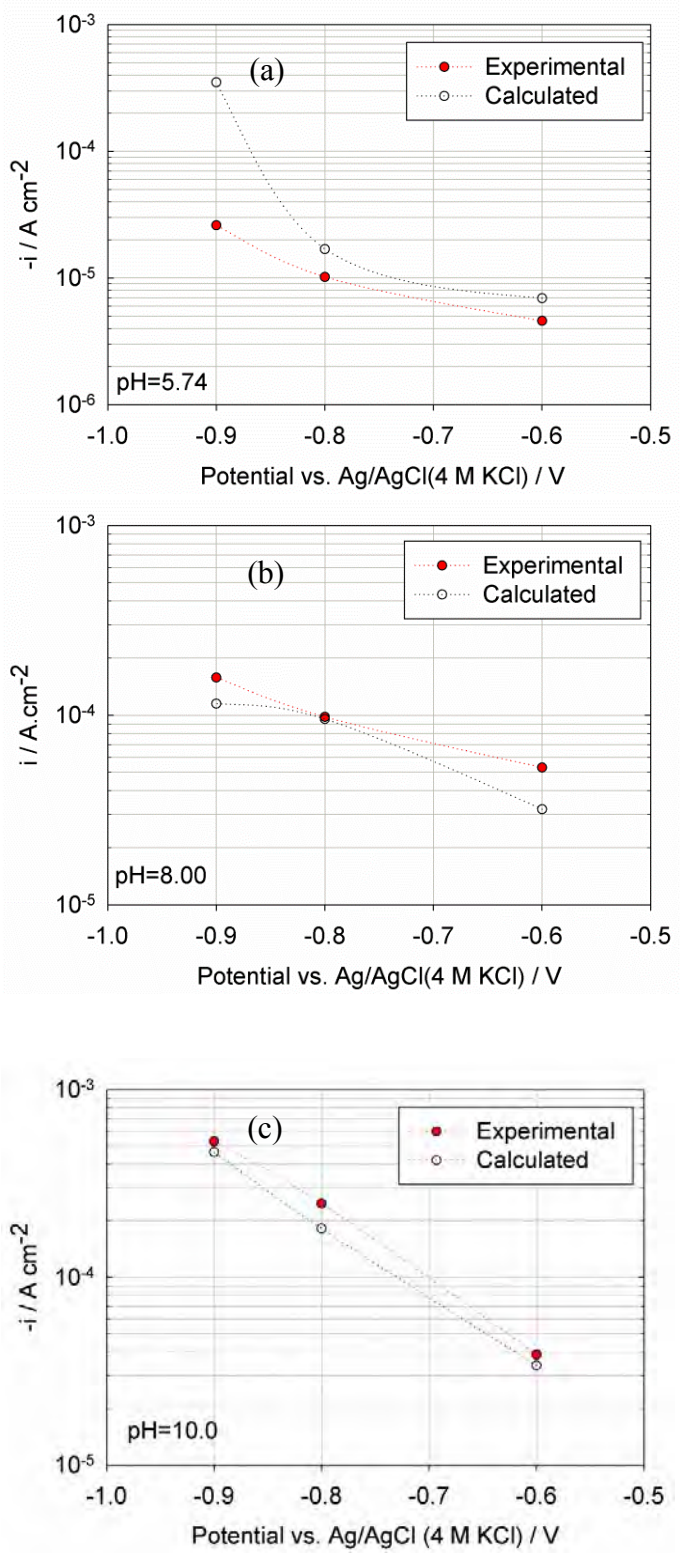

Figure 13. Comparison between experimental and calculated steady-state current as a function of potential (a) pH=5.74, (b) pH=8.00 and (c) pH=10.0.

Table 4. Comparison between obtained double layer capacitance from optimization and Eq. (47)

pH=5.74			
	E_1=-0.600 (V_{ref})	E_2=-0.800 (V_{ref})	E_3=-0.900 (V_{ref})
CPE-Y^0 (S s^{φ} cm^{-2})	8.47×10^{-5}	9.89×10^{-5}	8.95×10^{-5}
CPE-φ	0.74	0.67	0.71
C_{dl} (F cm^{-2})	1.34×10^{-4}	1.05×10^{-4}	4.22×10^{-5}
Roughness factor	5.38	4.19	1.69
pH=8.00			
CPE-Y^0 (S s^{φ} cm^{-2})	4.47×10^{-5}	4.88×10^{-5}	6.77×10^{-5}
CPE-φ	0.93	0.89	0.83
C_{dl} (F cm^{-2})	4.32×10^{-5}	4.36×10^{-5}	5.57×10^{-5}
Roughness factor	1.73	1.74	2.22
pH=10.00			
CPE-Y^0 (S s^{φ} cm^{-2})	3.88×10^{-5}	7.69×10^{-5}	1.09×10^{-4}
CPE-φ	0.80	0.85	0.81
C_{dl} (F cm^{-2})	3.06×10^{-5}	6.03×10^{-5}	7.94×10^{-5}
Roughness factor	1.22	2.41	3.18

4. Summary and Conclusions

- The kinetics of the HER on copper has been studied as a function of temperature, solution pH, and hydrogen pressure. Steady-state polarization using a rotating disk electrode (RDE) was adopted as the primary tool for studying the kinetics of the reaction. As a result, an analytical equation describing the kinetics of the hydrogen evolution reaction has been developed.
- Derived cathodic polarization diagrams calculated using the proposed equation display good agreement with the experimentally-obtained data. The activation energy of the HER on copper is calculated to be ≈ 32 kJ mol^{-1}.
- The exchange current densities and the transfer coefficients can be used in mixed potential models to estimate the corrosion potential and corrosion current density under various conditions and to predict the life time of copper canisters in HLNW repositories.
- The impedance spectra were modeled using a proposed mechanism based upon the Volmer-Heyrovsky-Tafel steps for hydrogen evolution and by considering the reactions involved in hydrogen atom and hydroxyl group adsorption on the copper surface. As a result, a single set of kinetic parameters, including the rate constants and transfer coefficient, has been determined for each pH by optimizing the model on the experimental EIS data. The results have revealed that the HER appears to proceed through the Volmer-Heyrovsky-Tafel mechanism with the Volmer reaction being the rate-determining step. Fairly good correlation is achieved between the experimental and calculated steady-state current as a function of potential showing the viability of the proposed mechanism.

5. References

1. J.O'M. Bockris and A.K.N. Reddy, *Modern Electrochemistry*. Plenum Press, New York, NY, (1970).
2. L. Chen and A. Lasia, *J. Electrochem. Soc.*, **138**(11), 3321–3328 (1991).
3. D. A. Harrington, L. Bai, and B. E. Conway, *Electrochim. Acta*, **32**, 1713-1731 (1987).
4. B. E. Conway, L. Bai and D. Tessier, *J. Electroanal. Chem.,* **161**, 39-49 (1984).
5. J. O'M. Bockris, I.A. Ammar, A. Huq, *J. Phys. Chem.*, **61,** 879-886 (1957).
6. J. O'M. Bockris, A.K.N. Reddy, M. Gamboa-Aldeco, *Modern Electrochemistry* (2nd ed.)Kluwer Academic/Plenum Publishers (2000).
7. A. Lasia, *J. Electroanal. Chem.*, **454,** 115-121 (1998).
8. G.R. Engelhardt, R. Biswas, Z. Ahmed, S.N. Lvov, D.D. Macdonald, *Electrochim. Acta*, **52** (12) 4124-4131 (2007).
9. B. Habibi, M.H. Pournaghi-Azar, H. Razmi, H. Abdolmohammad-Zadeh *Int. J. Hydrogen Energy*, **33,** 2668-2678 (2008).
10. A. Lasia and A. Rami, *J. Electroanal. Chem*., **294**, 123-141 (1990).
11. C. Gabrielli, F. Huet, R.P. Nogueira, *Electrochim. Acta*, **47**, 2043-2048 (2002).
12. P. Los, A. Rami, A. Lasia, *J. Appl. Electrochem.*, **23**, 135-140 (1993).
13. J. O'M. Bockris, N Pentland, *Trans. of the Faraday Soc.*, **48,** 833-839 (1952).
14. J. Garche (Ed.), *Encyclopedia of electrochemical power sources,* Elsevier, **1**, 751-761 (2009).
15. J. O'M. Bockris and R. Parsons, *Trans. of the Faraday Soc.*, **45**, 916-928 (1949).
16. A. C. Ferreira, *J. Appl. Electrochem.*, **18**, 894-898 (1988).
17. H. Kim and Digby D. Macdonald, *Corrosion sci.*, **52**, 1139-1145 (2010).
18. J. Bao, *Ph.D Dissertation in Materials Science and Engineering: Pennsylvania State University*, (2007).
19. A. Davydov, K.V. Rybalka, L. A. Beketaeva, G. R. Engelhardt, P. Jayaweera and D. D. Macdonald, *Corrosion Sci.*, **47**, 195-215 (2005).
20. D. D. Macdonald, A. C. Scott and P. R. Wentrcek, *J. Electrochem. Soc*., **126**(9), 1618-1624 (1979).
21. A. J. Bard and L. R. Faulkner, *Electrochemical Methods: Fundamentals and Applications*, John Wiley & Sons, New York, 2nd edition, (2001).
22. M. Urquidi-Macdonald, S. Real, and D. D. Macdonald, *Electrochim. Acta*, **35** 1559-1566 (1990).
23. D.A. Harrington and B.E, Conway, *J. Electroanal. Chem*., **221**, 1-21 (1987).
24. E. Protopopoff, P. Marcus, *Electrochim. Acta*, **51**, 408-417 (2005).
25. S. Härtinger, B. Pettinger, K. Doblhofer, *J. Electroanal. Chem.* **397**, 335-338 (1995).
26. G. Niaura, *Electrochim. Acta* **45**, 3507-3519 (2000).
27. V. Maurice, H.-H. Strehblow, P. Marcus, *Surf. Sci*. **458**, 185-194 (2000).
28. H.-H. Strehblow, V. Maurice, P. Marcus, *Electrochim. Acta* **46**, 3755-3766 (2001).
29. O. Matsuoka, S.S. Ono, H. Nozoye, S. Yamamoto, *Surf. Sci*. **545**, 8-18 (2003).
30. U. Bertocci, *Electrochim. Acta* **49**, 1831-1841 (2004).
31. S.N. Sivanandam and S.N. Deepa, "Introduction to Genetic Algorithms", *Springer Verlag*, (2007).
32. M. Gulsen, A. Smith and D. Tate, *Int. J. Prod. Res*.,**33**, 1911-1923(1995).

33. T.VanderNoot and I. Abrahams, *J. Electroanal. Chemistry*, **448**(1), 17-23 (1998).
34. O. Kanoun, U. Tröltzsch and H.-R. Tränkler, *Electrochim. Acta* **51**, 1453-1461(2006).
35. "GenCurvefit | IgorExchange." [Online]. Available: http://www.igorexchange.com/project/gencurvefit. [Accessed: 07-Aug-2012].
36. "Ellis 2: Complex curve fitting for one independent variable | IgorExchange." [Online]. Available: http://www.igorexchange.com/project/Ellis2. [Accessed: 07-Aug-2012].
37. D. D. Macdonald, S. Real, S. I. Smedley and M. Urquidi-Macdonald, *J. Electrochem. Soc.*, **135**(10), 2410–2414 (1988).
38. C.H. Hsu and F. Mansfeld, *Corrosion*, **57,** 747-748 (2001).

Corrosion of Copper in Sodium Chloride Solution Containing Sulphide Species

1. Introduction

The Scandinavian plan for disposal of high-level nuclear waste calls for encapsulation of spent fuels in a crystalline bedrock repository at a depth of about 500 m. The current plan calls for emplacement of spent fuels in an inner cast iron insert that is contained in a copper canister with a 50 mm wall thickness [1–3]. After emplacement of the canisters in the boreholes, the remaining space will be backfilled with a compacted bentonite clay buffer [1]. The role of the inner cast iron insert is to provide mechanical strength as well as radiation shielding, while the copper canister (outer layer) role is to provides corrosion protection. Figure 1 shows an exploded view of the cast iron-copper canister designed for boiling water reactor (BWR) fuel. Sweden's KBS-3 plan for the disposal of high-level nuclear waste (HLNW) is partly predicated on the assumption that copper, the material from which the canisters will be fabricated, is thermodynamically immune to corrosion when in contact with pure water under anoxic conditions. In other words, copper is classified as a noble metal-like gold. In the immune state, corrosion cannot occur because any oxidation process of the copper is characterized by a positive change in the Gibbs energy rather than the negative change demanded by the second law of thermodynamics for a spontaneous process [4].

The corrosion evolution of a copper canister can be divided into different stages based on the evolution of the environment and system in contact: (1) corrosion prior to disposal, (2) corrosion after disposal, (3) corrosion during water saturation and (4) corrosion after water saturation. The environment within the proposed repositories is not pristine, pure water, but instead is brine containing a variety of species, including halide ions, sulphur-containing species, and iron oxidation products, as well as small amounts of hydrogen (determined to be about 10^{-11} M by bore-hole sampling). Some of these species are known to activate copper, for example, oxidation of copper in the presence of sulphide produced by dissolution of sulphide minerals (e.g. FeS_2) in the bentonite:

$$2Cu + HS^- \rightarrow Cu_2S + \frac{1}{2}H_2 \qquad (1)$$

Since sulphide species are ubiquitous in the groundwater in Sweden and elsewhere, the controversy raging around whether copper corrodes in pure water is moot.

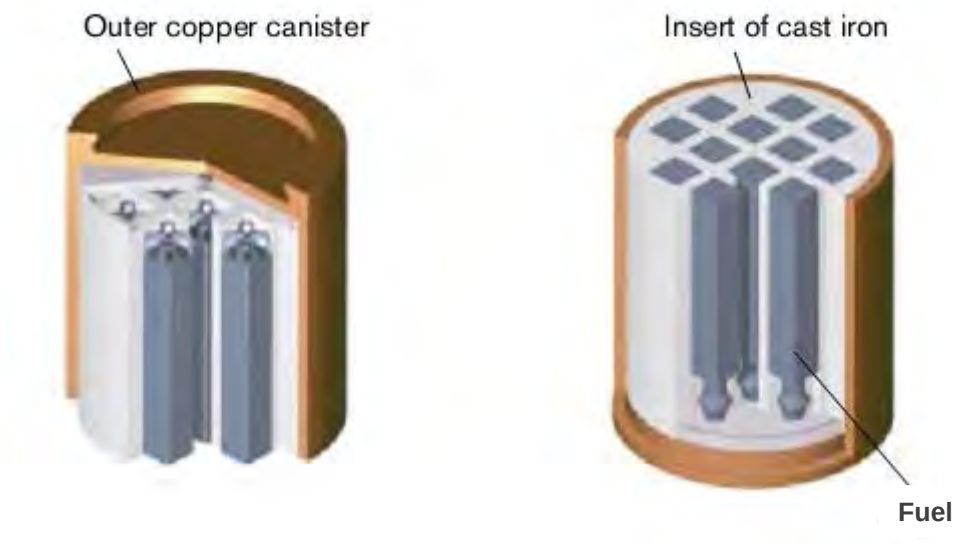

Figure 1. Exploded view of spent BWR fuel disposal canister. [1]

Corrosion of copper alloys (mostly *Cu-Ni* alloys which are common materials used in marine heat exchangers) have been studied extensively in sulphide-polluted environments in the past [5–17], but much less research has focused on the mechanism of pure copper passivity and corrosion in solutions containing sulphide species. The influence of dissolved sulphide species on the electrochemical behavior of copper and its alloys is complex and no satisfactory mechanism has yet been reported.
Several studies of copper corrosion in a sulphide-polluted environment have revealed that copper forms a bilayer corrosion product consisting of an inner Cu_2S layer and a thicker CuS outer layer [15,18,19]. The equilibrium potentials for the electrochemical formation of Cu_2S and CuS are, respectively [15]:

$$2Cu(s) + S^{2-}(aq) \rightleftharpoons Cu_2S(s) + 2e^- \text{ , E=-0.893+0.0295 p } [S^{2-}] \qquad (2)$$

and

$$Cu(s) + S^{2-}(aq) \rightleftharpoons CuS(s) + 2e^- \text{ , E=-0.698+0.0295 p } [S^{2-}] \qquad (3)$$

The most likely cathodic reaction in the presence of sulphide species would be interfacial reduction of bisulphide ions or water. Therefore, based on system conditions (such as pH and potential) de Chialvo and Ariva [15] (from their voltammetry studies) proposed that interaction of copper/sodium sulphide alkaline solution undergoes the following reaction paths: *Cu*/electrolyte → *Cu*/$Cu_{1.8}S$/electrolyte → *Cu*/$Cu_{1.8}S$/Cu_2S/electrolyte → *Cu*/$Cu_{1.8}S$/Cu_2S/*CuS*/electrolyte. They concluded that cupreous sulphide (Cu_2S) is dominantly formed at potentials lower than -0.6 V *vs.* SHE while cupric sulphide (*CuS*) forms after long electrolysis in potentials higher than the equilibrium potential for Reaction (3).
The work of Macdonald et al. [20] also suggested the formation of a duplex sulphide film on *Cu-Ni* alloys in a deaerated sea water solution containing sulphide species. Syrett [8], on the other hand, reported that the bilayer film consists of an oxide inner layer and the presence of sulphide species in the solution will result in the formation of a Cu_2S (or $Cu_{2-x}S$) outer layer. This bilayer structure comprising an inner oxide layer and a sulphide outer layer is likely to been seen in a repository once the initially trapped oxygen has been consumed during the first oxic period and the system becomes more reducing in the next anoxic period.

Based on the thermodynamic information of the system, Macdonald et al. [21] postulated that the presence of sulphide species in a sea water solution will shift the corrosion potential to more active values (Figure 2) that could satisfy the thermodynamic criteria for spontaneous anodic dissolution of copper with respect to hydrogen evolution as the cathodic partial reaction.

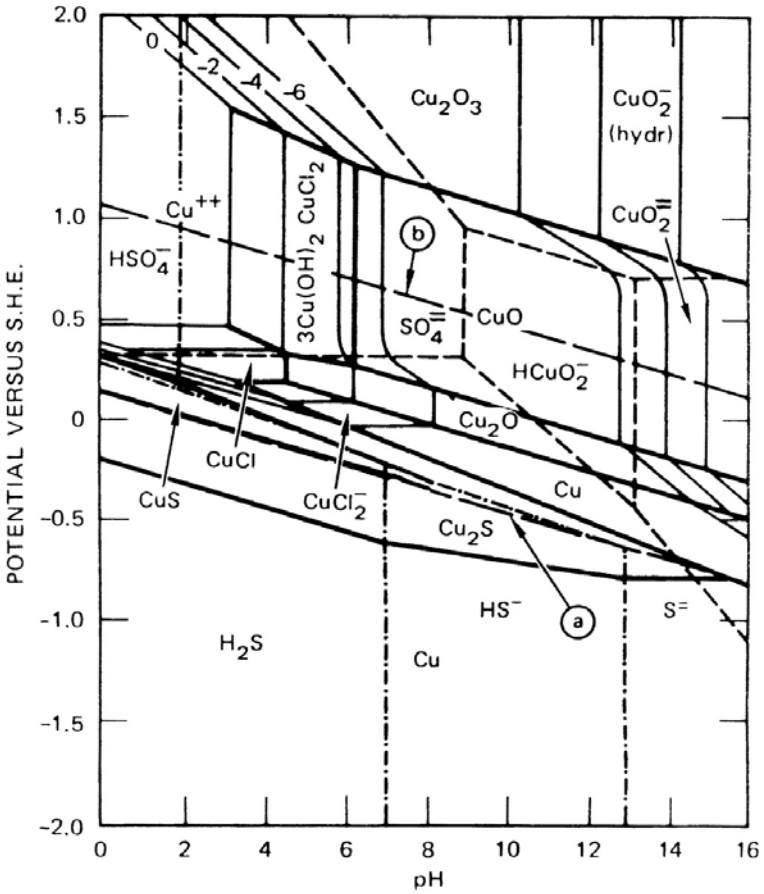

Figure 2. Potential-pH diagram for copper in sea water containing 4 mg lit^{-1} dissolved sulphide at 25°C. The equilibrium lines for hydrogen evolution (line a) and oxygen evolution (line b) have been drawn for gas partial pressures of 10^{-5} atm. [21]

Recently, several studies on the corrosion and electrochemistry of copper in sulphide-polluted environments have been published [22–28]. These studies were performed in sodium chloride solutions containing different concentrations of sulphide species that are expected to be present in the repository in Sweden.

Chen et al. [22] studied the kinetics of the copper corrosion in a neutral sodium chloride solution containing a small concentration of sulphide ions as a function of time in an open circuit potential condition. They proposed that low corrosion potential observed as a result of the presence of sulphide species in the solution could be attributed to the adsorption of HS^- on the surface of the copper electrode, resulting in the production of adsorbed Cu^+ species through a two-step reaction process, with the second step being the rate determining,

$$Cu + HS^- \rightleftharpoons Cu(HS)_{ads} + e^- \quad (4)$$

$$Cu + Cu(HS)_{ads} + HS^- \rightleftharpoons Cu_2S + H_2S + e^- \quad (5)$$

The overall reaction would be completed with the reduction of water as a cathodic reaction. Their results revealed that while chloride ions can influence the morphology of the copper sulphide deposits, there is no evidence of its role on copper dissolution reaction. Combined electrochemical and morphological studies in their work have shown that the corrosion film formed on the copper surface consisted of a single layer of Cu_2S, and its thickness increased with immersion time and had a non-uniform nature [22].
The objective of this part of the study is to explore the electrochemical/corrosion behavior of a pure copper electrode in a sodium chloride solution containing sulphide species at different temperatures as well as the surface characterization of the film and its semiconductive character. The ultimate goal is to develop an impedance model, based on the Point Defect Model (PDM) and extracting the kinetic data for copper sulphide passive film formation and dissolution which can be used in mixed potential models to estimate the corrosion potential and corrosion current density under various conditions and to predict the life span of copper canisters in HLNW repositories.

2. Experimental

All experiments were carried out in a typical double-wall three electrodes electrochemical cell. The working electrode was a pure copper (*Puratronic*®, 99.999% *Alfa Aesar*®) cylinder mounted in epoxy resin with a 0.78 cm^2 area exposed to the solution. The electrode surface was abraded to a mirror finish with 600, 800 and 1200 *SiC* paper and then further polished with 0.05 μm alumina. After polishing, the electrode was rinsed with acetone and doubly distilled water (18.3 MΩ cm^{-1}, *mili-Q*) to remove any residual alumina. The electrolyte was made from a different concentration of *NaCl* and $Na_2S.9H_2O$ using doubly distilled water (18.3 MΩ cm^{-1}, *mili-Q*). The electrolyte was deaerated prior to the experiment with ultra-high purity nitrogen (UHP, 99.999%) for approximately four hours prior to the experiments and a slow flow of nitrogen was maintained during the experiments. The counter electrode was a *Pt* wire, and all potentials were measured against a silver/silver chloride electrode (*Ag/AgCl* (in 4M *KCl*)) that was connected to the cell via a Luggin probe. All the potentials reported in this chapter have been recalculated to the standard hydrogen electrode (SHE) scale. The working electrode was initially reduced potentiostatically at -1.2 V *vs. Ag*/*AgCl*(4M *KCl*) for 5 min to remove any air-formed oxide on the surface of the electrode and then the passive films were grown potentiostatically for 48 h (24h at 75 ^oC) before initiating the measurements.

For Mott-Schottky analysis, capacitance measurements of passive film formed on copper electrodes were carried out by stepping the potential in the negative direction from the film formation potential, while simultaneously imposing a small amplitude sinusoidal voltage perturbation (10mV peak-to-peak) at a frequency of 3 kHz using a Gamry Instrument (PC3 Potentiostat/Galvanostat/ZRA). The potential step of 0.025 V was sufficiently fast to ensure that the defect structure of the passive film was "frozen-in" and, hence, that the defect density and the barrier layer thickness would not be a function of potential. The corresponding capacitance of the space charge then was calculated from the imaginary part of the impedance from $C_{SC} = -\frac{1}{\omega Z''}$ where ω is the angular frequency. It is assumed that the double layer capacitance is sufficiently large that it can be neglected in a series representation of the capacitance of the interface.

The impedance data were collected under the steady-state potential in the passive potential range after 48 h, ensuring the stability of the system as required by electro-

chemical impedance spectroscopy (EIS). Measurements were performed using a Gamry Instrument (PC3 Potentiostat/Galvanostat/ZRA) under excitation potential of 10 mV (peak-to-peak) over the frequency range from 5 kHz to 0.01 Hz, with the impedance being measured at 10 frequencies per decade. The EIS data were analyzed using *Igor Pro* software.

An X-ray photoelectron spectroscopy (XPS) analysis was performed with a Kratos Analytical Axis Ultra Spectrometer, using an *Al* K_α X-ray source. Sulphide film was first grown at -0.295 V *vs.* SHE formation potentials for 24 hours, and then rinsed with deionized water and dried in the nitrogen gas flow. The samples were then transferred to the sample introduction compartment of the XPS spectrometer. A survey spectrum was first recorded to identify all elements presented on the surface, and then high resolution spectra of the following regions were recorded: *Cu*-2p, *O*-1s, *S*-2p and *C*-1s.

3. Results and Discussion

3.1. Potential-pH diagrams

In order to predict the relative stability of different dissolved species and solids as a function of pH and redox potential, simplified Pourbaix (Eh-pH) diagrams have been derived for different conditions. Figure 3 shows a series of potential-pH diagrams for the $Cu/Cl^-/S/H_2O$ system at 25°C as a function of chloride concentrations.

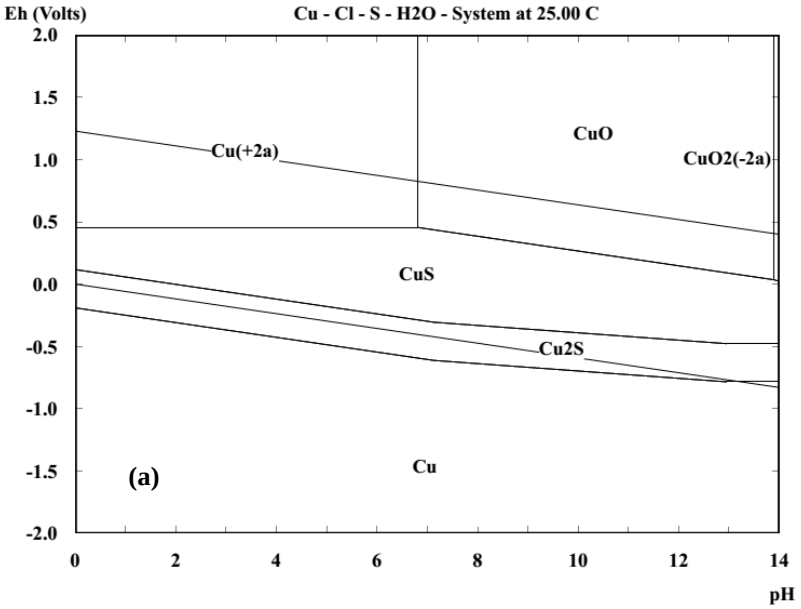

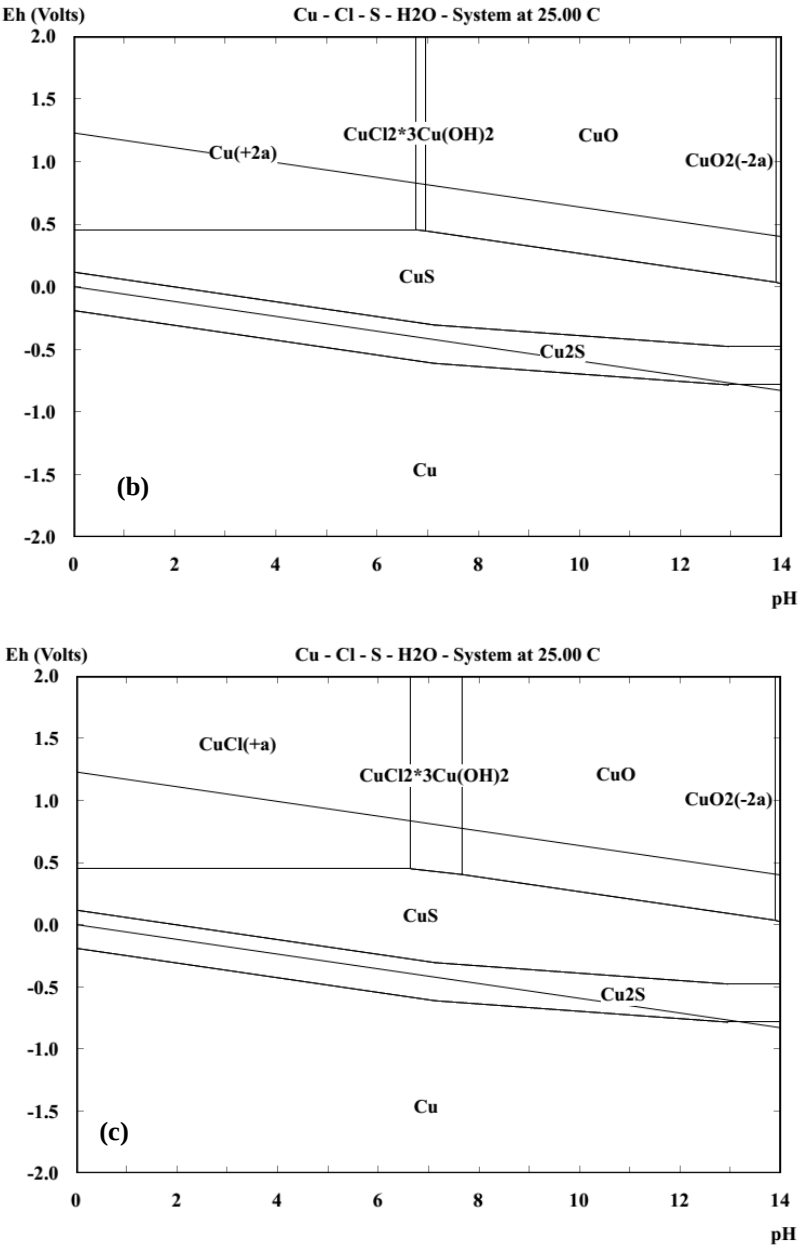

Figure 3. Potential/pH (Pourbaix) diagrams for the system $Cu/Cl^-/S/H_2O$ at 25°C for various chloride concentrations. (a)10^{-2} mol kg^{-1}, (b)0.1 mol kg^{-1}, (c) 0.5 mol kg^{-1}. All diagrams constructed for a total dissolved copper concentration of 10^{-6} mol kg^{-1} and [*S*]=2×10^{-4} mol kg^{-1} using the Outokumpu thermodynamic database [29]. Solid species considered: *Cu, Cu_2O, CuO, $Cu(OH)_2$, CuS, Cu_2S* and *S*; dissolved species considered: Cu^+, Cu^{2+}, $CuCl_2^-$, $CuCl_3^{2-}$, $CuCl^+$, $CuCl_3^-$, $CuCl_4^{2-}$, CuO_2^{2-}, H_2S, HS^-, S^{2-}, $CuCl_2*3Cu(OH)_2$ and $HCuO_2^-$. In the diagrams, the number in parentheses indicates the charge of dissolved ions.

As seen in Figure 3, both Cu_2S and *CuS* solids dominate over the entire pH and potential ranges expected in the repository in Sweden and chloride seems not to have any effect on their stability at least from a thermodynamic point of view. Increasing the chloride concentration from 0.1 mol kg^{-1} to 0.5 mol kg^{-1} has the largest effect at neutral and acidic pH, with $CuCl^+$ becoming more stable than Cu^{2+} ions.

Figure 4 shows a simplified potential-pH diagram for the $Cu/S/Cl^-/H_2O$ system at three different temperatures for a total *S* concentration of 2×10^{-4} mol kg^{-1}, a total *Cu* concentration of 1×10^{-6} mol kg^{-1}, and a total Cl^- concentration of 0.1 mol kg^{-1}. It is

evident that temperature does not have any major effect over the entire potential and pH region expected in the repository and both Cu_2S and CuS are dominating species. By increasing the potential, CuS becomes the stable, solid phase and CuO will only form at relatively positive potentials. It also found out that sulphide concentration (not shown here) does not have a major impact on the observed behavior and can only shift the $Cu/Cu_2S/CuS$ boundary to more positive potentials at lower sulphide concentrations.

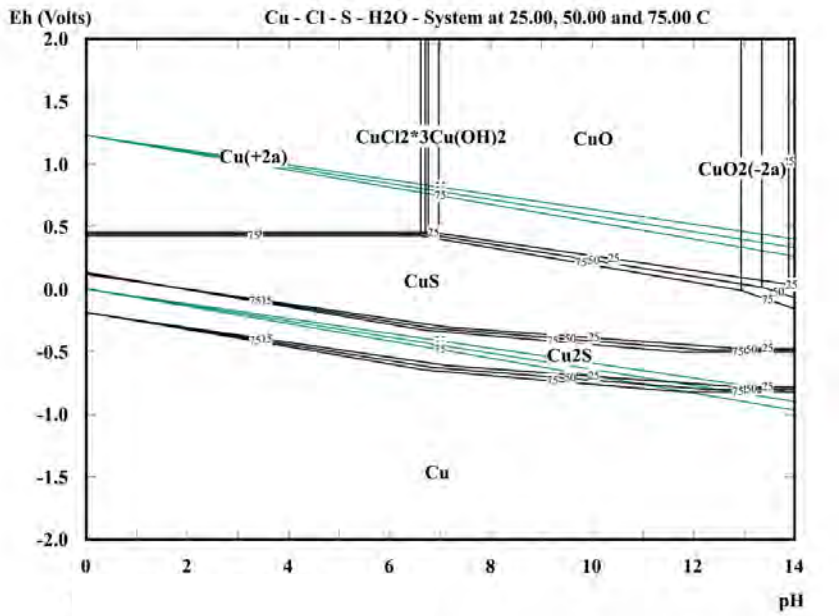

Figure 4. Potential/pH (Pourbaix) diagrams for the system $Cu/Cl/S/H_2O$ as a function of temperature. All diagrams constructed for a total dissolved [Cu]=10–6 mol kg^{-1}, [Cl]=0.1 mol kg^{-1} and [S]=2×10^{-4} mol kg^{-1} using the Outokumpu thermodynamic database [29]. Solid species considered: *Cu, Cu_2O, CuO, $Cu(OH)_2$,CuS, Cu_2S and S;* dissolved species considered: Cu^+,Cu^{2+},$CuCl_2^-$,$CuCl_3^{2-}$, $CuCl^+$,$CuCl_3^-$, $CuCl_4^{2-}$, CuO_2^{2-}, H_2S, HS^-, S^{2-} ,$CuCl_2$*$3Cu(OH)_2$ and $HCuO_2^-$. In the diagrams, the number in parentheses indicates the charge of dissolved ions.

3.2. Potentiodynamic polarization

3.2.1. Effect of chloride concentration

Figure 5 shows the potentiodynamic polarization of copper in a deaerated $NaCl$+2×10^{-4} M $Na_2S.9H_2O$ solution at different chloride concentrations. It is evident that chloride plays an important role in the passivity breakdown potential because as its concentration increases from [Cl^-]=0.01 M to 0.5 M the breakdown potential drops about -0.2 V from around E_b=0.2 V *vs.* SHE at [Cl^-]=0.01 M to around E_b=0 V *vs.* SHE at [Cl^-]=0.5 M. The Point Defect Model, PDM, postulates that the role of aggressive ions such as chloride on passivity breakdown is to increases the flux of metal vacancies (in the p-type passive films) through the barrier layer and subsequent condensation of cation vacancies at the metal/film interface[30,31]. One can see that the chloride concentration does not play an important role in the passive current density. As a result, a chloride concentration equal to 0.1 M has been selected for the rest of this study as it is more relevant to the practical conditions in the repository. Kear *et* al. [32] have reviewed the role of the chlo-

ride ion on the corrosion and electrochemical mechanisms of unalloyed copper in aqueous solutions and the reader is referred to that article for more information.

3.2.2. Effect of temperature

Figure 6 displays the potentiodynamic polarization of copper in a deaerated 0.1 M *NaCl*+2×10^{-4} M $Na_2S.9H_2O$ solution at 25°C, 50°C, and 75°C. A wide passive range potential of roughly -0.6 (potential which is related to the formation of copper sulphide) to 0 V *vs.* SHE for 50°C and 75°C and to 0.2 V *vs.* SHE for 25°C is observed. It is evident that the effect of temperature on passive current is minor, although it shows the greater impact on the cathodic branch and passivity breakdown potential. The effect of solution temperature on the transient current of copper when its potential is stepped to -0.295 V *vs.* SHE is shown in Figure 7. One can see that the net current decreases with time until finally it reaches its steady-state value. Interestingly, as temperature increased from 50°C to 75°C, observed net current decreased even more with time, which could be attributed to the increase in the rate of any cathodic reaction(s) participating in the overall net current. Thus, one can conclude that the cathodic reaction(s) is possibly the rate-determining step while the anodic reaction controls the potential. Similar trends were observed in the rest of the applied potentials.

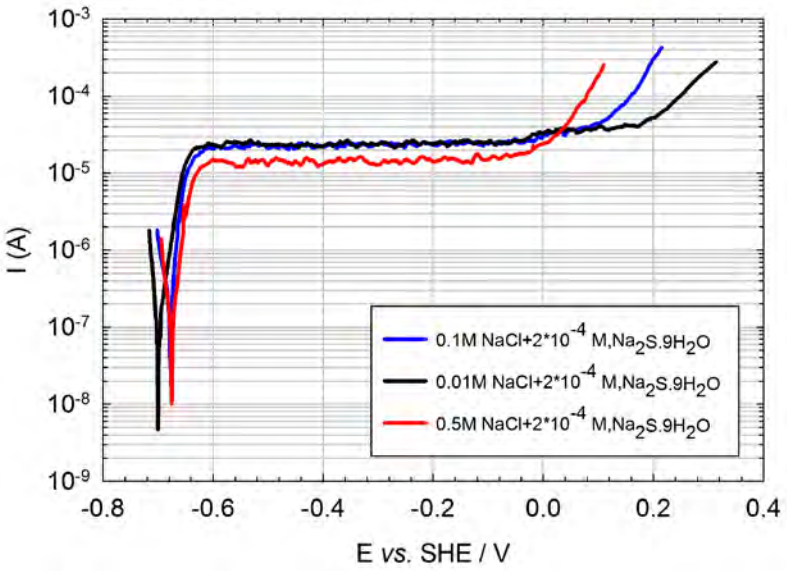

Figure 5. Potentiodynamic polarization curves of *Cu* in a deaerated *NaCl*+2×10^{-4} M $Na_2S.9H_2O$ solution at ambient temperature (25°C) as a function of chloride concentration. (Scan rate=1 mV s^{-1})

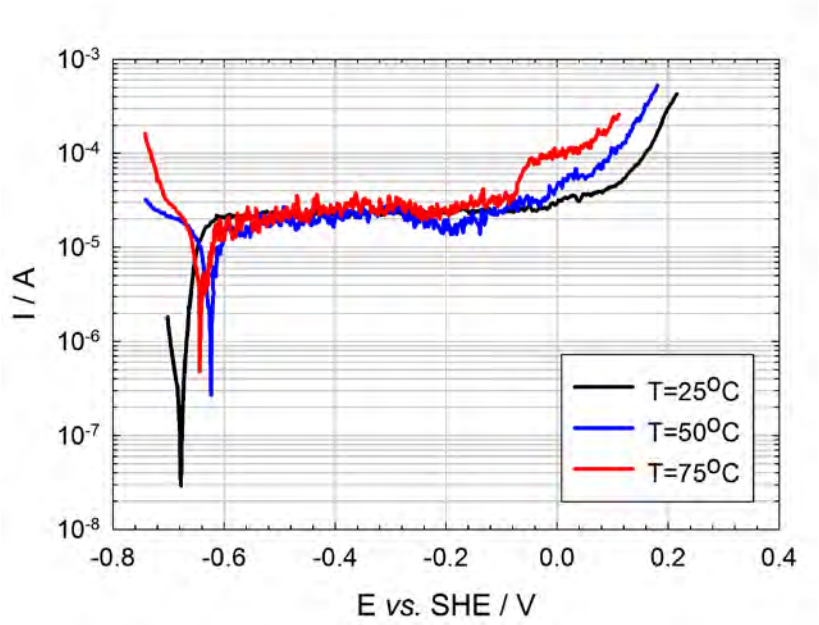

Figure 6. Potentiodynamic polarization curves of *Cu* in a deaerated 0.1 M *NaCl*+2×10^{-4} M $Na_2S.9H_2O$ solution as a function of temperature. (Scan rate=1 mV s^{-1})

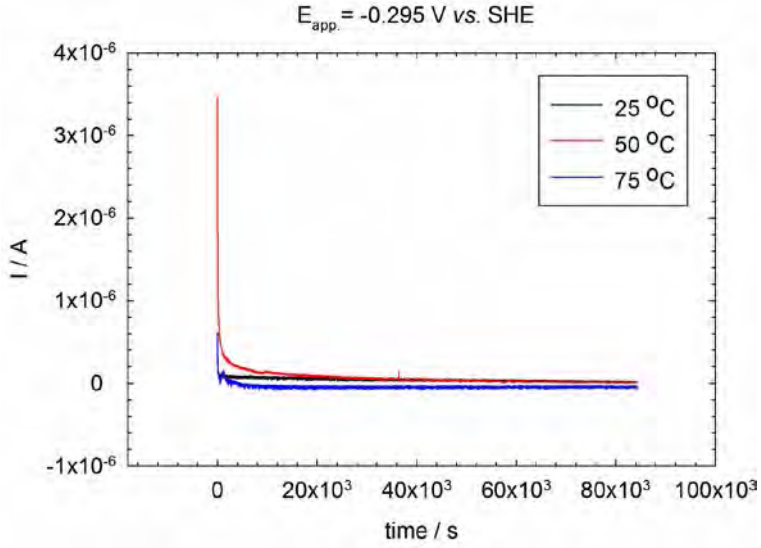

Figure 7. Potentiostatic current transients of *Cu* in a deaerated 0.1M *NaCl*+2×10^{-4} M $Na_2S.9H_2O$ solution as a function of temperature at -0.295V vs. SHE for 24h.

3.2.3. Effect of sulphide concentration

The potentiodynamic polarization and current transient behavior of copper in 0.1 M *NaCl* solution as a function of sulphide concentration at room temperature are presented in Figures 8 and 9. It is evident that the increase of the sulphide concentration from 2×10^{-4} M to 4×10^{-4} M does not have a major impact on the anodic behavior of the copper electrode. However, with the increase of the concentration to 2×10^{-3} M, not only did we observe a major shift in passive current, but we also saw the open circuit potential shift to more negative potentials. The passivity potential region is quite similar for all sulphide concentrations starting roughly at -0.6 V up to approximately 0.1-0.2 V *vs.* SHE and no clear active dissolution could be discerned in these curves. It should be mentioned that as the concentration of sulphide species

increased, the pH of the electrolyte also increased (higher alkalinity). So, apparently as a result of the increase in sulphide concentration and a higher alkalinity, passive film becomes less protective and more porous. In fact, at the highest concentration of sulphide (e.g. 2×10^{-3} M), the observed passive current is around 2×10^{-4} (A), which is much bigger than the typical passive current. In addition, as can be seen from the transient current curve, at this concentration, the observed current is fluctuating during the whole time, which could be attributed to any localized phenomenon such as pitting or passivation/repassivation incidents. Also, in Figure 9, two current peaks have been observed during the experiment time, which are related to the sulphide film removal from the surface of the electrode and growth of a fresh sulphide film.

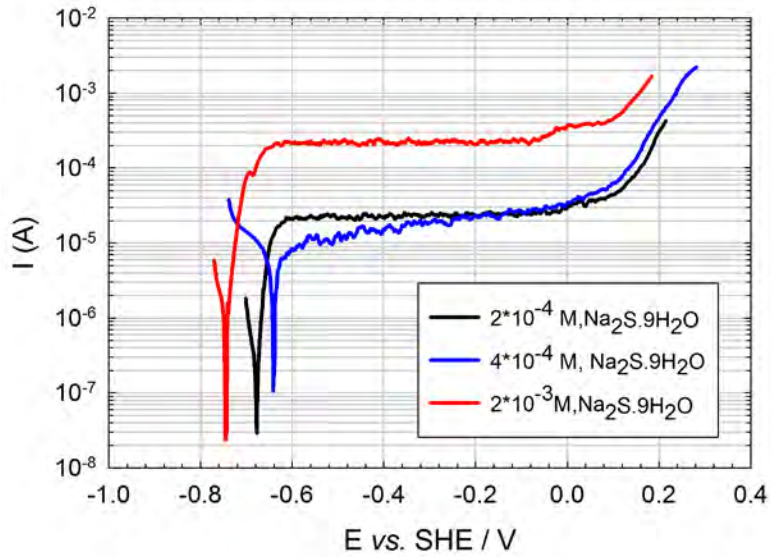

Figure 8. Potentiodynamic polarization curves of *Cu* in a deaerated 0.1 M *NaCl* solution as a function of sulphide concentration at ambient temperature.(Scan rate=1 mV s^{-1})

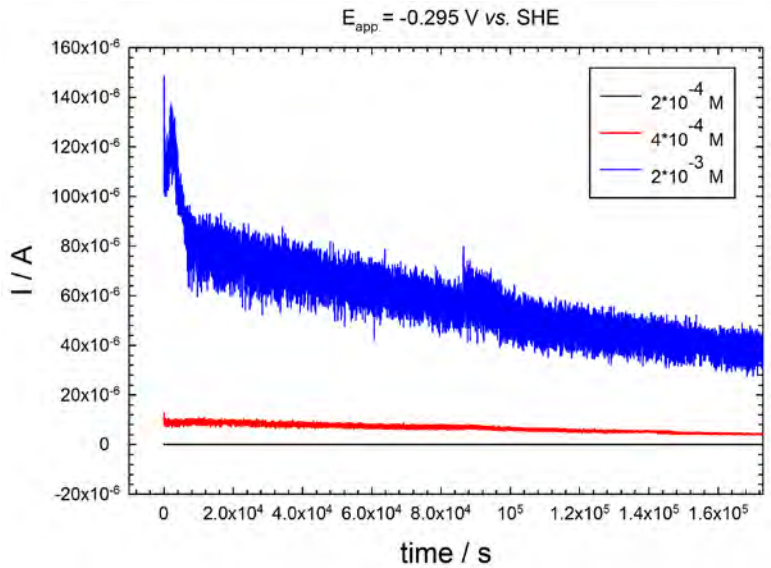

Figure 9. Potentiostatic current transients of *Cu* in a deaerated 0.1 M *NaCl* solution as a function of sulphide concentration at -0.295V vs. SHE for 48h.

3.3. Mott-Schottky Analysis

In order to examine the electronic properties of the sulphide passive film that forms on copper in deaerated 0.1 M *NaCl*+2×10^{-4} M $Na_2S.9H_2O$ Mott-Schottky analysis was performed as a function of temperature. This in situ technique can provide qualitative and quantitative properties of semiconductors, such as type of semiconductor, density of defects, flat band potential, and bandgap energy. Although this technique is a useful method for characterizing the semiconductor-solution interface, it must be used with caution because the electrochemically grown semiconductors often do not meet the ideal conditions on which the Mott-Schottky (M-S) equation is based. These kinds of semiconductors generally have an amorphous structure and their band gap contains localized energy states that may give rise to a frequency dependence of the space charge capacity. This phenomenon is related to the different time constants for the charging and discharging of these localized energy states. Generally, it is agreed that the capacitive behavior of the passive film/electrolyte interface is analogous to that of a semiconductor/electrolyte interface [33]. In this technique (M-S), the inverse of the space charge capacitance (C_{sc}^{-1}) in a semiconductor is measured as a function of applied potential across it. Similar to the metal-liquid interface, a double layer of charge exists at the semiconductor-liquid interface as a result of ion or molecule adsorption, oriented dipoles, etc. A diffuse double layer could exist in dilute solution as well; however, it can be neglected at sufficiently high ion concentration. On the other hand, in the semiconductors, counter charges such as electrons, holes, and ionized donor and acceptor states not only located at the interface (as in a metal), but are distributed over a finite distance below the surface; the reason for that is lower carrier density in the semiconductors than in the metals. This region in the semiconductors, where charge is distributed, is called the space charge layer [34]. The existence of the space charge capacitance is due to the charge separation within the semiconductor when potential is applied. In the case of examining passive films in the aqueous system, measured capacitance comprises several capacitances (e.g., Helmholtz layer capacitance, outer layer capacitance) in series and the smallest one dominates the capacitance of the junction. As we know, different type of defects could exist within the barrier layer, including cation vacancies, cation interstitials, and anion vacancies based on the type of semiconductor and the concentration (according to the PDM) [35].

In conformity with the Mott-Schottky theory, the space charge capacitance of a semiconductor is expressed as,

$$\frac{1}{C_{sc}^2} = \frac{-2}{\varepsilon\varepsilon_0 e N_A}\left(V - V_{FB} + \frac{kT}{e}\right) \quad \text{for p-type semiconductor} \qquad (6)$$

$$\frac{1}{C_{sc}^2} = \frac{2}{\varepsilon\varepsilon_0 e N_D}\left(V - V_{FB} + \frac{kT}{e}\right) \quad \text{for n-type semiconductor} \qquad (7)$$

where "ε" is the dielectric constant of the passive film (assumed to be equal to 16 here), "ε_0" is the vacuum permittivity (8.854×10^{-14} F cm^{-1}), "e" is the electron charge (1.602×10^{-19} C), "k" is the Boltzmann constant (1.38×10^{-23} J K^{-1}), "V" is the applied potential, "V_{FB}" is the flat band potential, "T" is the temperature (K), "N_A" is the acceptor density (cm^{-3}), and "N_D" is the donor density (cm^{-3}). Therefore, the C_{sc}^{-2} vs. V plot should be linear with a negative slope for p-type semiconductors, while that for the n-type should have a positive slope.

Figures 10 through 12 display the Mott-Schottky plots for the passive sulphide film formed on copper potentiostatically in a deaerated 0.1 M *NaCl*+2×10^{-4} M $Na_2S.9H_2O$ solution at -0.395 V *vs.* SHE at different solution temperatures. As can be seen, at 25^{o}C and 50^{o}C, the plots of C^{-2} *vs.* potential indicate the existence of two

distinctive regions. A positive slope is seen for potentials lower than approximately -0.6 V *vs.* SHE, denoting that the film behaved like n-type semiconductor. For applied potentials higher than -0.6 V *vs.* SHE, a negative slope was observed, suggesting p-type semiconductive behavior. From the potentiodynamic polarization results described earlier in this section, the passive film does exist in the potential range between -0.6 to 0 V *vs.* SHE so that the p-type character observed at potentials higher than -0.6 V *vs.* SHE can be attributed to the electronic character of the passive sulphide film, which is consistent with the result reported on copper sulphide thin films [36]. The n-type character observed at more negative potentials can be attributed to other electrochemical/chemical reactions, such as reduction of water at the electrode/solution interface or change of defects concentration as a result of potential change. For quantitative analysis, however, we only considered the potentials in the passive range (E > -0.6 V *vs.* SHE). At 75°C, on the other hand, a negative slope for the majority of the applied potentials was observed indicating that cation vacancies are the dominant defects in the passive film and consequently the passive film behaves like a p-type semiconductor. Acceptor density can be calculated from fitting of Eqs. (6) and (7), and the results as a function of potential and temperature are shown in Table 1 and Figure 13. It is evident from Figure 13 that the acceptor density is almost constant at 25°C for the entire potential range, while in case of 75°C it increases with increases in potential. At 50°C, however, we observed an increase up to -0.3 V *vs.* SHE and a decrease after that. Another point to notice is the increase of defect density as a result of increasing the temperature to 75°C, especially at higher potentials.

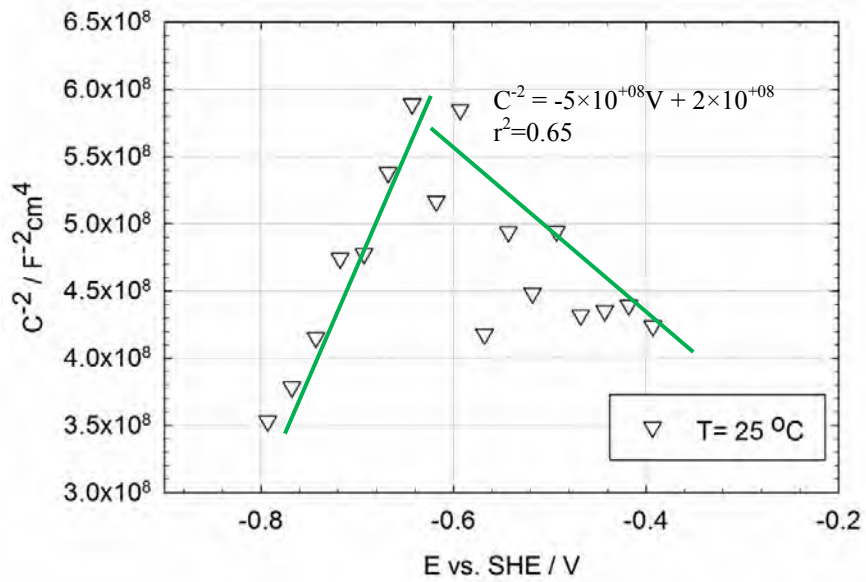

Figure 10. Mott-Schottky plot for the passive film formed on copper at -0.395 V vs. SHE in a deaerated 0.1M, *NaCl* + 2×10^{-4}M, $Na_2S.9H_2O$, at T=25°C.

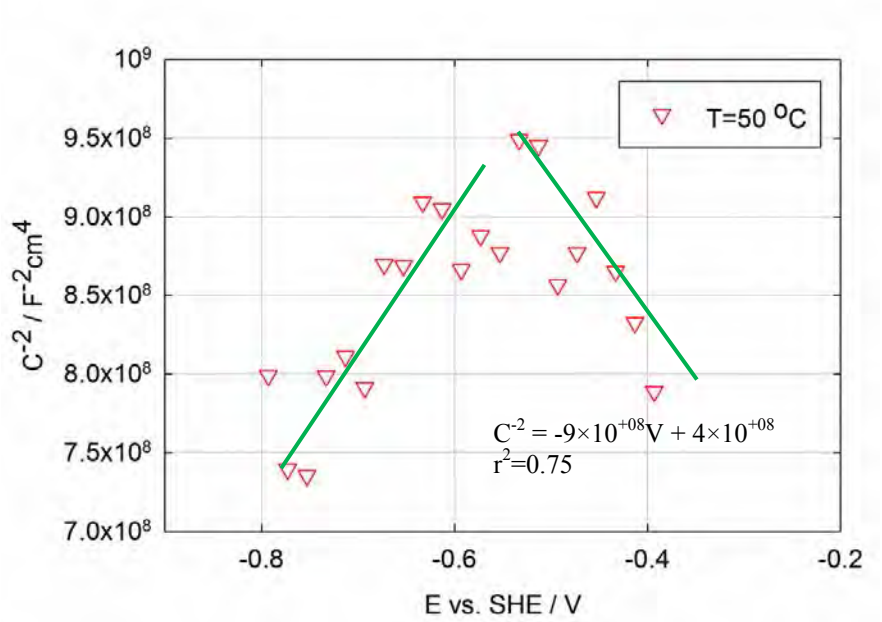

Figure 11. Mott-Schottky plot for the passive film formed on copper at -0.395 V vs. SHE in a deaerated 0.1M, *NaCl* + 2×10^{-4}M, $Na_2S.9H_2O$, at T=50°C.

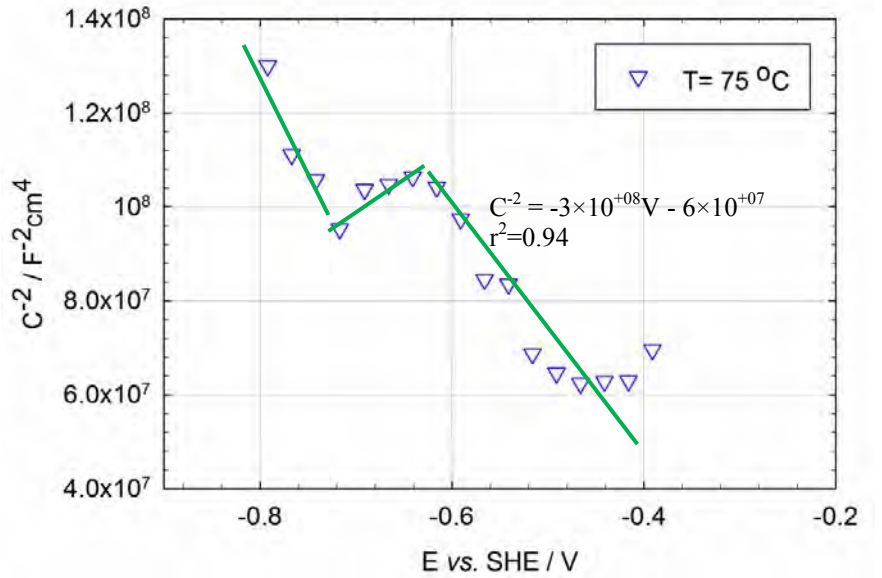

Figure 12. Mott-Schottky plot for the passive film formed on copper at -0.395 V vs. SHE in a deaerated 0.1M, *NaCl* + 2×10^{-4}M, $Na_2S.9H_2O$, at T=75°C.

Table 1. Acceptor density (N_A) of the passive film formed at E=-0.295 V vs. SHE at different temperatures.

T (°C)	25	50	75
N_A (cm^{-3})	$8.82\times10^{+21}$	$4.41\times10^{+22}$	$1.26\times10^{+23}$

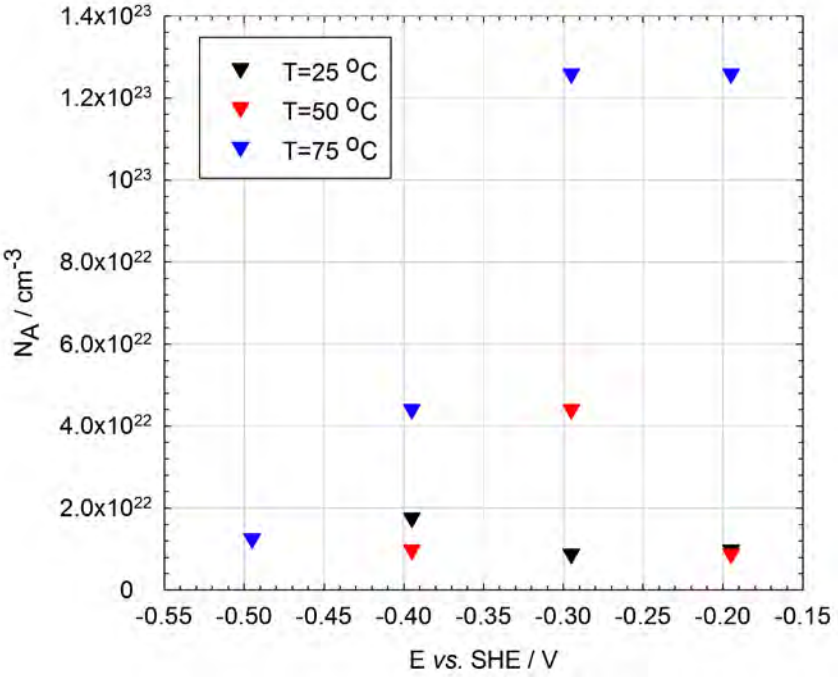

Figure 13. Variation in defect density with potential as calculated by the Mott-Schottky slopes at different temperatures.

3.4. XPS Analysis of the Sulphide Passive Film on Copper

The Surface of the copper sulphide passive film formed electrochemically in a de-aerated 0.1 M $NaCl$+2×10^{-4} M $Na_2S.9H_2O$ solution at $E_{app.}$=-0.295 V *vs.* SHE was examined by X-ray photoelectron spectroscopy (XPS) measurement. Figure 14 shows the survey spectra of the sulphide film on copper. As can be seen, *Cu*, *S*, *O,* and *C* were detected on the surface of the passive film. The presence of carbon and oxygen is generally attributed to contamination, and air formed an oxide layer during the handling of the samples. It should be mentioned that the surface of the sulphide film was not homogenous, therefore no quantitative analysis were performed in this study.

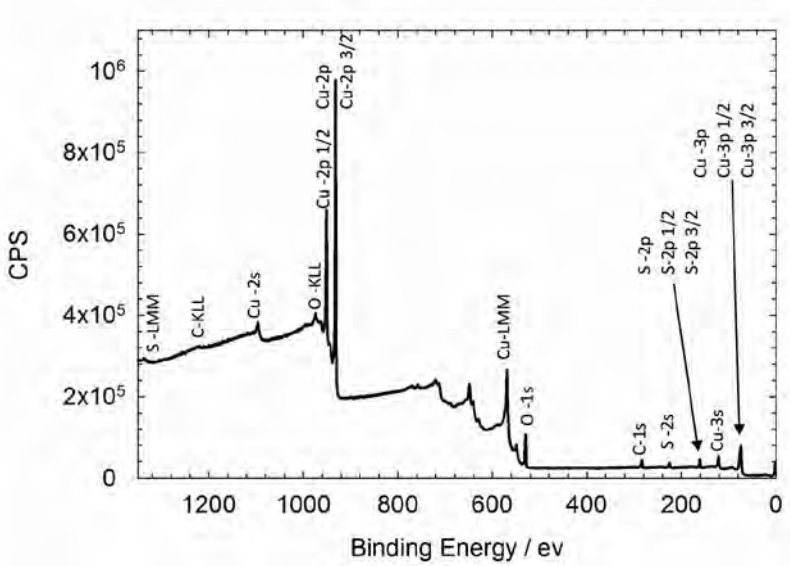

Figure 14. XPS survey spectra of the *Cu-2p* recorded at 90° for the passive sulphide film on copper formed in a deaerated 0.1 M *NaCl*+2×10^{-4} M $Na_2S.9H_2O$ at 25°C.

The high resolution XPS spectrum of the *Cu*-2p is shown in Figure 15. The key feature of the spectra is the presence of the "shake-up" satellite at ca. 944 eV. It is known that when a core electron is being ejected, there is a probability that a valence electron will be simultaneously excited to an empty orbital level during the relaxation process. If this phenomenon occurs in the process, the photoelectron must be ejected with less energy, resulting in a shift in the XPS peak to apparently higher binding energy. These "shake-up" satellites are normally weak since the probability of their occurrence is very low; however, in some cases, they could be as strong as the "main" peaks. Since the valence level electrons are involved in this process, the "shake-up" structure can provide chemical state identification [37]. The presence of this "shake-up" structure in the XPS spectrum of *Cu*-2p was attributed to the presence of divalent copper [38], while others detected this "shake-up" satellite in both Cu_2S and *CuS* compounds and argued that this occurrence is consistent with other diamagnetic species. [39]

A high-intensity peak at 932.1 eV is close to the reported peak position of *CuS* (932.2 eV) [40] and Cu_2S (932.5 eV) [41] which means that both compounds were likely presented in the passive film. It is postulated that a clearer distinction between these two compounds can be obtained by analyzing copper Auger peaks. The *Cu*-LMM peak position at 917.6 eV coincides with known Cu_2S and *CuS* peak positions, which makes it difficult to distinguish either of the compounds from each other (917.3 eV, 917.9 eV, respectively) [38,39].

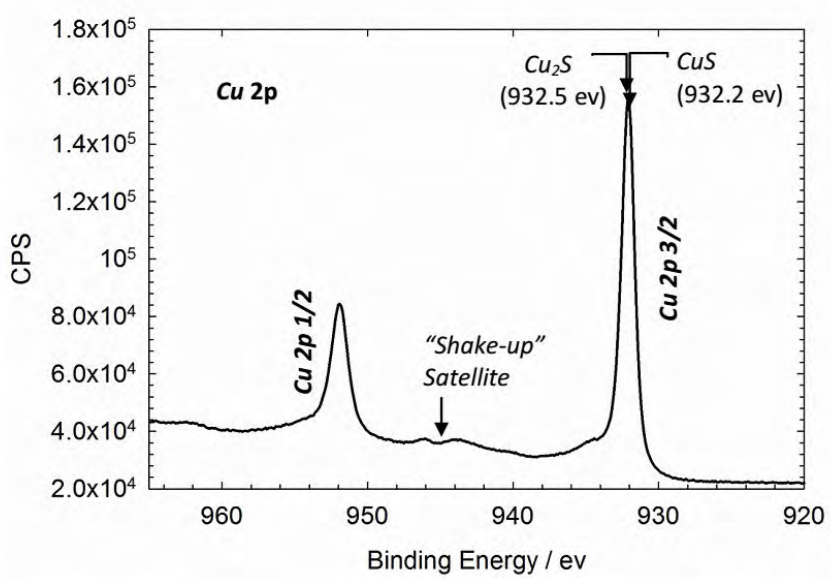

Figure 15. High resolution XPS spectra of the *Cu-2p* recorded at 90° for the passive sulphide film on copper formed in a deaerated 0.1 M *NaCl*+2×10^{-4} M $Na_2S.9H_2O$ at 25°C.

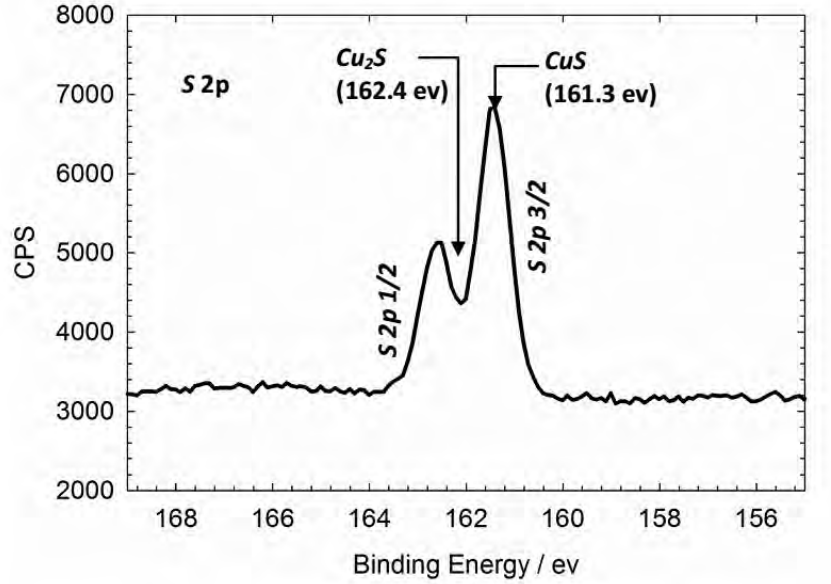

Figure 16. High resolution XPS spectra of the *S-2p* recorded at 90° for the passive sulphide film on copper formed in a deaerated 0.1 M *NaCl*+2×10^{-4} M $Na_2S.9H_2O$ at 25°C.

A high resolution XPS spectrum of *S*-2p is shown in Figure 16. This spectrum shows more promising results in terms of the surface analysis of the passive film. The observed peak position in the spectrum is in good agreement with known *CuS* and Cu_2S positions (161.3 eV and 162.4 eV, respectively) [42,43], while it is closer to the *CuS* peak reported previously in the literature [39]. From a structural point of view, Cu_2S consists of only S^{2-} ligands, but *CuS* consists of both S^{2-} and S_2^{2-} ligands. Therefore, sulphur in the *CuS* spectrum is a composite of a doublet of doublet (the 2p spectrum of sulphur contains both the $2p_{3/2}$ and $2p_{1/2}$ lines separated by ≈1.2 eV, reflecting the two sulphur states). Whilst characterizing the passive film was interesting in the course of this research, of greater importance was distinguishing between the oxidation states of copper in the film, as we needed to use this information

later in the analysis of the impedance data and this task was unsuccessful. However, after a comprehensive literature review, we found strong evidence that the oxidation state of copper in either Cu_2S or CuS is equal to 1 [44–46].

3.5. Electrochemical impedance spectroscopy

3.5.1. Validation of impedance data

Electrochemical impedance spectroscopy (EIS) plots for the passive copper were measured over a wide range of the frequency (5 kHz-0.01 Hz) as a function of the applied potential across the passive range, sulphide concentration and temperature in a deaerated 0.1 M *NaCl* solution. The impedances were measured after holding the potential constant for 48 hours (24 hours at 75°C) to assure that the passive film exists in the steady-state, as determined by the constancy of the current. A critical criterion during the EIS measurements is the stability of the system necessary to obtain viable data. In this study, the quality of the EIS data was checked both experimentally and theoretically. The data were checked experimentally by stepping the frequency from high-to-low and then immediately from low-to-high direction. The impedance response of the system under steady-state conditions should be identical in both directions. Figures 17 through 21 show selected results of stepping frequencies in both directions in the form of Nyquist and Bode plots. As can be seen, the measured impedance data match in the two-frequency step directions, demonstrating system stability at least over the time of data acquisition. The only case in which we observed small instability in the system, was the lower frequency part of the impedance collected in a solution containing the highest concentration of sulphide species (e.g. 2×10^{-3} M). As mentioned earlier, in this case, either the barrier layer or the outer layer that formed on the copper surface was very unstable with very poor adhesion to the metal surface. The black film spallation (perhaps cuprous sulphide) of the electrode surface was observed several times during the course of the experiments.

The quality of the measured impedance data was also checked using Kramers-Kronig transformations. It is important to note that the data satisfy the Kramers-Kronig transformations [47,48], demonstrating that the system complies with the constraints of linear systems theory (LST). The Kramers-Kronig transformations mathematically relate the real and imaginary parts of any complex function that describes the response of a physico-electrochemical system to an imposed perturbation and, therefore, the transformations are often used to investigate compliance of a system with the causality, stability, and linearity constraints of LST. The reader should note that these transformations do not reflect any physical property or condition of the system under study.

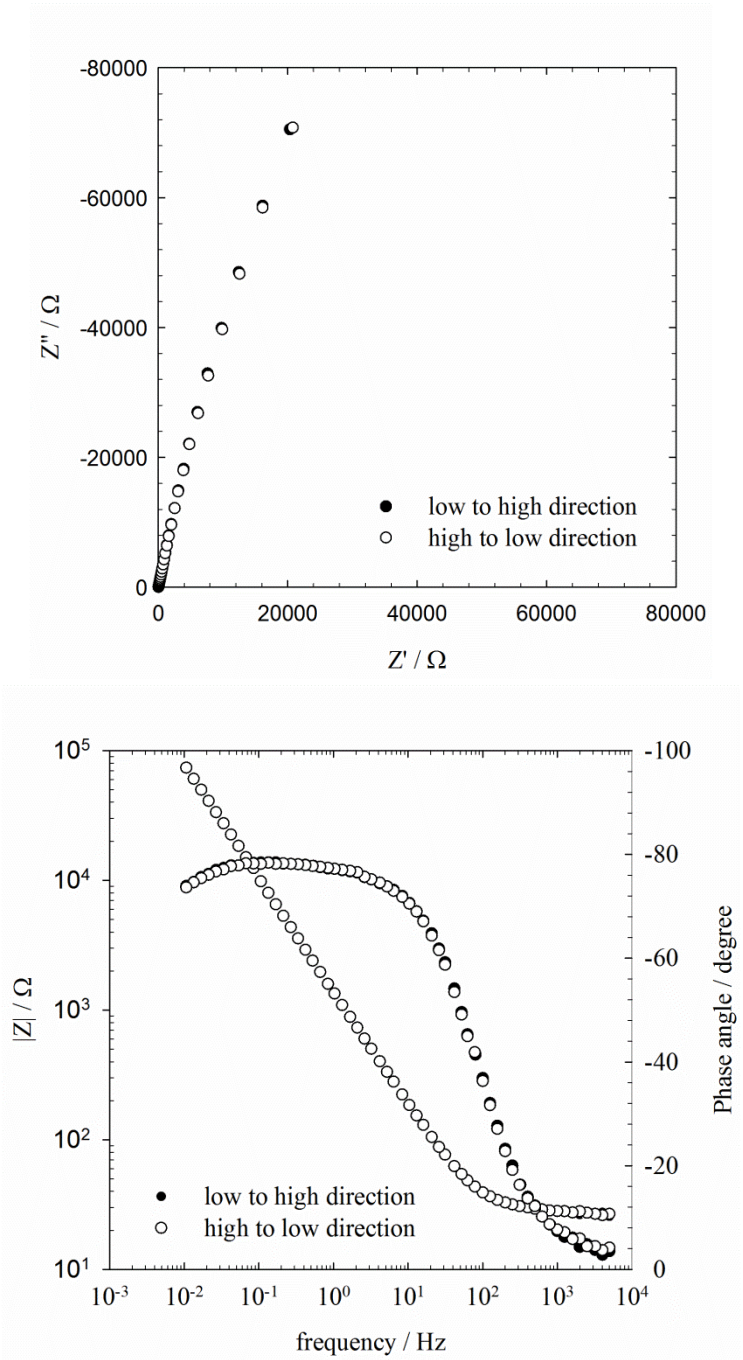

Figure 17. Comparison of the Nyquist (up) and Bode (down) plots for the passive copper formed at -0.295 V vs. SHE after polarization for 48h, and subsequent scanning the frequency in the high-to-low direction and immediately following in the low-to-high direction, in a deaerated 0.1 M, $NaCl$ + 2×10^{-4} M, $Na_2S.9H_2O$, at T=25°C.

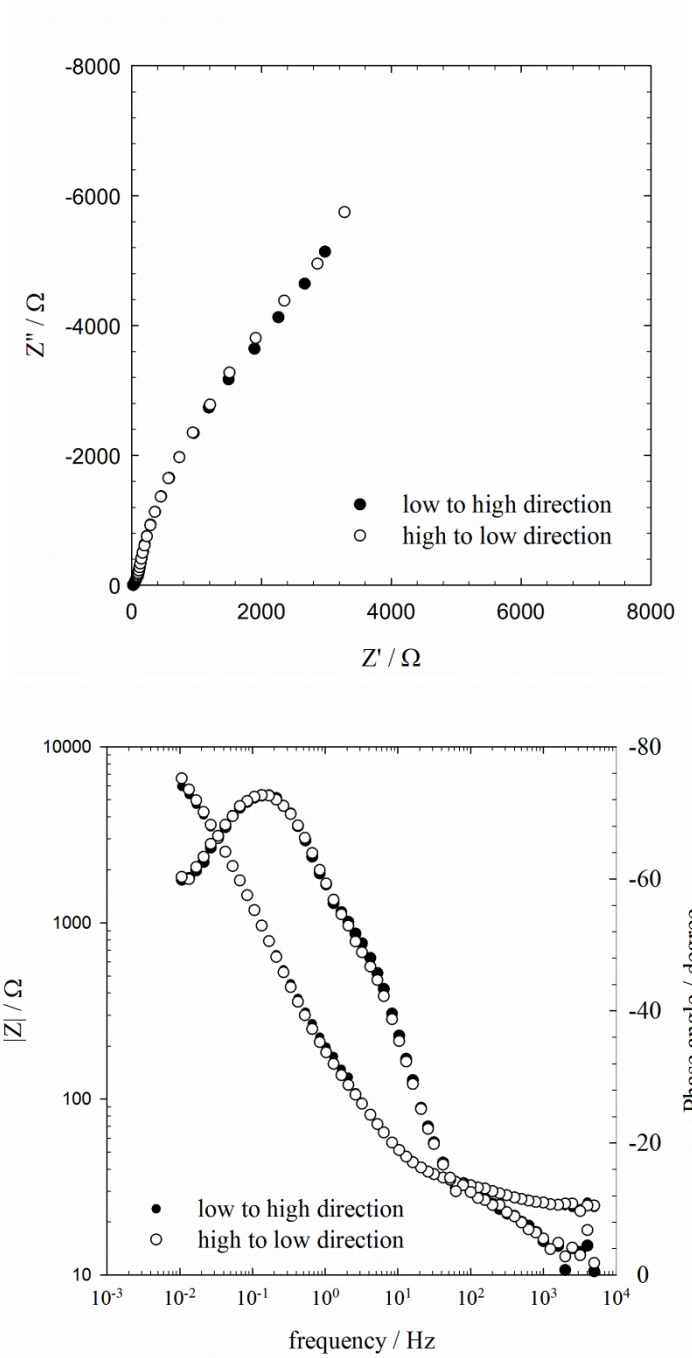

Figure 18. Comparison of the Nyquist (up) and Bode (down) plots for the passive copper formed at -0.195 V vs. SHE after polarization for 48h, and subsequent scanning the frequency in the high-to-low direction and immediately following in the low-to-high direction, in a deaerated 0.1 M, $NaCl$ + 4×10^{-4} M, $Na_2S.9H_2O$, at T=25°C.

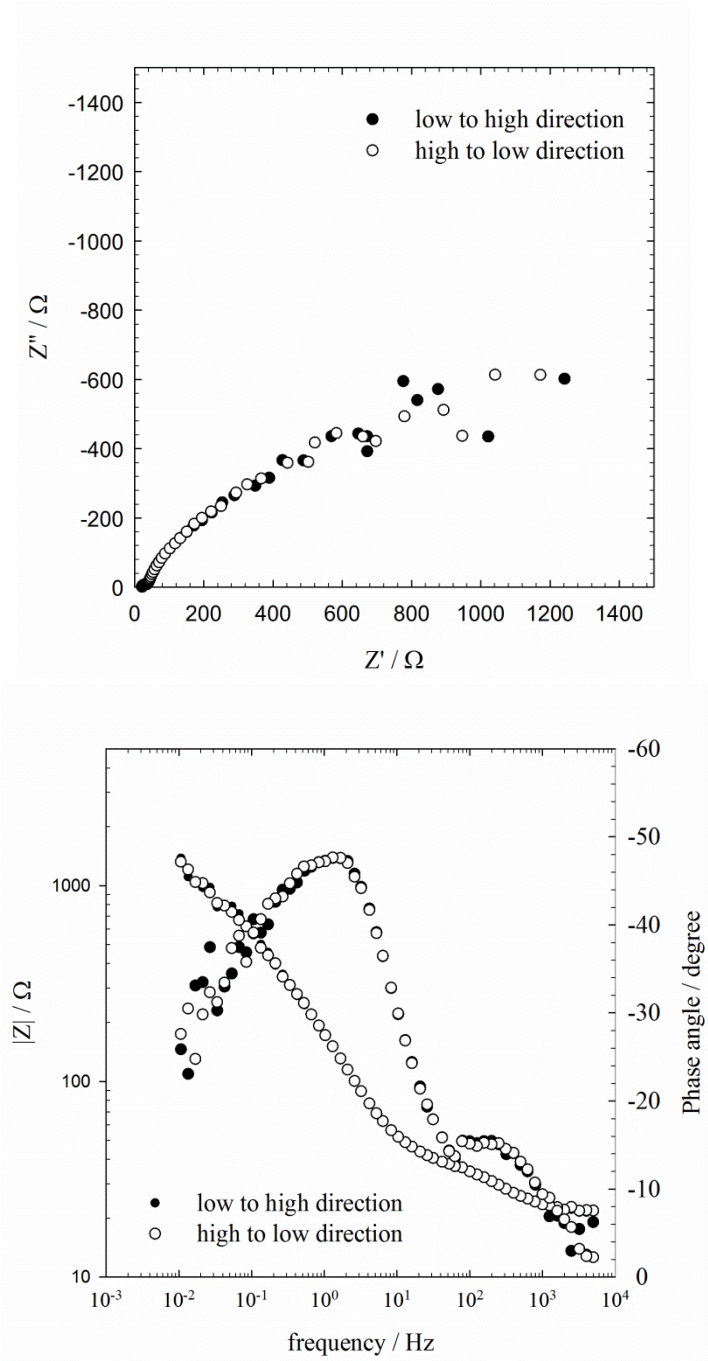

Figure 19. Comparison of the Nyquist (up) and Bode (down) plots for the passive copper formed at -0.395 V vs. SHE after polarization for 48h, and subsequent scanning the frequency in the high-to-low direction and immediately following in the low-to-high direction, in a deaerated 0.1 M, *NaCl* + 2×10^{-3} M, $Na_2S.9H_2O$, at T=25°C.

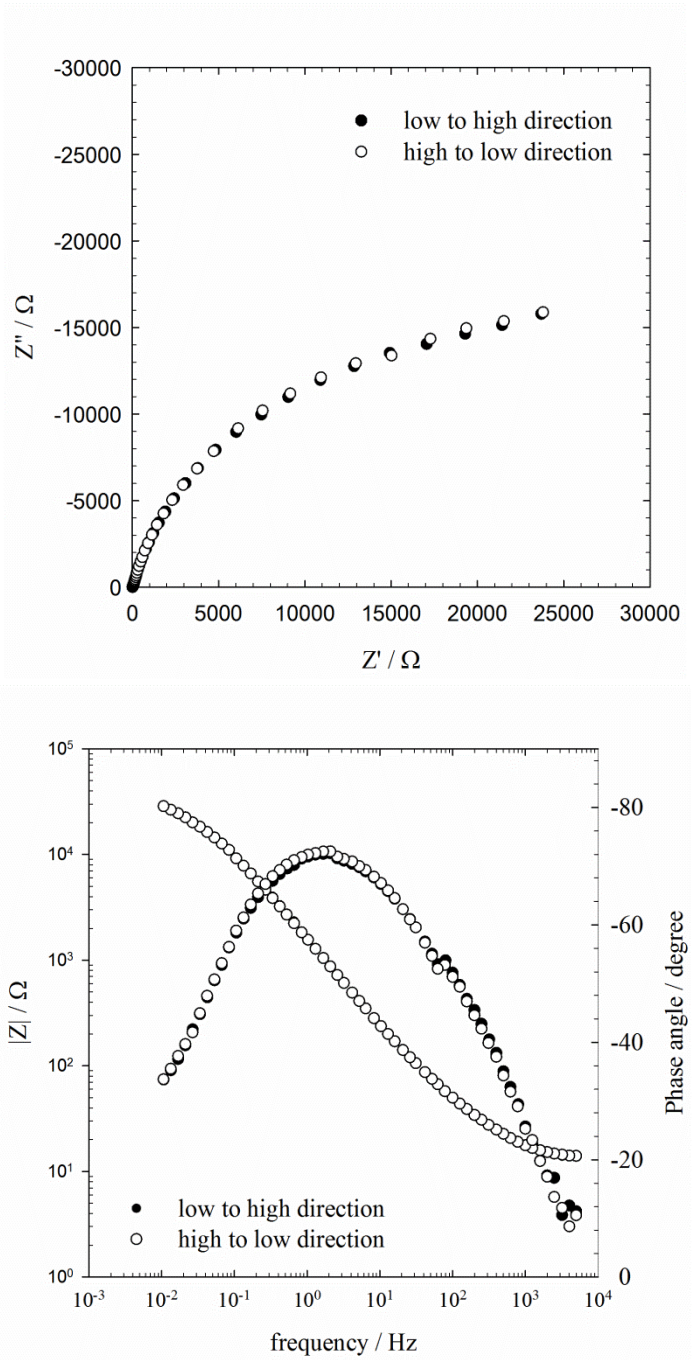

Figure 20. Comparison of the Nyquist (up) and Bode (down) plots for the passive copper formed at -0.295 V vs. SHE after polarization for 48h, and subsequent scanning the frequency in the high-to-low direction and immediately following in the low-to-high direction, in a deaerated 0.1 M, *NaCl* + 2×10^{-4} M, $Na_2S.9H_2O$, at T=50°C.

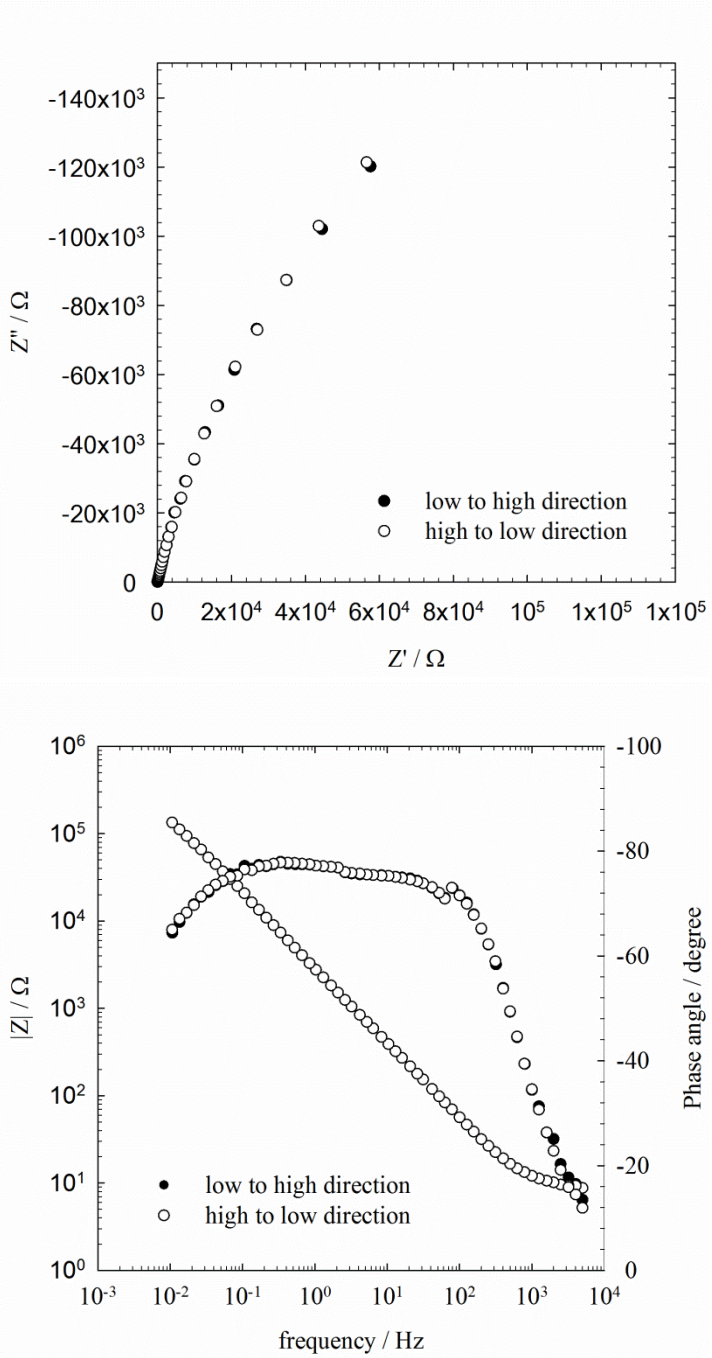

Figure 21. Comparison of the Nyquist (up) and Bode (down) plots for the passive copper formed at -0.295 V vs. SHE after polarization for 24h, and subsequent scanning the frequency in the high-to-low direction and immediately following in the low-to-high direction, in a deaerated 0.1M, *NaCl* + 4×10^{-4}M, $Na_2S.9H_2O$, at T=75°C.

Macdonald and Urquidi-Macdonald [49–51] developed methods for transforming the real part of the electrochemical impedance into an imaginary part and vice versa. Their studies revealed strong sensitivity of the K-K transformation to a violation of the stability and causality constraints. However, they are not especially sensitive to violation of the linearity condition. Figures 22 through 26 show a selected number of the K-K transformations, in which the transformed components of the impedance are compared with the corresponding measured components. Excellent agreement is

obtained over most of the frequency range, except for small discrepancies at lower frequencies of the samples exposed to the highest concentration of sulfide species (Figure 26). As mentioned earlier, the system at this concentration of sulphide species was very unstable. Accordingly, the impedance data that did not satisfy K-K transformation criteria have been disregarded in further analysis. The same level of agreement was observed for all the impedance data used in this study, which provides unequivocal evidence that the system satisfies the constraints of the LST.

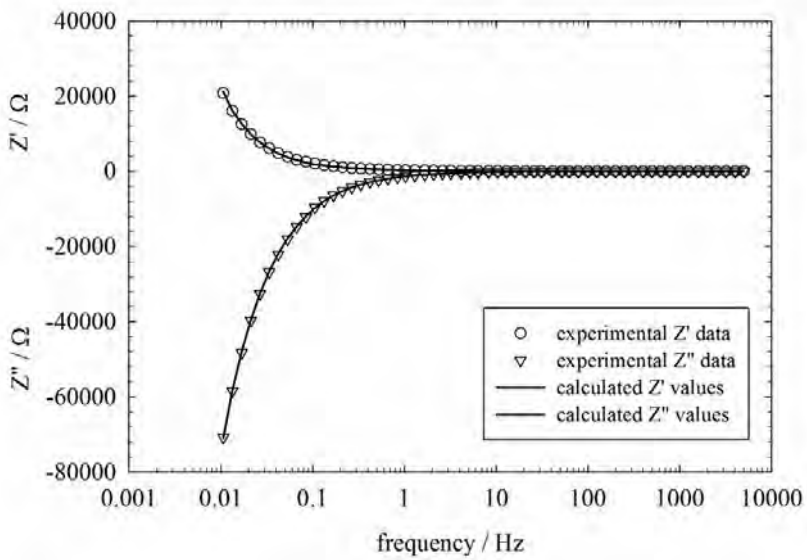

Figure 22. K-K transform of the EIS data for the passive copper formed at -0.295 V vs. SHE after polarization for 48h, in a deaerated 0.1 M, *NaCl* + 2×10^{-4} M, $Na_2S.9H_2O$, at T=25°C.

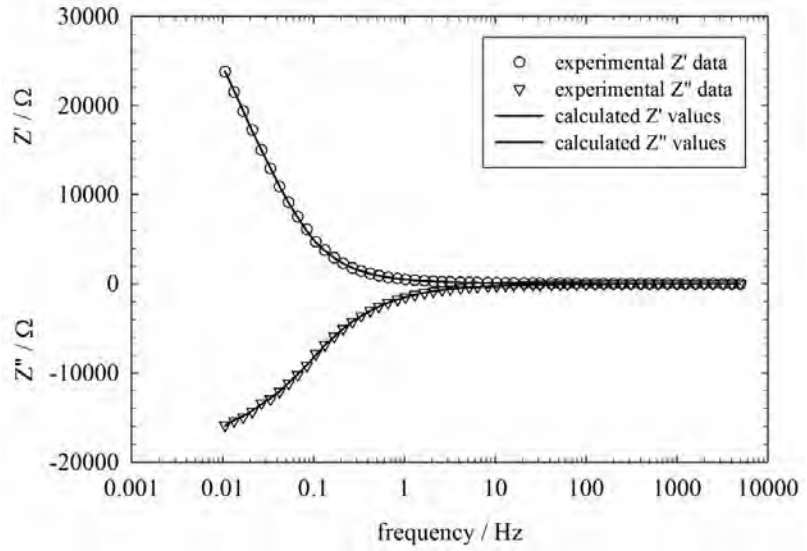

Figure 23. K-K transform of the EIS data for the passive copper formed at -0.295 V vs. SHE after polarization for 48h, in a deaerated 0.1 M, *NaCl* + 2×10^{-4} M, $Na_2S.9H_2O$, at T=50°C.

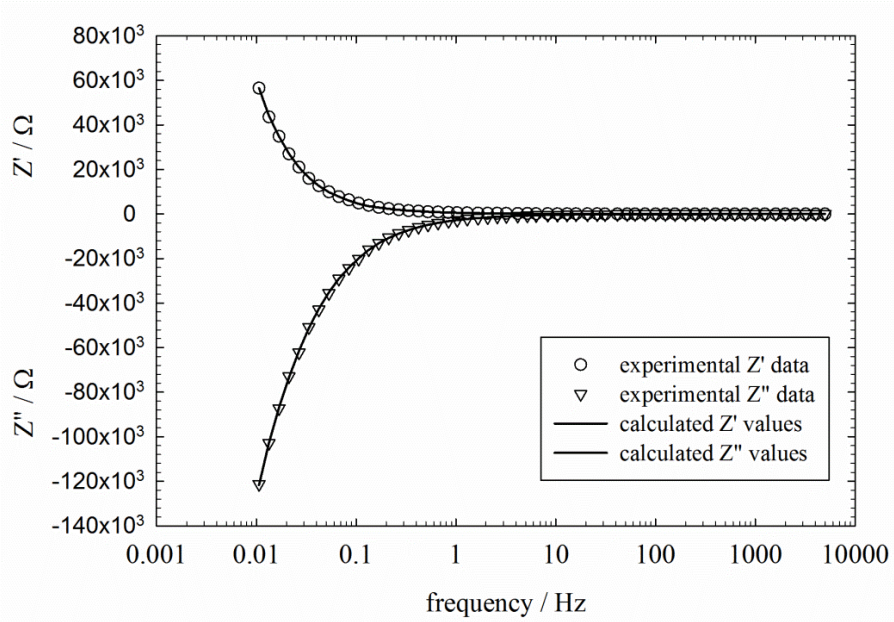

Figure 24. K-K transform of the EIS data for the passive copper formed at -0.295 V vs. SHE after polarization for 24h, in a deaerated 0.1 M, *NaCl* + 2×10^{-4} M, $Na_2S.9H_2O$, at T=75°C.

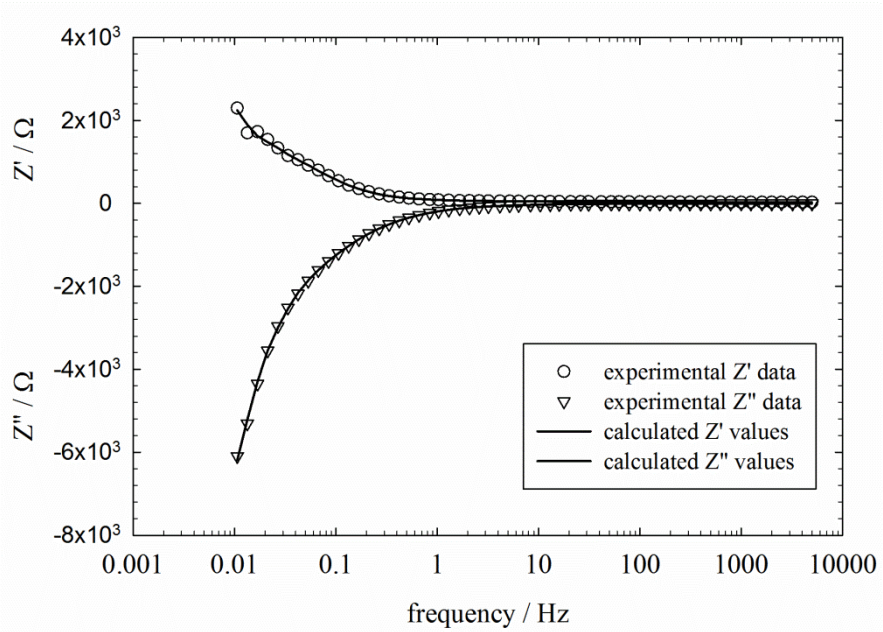

Figure 25. K-K transform of the EIS data for the passive copper formed at -0.295 V vs. SHE after polarization for 48h, in a deaerated 0.1 M, *NaCl* + 4×10^{-4} M, $Na_2S.9H_2O$, at T=25°C.

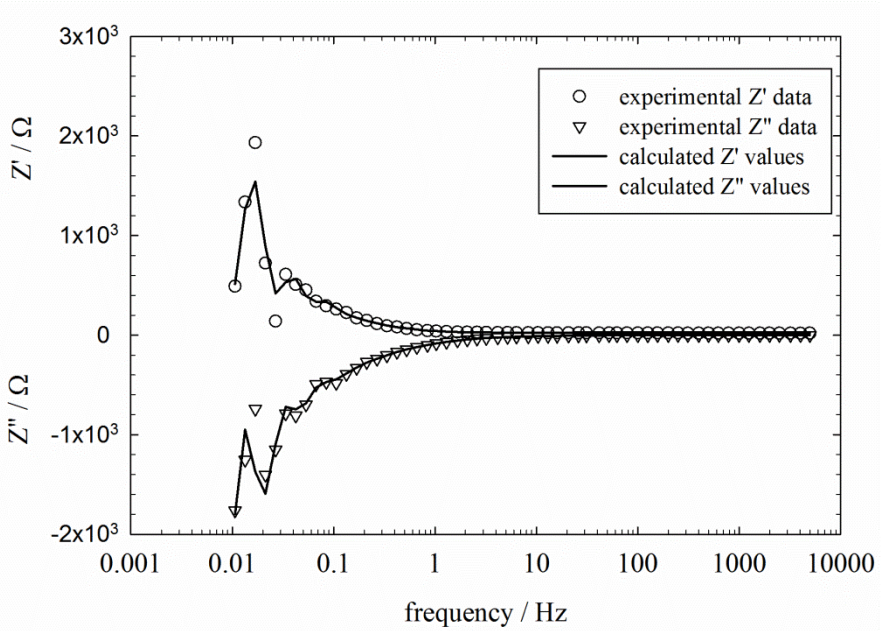

Figure 26. K-K transform of the EIS data for the passive copper formed at -0.295 V vs. SHE after polarization for 48h, in a deaerated 0.1 M, *NaCl* + 2×10^{-3} M, $Na_2S.9H_2O$, at T=25°C.

3.5.2. Effect of Formation Potential

The impedance spectra of the passive copper in a deaerated 0.1 M *NaCl* solution containing different concentrations of $Na_2S.9H_2O$ at 25°C, 50°C, and 75°C are shown in Figures 27 through 31 as a function of applied potential within the passive region ($-0.495 \leq E_{app.} \leq -0.195$ V *vs.* SHE). As can be seen, the impedance spectra of the system follow the same pattern having almost the same magnitude for most of the conditions except at 50°C and for the solution containing the highest concentration of sulphide species (e.g. 2×10^{-3} M) in which the observed response of the system shows potential dependencies. Similar behavior has been reported previously for the passive oxide film on *Ni* [52], and it corresponded to the transport of defects across the passive film. As stated in the PDM hypothesis, transport of point defects is principally under the influence of the electric field across the barrier layer, and since the field strength is postulated [35] to be independent of the applied potential, the impedance should be insensitive to the film formation potential, as observed here and reported previously [52]. At sulphide concentration of 2×10^{-3} M (Figure 31), however, we observed potential dependency of the system, especially at E=-0.395 V *vs.* SHE. The form of impedance corresponds to the occurrence of a charge transfer reaction in a porous film of finite thickness. The precipitated outer layer seems to play the most important role in the impedance behavior of the system at this condition and, since it is very unstable and perhaps porous, its response changes drastically with the applied potential.

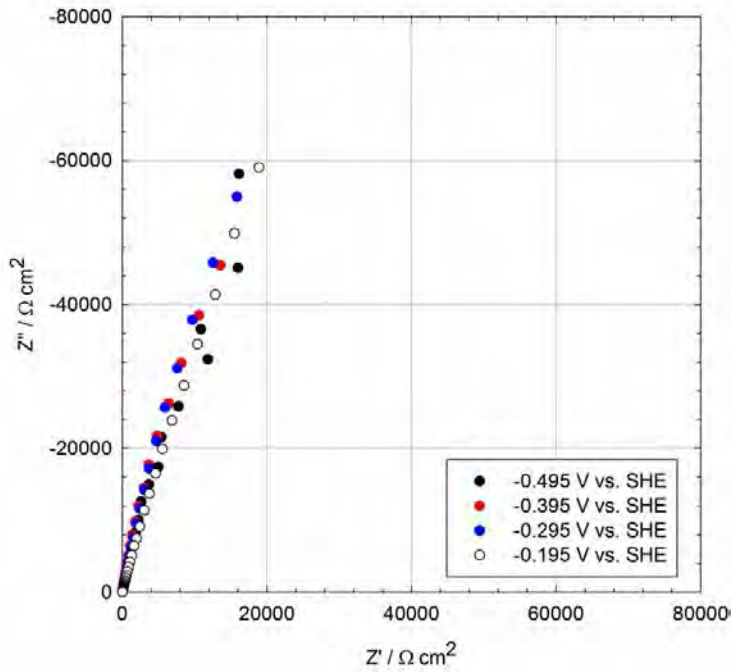

Figure 27. Nyquist plots for the passive copper in a deaerated 0.1 M, *NaCl* + 2×10^{-4} M, $Na_2S.9H_2O$, at T=25°C as a function of applied potentials.

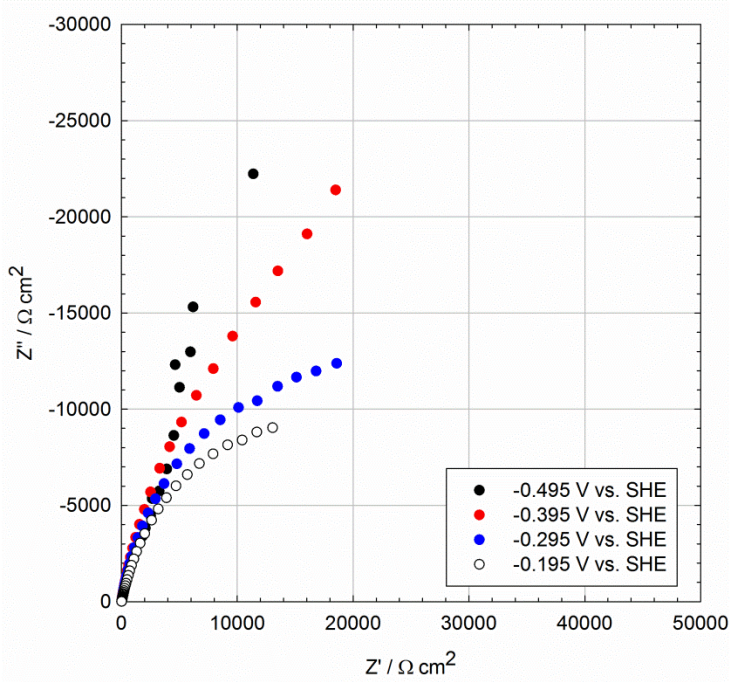

Figure 28. Nyquist plots for the passive copper in a deaerated 0.1 M, *NaCl* + 2×10^{-4} M, $Na_2S.9H_2O$, at T=50°C as a function of applied potentials.

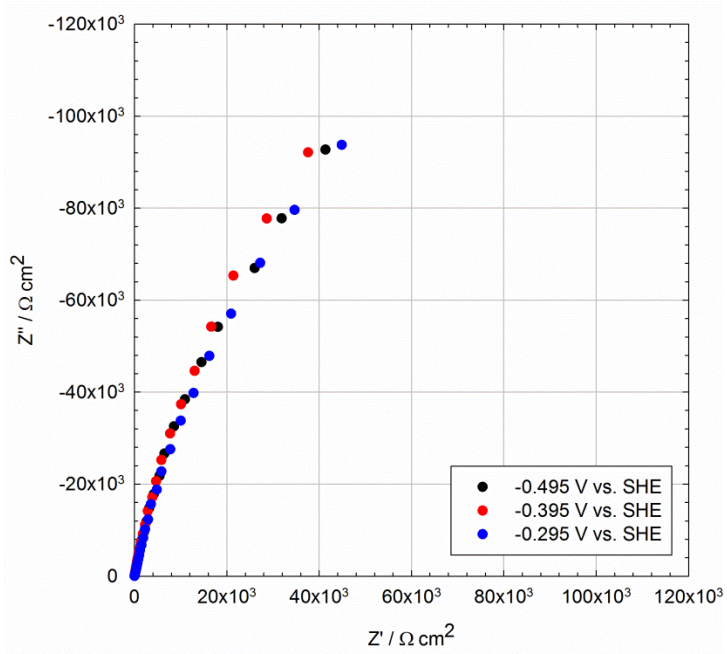

Figure 29. Nyquist plots for the passive copper in a deaerated 0.1 M, *NaCl* + 2×10^{-4} M, $Na_2S.9H_2O$, at T=75°C as a function of applied potentials.

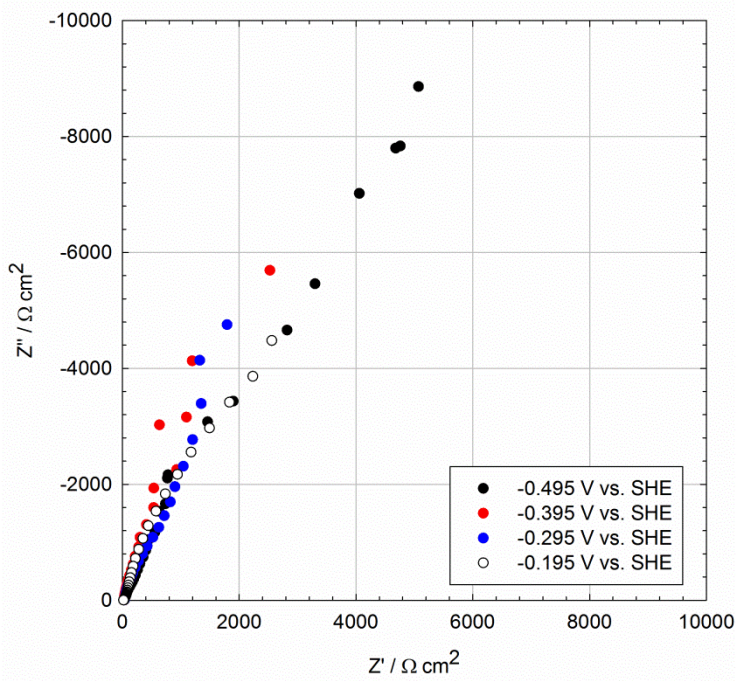

Figure 30. Nyquist plots for the passive copper in a deaerated 0.1 M, *NaCl* + 4×10^{-4} M, $Na_2S.9H_2O$, at T=25°C as a function of applied potentials.

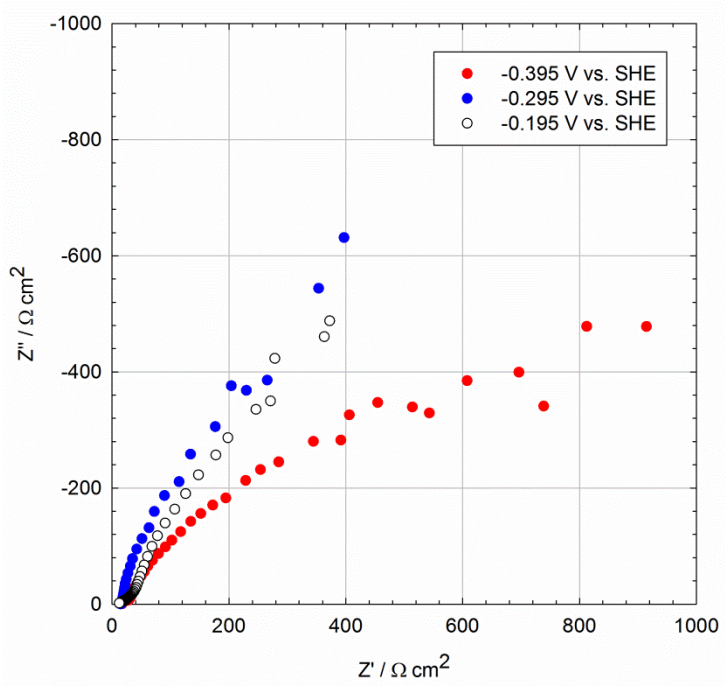

Figure 31. Nyquist plots for the passive copper in a deaerated 0.1 M, *NaCl* + 2×10^{-3} M, $Na_2S.9H_2O$, at T=25°C as a function of applied potentials.

3.5.3. Effect of temperature

Figures 32 and 33 display the effect of solution temperature on the impedance response (in the form of Bode plots) of the passive films formed on copper at -0.495 and -0.295 V *vs.* SHE in a deaerated 0.1 M *NaCl* + 2×10^{-4} M $Na_2S.9H_2O$ solution. The effect of temperature can be divided into two parts of the impedance spectra: (1) high frequency part (5000 > f >100 Hz) and (2) medium to low frequency part (100 < f < 0.01 Hz). As we know, in the high-frequency region, solution resistance is the dominating factor in the impedance response of the system and the phase angle is almost zero. At frequencies in the range of 5000 Hz-100 Hz, the impedance of the system is determined by the capacitance of the passive film since its impedance is lower in this frequency range. On the other hand, the medium frequency part of the impedance is mostly controlled by interfacial charge transfer reactions as well as relaxation in the space charge layer, while the lower frequency region is mostly dominated by transport of the point defects through the barrier layer. One can see that at 25°C and 75°C, the phase angle shows constant behavior at this frequency range, which is typical behavior for the passive films and attributed to the migration of the point defects through the film under the influence of the electric field. At 50°C, we see an abrupt change in the lower frequency part, which could be attributed to the diffusion of species in solution or any other form of the interfacial reactions. Interestingly, at higher temperature, i.e. 75°C, we did not observe such an abrupt change in the phase angle, which means perhaps that diffusion at higher temperature is not a controlling factor. Another point to notice is a decrease in the slope of the logarithm of the impedance modulus against the logarithm of the frequency from about -0.87 to -0.79 as a result of an increase in temperature from 25°C to 50°C. Generally, having a slope of less than -1 is attributed to the presence of porosity on the electrode surface with semi-infinite pore length [23]. Therefore, we can conclude that one impact of the temperature rise, up to 50°C, could be an increase in the porosity and/or dissolution of the sulphide passive film (barrier or outer layers)

while an increase in temperature did not result in the same behavior and even had a reverse impact.

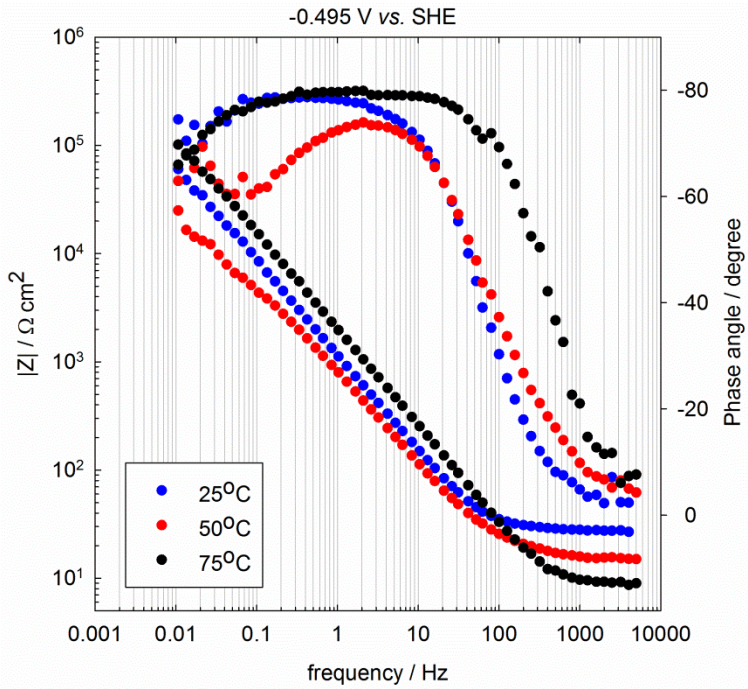

Figure 32. Bode plots for the passive copper formed at -0.495 V vs. SHE in a deaerated 0.1 M *NaCl* + 2×10^{-4} M $Na_2S.9H_2O$, as a function of temperature.

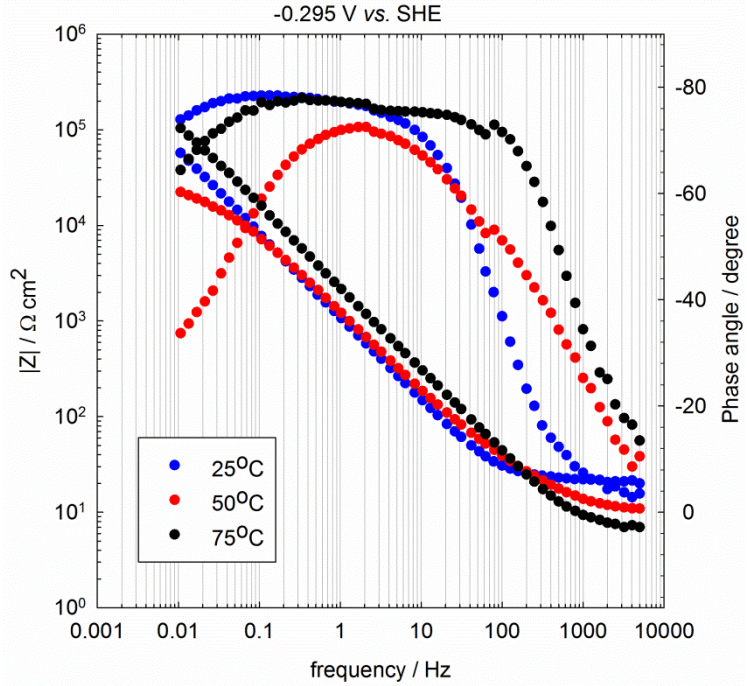

Figure 33. Bode plots for the passive copper formed at -0.295 V vs. SHE in a deaerated 0.1 M *NaCl* + 2×10^{-4} M $Na_2S.9H_2O$, as a function of temperature.

3.5.4. Effect of sulphide concentration

The impedance responses for the passive copper in deaerated sodium chloride solutions containing various sulphide concentrations are plotted in Figures 34 and 35 in

the form of Bode plots. One can see that the addition of sulphide to sodium chloride solution has a profound effect on the impedance response of the system and alters its behavior drastically. While the system shows the typical response attributed to the passive films at lower sulphide concentrations (i.e. 2×10^{-4} M), deconvolution of the phase angle *vs.* frequency indicated the presence of at least two time constants as well as a diffusion element for the higher sulphide concentrations. In accordance with previous studies on the passive films, the time constant in the higher frequency part could be attributed to the electronic properties of the passive film, while the time constants in the medium to low frequency part are associated with the charge transfer process at the film/solution interface and the defect transport across the passive film, respectively. Another effect of the sulphide concentration is on the magnitude of the impedance and its phase angle. One can see that, as a result of an increase in sulphide ion concentration, the impedance modulus decreases drastically (about two orders of magnitude). If we consider the magnitude of the impedance as an estimate of the polarization resistance of the film, this major decrease indicates that the charge transfer reaction becomes faster and accordingly the corrosion rate of copper will be higher at higher concentrations of the sulphide species. One can also see that the phase angle response of the system shows a displacement towards the lower frequency part, indicating that the response of the passive film is disappearing and the interfacial reactions will probably start to dominate the impedance response of the system. Observation of a phase angle around 45° as a result of a rise in the sulphide concentration could suggest that the electrochemical current at this concentration level becomes more transport-controlled. The reader should notice that the system response at the higher concentration of sulphide species was very potential dependent, as stated before.

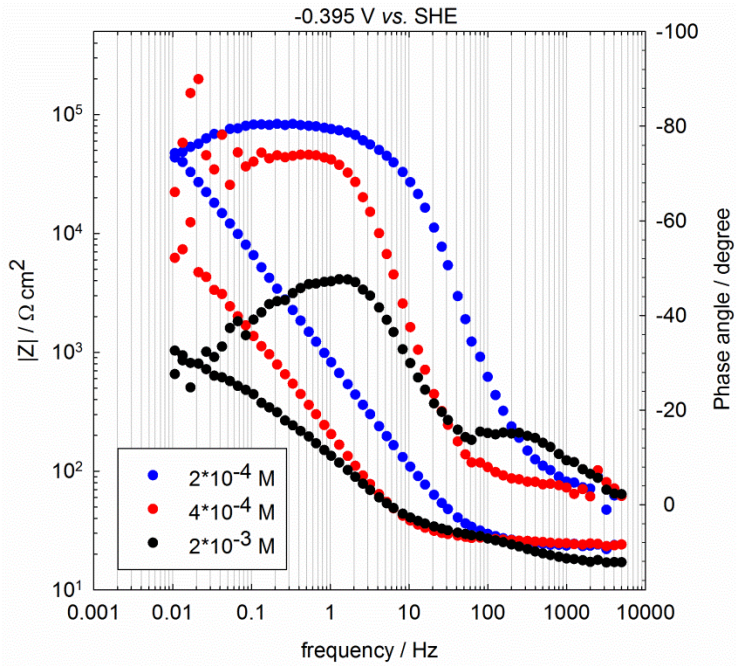

Figure 34. Bode plots for the passive copper formed at -0.395 V vs. SHE at 25°C as a function of sulphide concentration.

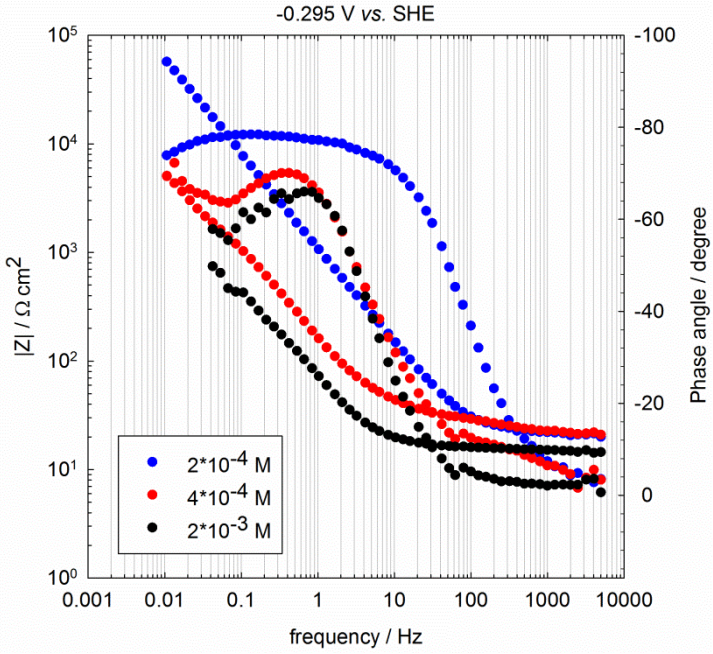

Figure 35. Bode plots for the passive copper formed at -0.295 V vs. SHE at 25°C as a function of sulphide concentration.

3.6. Impedance model: Point Defect Model

A modified point defect model for the formation of the bi-layer *Cu*/Cu_2S/*CuS* passive films on copper in the sulphide containing solutions is proposed. The Point Defect Model was developed by Macdonald and co-workers as a mechanistically-based model that could be tested analytically against experiment, and which might be used as the basis of a deterministic protocol for predicting the accumulation of corrosion damage in practical systems [53–55]. The PDM is now highly developed and has accounted for all of the known phenomena associated with the passive state. To our knowledge, there are no known conflicts with experiment, where confluence between theory and experiment has been first demonstrated, and, indeed, the model has predicted new phenomena that have subsequently been observed, including the photo-inhibition of passivity breakdown (PIPB) [35,56–58] and resistive depassivation [59], and has provided a theoretical basis for designing new alloys from first principles [40, 41]. The PDM has been previously used to interpret electrochemical impedance data by optimizing the model on the experimentally-determined real and imaginary components of the interphasial (metal/passive film/solution) impedance, with considerable success [62–65]. An earlier version of the model has been extensively used to analyze data in different practical systems. This earlier model assumed that the impedance due to the transport of point defects in the barrier layer was separable from the impedance due to the point defect generation/annihilation reactions occurring at the barrier layer interfaces [66,67]. In all the previous system, this model proposed for the formation and dissolution of the passive oxide films on different metals and in this study for the first time we proposed a model for the growth and dissolution of the passive sulphide films.

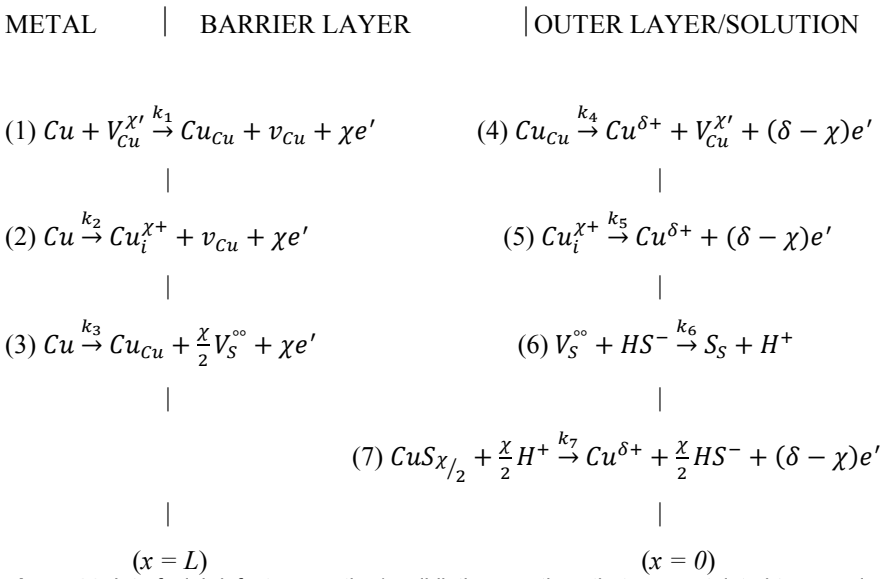

Figure 36. Interfacial defect generation/annihilation reactions that are postulated to occur in the growth of anodic barrier sulphide films according to the Point Defect Model. $\boldsymbol{V_{Cu}^{\chi'}}$ ≡ cation vacancy on the metal sublattice of the barrier layer, $\boldsymbol{Cu_i^{\chi+}}$ ≡ cuprous cation interstitial, $\boldsymbol{Cu_{Cu}}$ ≡ cuprous cation in cation site on the metal sublattice of the Cu_2S barrier layer, $\boldsymbol{V_S^{\circ\circ}}$ ≡ sulphur vacancy on the anion sublattice of the barrier layer, $\boldsymbol{S_S}$ ≡ sulphur anion on the anion sublattice of the barrier layer, $\boldsymbol{Cu^{\delta+}}$ ≡ cuprous cation in solution. $\boldsymbol{\chi}$ is oxidation state of the cation in the barrier Cu_2S barrier layer and $\boldsymbol{\delta}$ is the oxidation state of the cation in the solution.

The PDM postulates that the passive film that forms on a metal surface comprises a bi-layer structure, consisting of a point defective barrier layer that grows directly into the metal, and an outer layer that forms by hydrolysis and precipitation of cations that are transmitted through the barrier layer and are ejected at the barrier layer/outer layer (bl/ol) interface, and by the dissolution of the barrier layer at the same location. The point defects that are considered in the model are cation and anion vacancies and cation interstitials.

The physico-chemical basis of the PDM is shown in Figure 36. Briefly, the model postulates that defect generation and annihilation reactions occur at the metal/barrier layer (m/bl) and the barrier layer/outer layer (bl/ol) interfaces and that these reactions essentially establish the point defect concentrations within the barrier layer. It is postulated that there is a net flow of anion vacancies from m/bl interface (at x=L) under anodic polarization to the bl/ol interface (at x=0) and a net flow of cation vacancies in the reverse direction. Understanding of the growth of the barrier layer requires differentiating of the interfacial reactions to whether they are lattice conservative or nonconservative processes. Accordingly, Reactions (1), (2), (4), (5) and (6) in Figure 36 are lattice conservative, meaning that their occurrence does not result in the movement of the boundary while, Reactions (3) and (7) result in generation and destroy of the barrier layer, respectively, so they are considered as being lattice nonconservative reactions with regard to the laboratory frame of reference [35]. Analytical expressions for the rate constants for the reactions in Figure 36, as derived by the method of partial charges, are summarized in Tables 2 and 3.

Table 2. Coefficients for the rate constants for the reactions that generate and annihilate point defects at the m/bl interface [Reactions (1) – (3)] and at the bl/s interface [Reactions (4) – (6)], Figure 36, and for dissolution of the film (Reaction 7) [53–55]. $\boldsymbol{k_i = k_i^0 e^{a_i V} e^{b_i L}}$

Reaction	$a_i(V^{-1})$	$b_i(cm^{-1})$	Units of k_i^0
(1) $Cu + V_{Cu}^{\chi'} \overset{k_1}{\rightarrow} Cu_{Cu} + v_{Cu} + \chi e'$	$\alpha_1(1-\alpha)\chi\gamma$	$-\alpha_1\chi K$	$\frac{1}{s}$
(2) $Cu \overset{k_2}{\rightarrow} Cu_i^{\chi+} + v_{Cu} + \chi e'$	$\alpha_2(1-\alpha)\chi\gamma$	$-\alpha_2\chi K$	$\frac{mol}{cm^2 s}$
(3) $Cu \overset{k_3}{\rightarrow} Cu_{Cu} + \frac{\chi}{2}V_{\ddot{S}} + \chi e'$	$\alpha_3(1-\alpha)\chi\gamma$	$-\alpha_3\chi K$	$\frac{mol}{cm^2 s}$
(4) $Cu_{Cu} \overset{k_4}{\rightarrow} Cu_i^{\delta+} + V_{Cu}^{\chi'} + (\delta-\chi)e'$	$\alpha_4\alpha\delta\gamma$		$\frac{mol}{cm^2 s}$
(5) $Cu_i^{\chi+} \overset{k_5}{\rightarrow} Cu^{\delta+} + (\delta-\chi)e'$	$\alpha_5\alpha\delta\gamma$		$\frac{cm}{s}$
(6) $V_{\ddot{S}} + HS^- \overset{k_6}{\rightarrow} S_S + H^+$	$2\alpha_6\alpha\gamma$		$\frac{cm}{s}$
(7) $CuS_{\chi/2} + \chi H^+ \overset{k_5}{\rightarrow} Cu^{\delta+} + \frac{\chi}{2}HS^- + H^+ + (\delta-\chi)e'$	$\alpha_7\alpha(\delta-\chi)\gamma$		$\frac{mol}{cm^2 s}$

The electron current density, I, which is sensed in an external circuit, is given by:

$$I = F\left\{\chi k_1 C_v^L + \chi k_2 + \chi k_3 + (\delta-\chi)k_4 + (\delta-\chi)k_5 C_i^0 + (\delta-\chi)k_7\left(\frac{C_{H^+}}{C_{H^+}^0}\right)^n\right\} \quad (8)$$

where C_v^L is the concentration of cation vacancies at the m/bl interface, C_i^0 is the concentration of cation interstitials at the bl/ol interface, F is the Faraday's constant and "n" is dissolution reaction order with regard to the hydrogen ion concentration. Note that Eq. (8) does not depend upon the concentration of anion vacancies or upon the rate constant for Reaction (6), Figure 36. Thus, no relaxations in the impedance response involve anion vacancies, but this is essentially an artifact of considering Reaction (3), Figure 36, to be irreversible. If this reaction was considered to be reversible, then a relaxation involving anion vacancies would be present.

Table 3. Definition of the standard rate constants for the interfacial defect generation and annihilation reactions employed in the point defect model [64]

Reaction	k_i^0
(1) $Cu + V_{Cu}^{\chi'} \overset{k_1}{\rightarrow} Cu_{Cu} + v_{Cu} + \chi e'$	$k_1^{00}\exp(-\chi\alpha_1\gamma(\phi_{f/s}^0 + \beta pH))$
(2) $Cu \overset{k_2}{\rightarrow} Cu_i^{\chi+} + v_{Cu} + \chi e'$	$k_2^{00}\exp(-\chi\alpha_2\gamma(\phi_{f/s}^0 + \beta pH))$
(3) $Cu \overset{k_3}{\rightarrow} Cu_{CU} + \frac{\chi}{2}V_{\ddot{S}} + \chi e'$	$k_3^{00}\exp(-\chi\alpha_3\gamma(\phi_{f/s}^0 + \beta pH))$
(4) $Cu_{Cu} \overset{k_4}{\rightarrow} Cu_i^{\delta+} + V_{Cu}^{\chi'} + (\delta-\chi)e'$	$k_4^{00}\exp(\delta\alpha_4\gamma(\phi_{f/s}^0 + \beta pH))$
(5) $Cu_i^{\chi+} \overset{k_5}{\rightarrow} Cu^{\delta+} + (\delta-\chi)e'$	$k_5^{00}\exp(\delta\alpha_5\gamma(\phi_{f/s}^0 + \beta pH))$
(6) $V_{\ddot{S}} + HS^- \overset{k_6}{\rightarrow} S_S + H^+$	$k_6^{00}\exp(2\alpha_6\gamma(\phi_{f/s}^0 + \beta pH))$
(7) $CuS_{\chi/2} + \chi H^+ \overset{k_5}{\rightarrow} Cu^{\delta+} + \frac{\chi}{2}HS^- + H^+ + (\delta-\chi)e'$	$k_7^{00}\exp((\delta-\chi)\alpha_7\gamma(\phi_{f/s}^0 + \beta pH))$

Using the method of partial charges, the rate constants for the reactions are found to be of the form:

$$k_i = k_i^0 exp[a_i(V - R_{ol}I) - b_i L + c_i pH] \qquad \text{i=1, 2, 3} \qquad (9)$$

$$k_j = k_j^0 exp\left[a_j(V - R_{ol}I) + c_j pH\right] \qquad \text{j=4, 5, 6, 7} \qquad (10)$$

In deriving these expressions theoretically, it is assumed that a resistive outer layer, R_{ol}, exists on the surface of the barrier layer and that the passive current flows through the barrier layer to a remote cathode, which is the normal experimental configuration. As a result, the potential that exists at the bl/ol interface must be corrected from that applied at the reference electrode located at the outer layer/solution interface by the potential drop across the outer layer, where R_{ol} (Ω cm^2) is the specific resistance of the outer layer.

Let us assume that the applied potential changes sinusoidally around some mean value ($\bar{V}$) in accordance with Eq. (11):

$$V = \bar{V} + \delta V = \bar{V} + \Delta V e^{j\omega t} \qquad (11)$$

where ω is the angular frequency and ΔV is the voltage amplitude. The bar over a letter refers to the corresponding value under the steady-state conditions.
Calculation of the faradaic admittance (Y_F), which is defined as follows, is the main task here:

$$Y_F = \frac{1}{Z_F} = \frac{\delta I}{\delta V} = \frac{\Delta I}{\Delta V} \qquad (12)$$

where Z_F is the faradaic impedance. Note that, I, is a function of the potential at the bl/ol interface (U), but the potential that is modulated is that at the outer layer/solution (ol/s) interface (V), or close to it, depending upon the exact placement of the tip of the Luggin probe. The two potentials are related by

$$U = V - R_{ol}I \qquad (13)$$

Accordingly,

$$Y_F = \left(\frac{dI}{dV}\right)_{V=\bar{V}} = \left(\frac{dI}{dU}\right)_{U=\bar{U}}\left(\frac{dU}{dV}\right)_{V=\bar{V}} = \left(\frac{dI}{dU}\right)_{U=\bar{U}}\left(1 - R_{ol}\left(\frac{dI}{dV}\right)_{V=\bar{V}}\right) \qquad (14)$$

Eq. (14) may be rearranged to

$$\frac{1}{Y_F} = \frac{1}{Y_F^0} + \frac{1}{R_{ol}} \;\; or \; Y_F = \frac{Y_F^0}{1+R_{ol}Y_F^0} \qquad (15)$$

where $Y_F^0 = \left(\frac{dI}{dU}\right)_{U=\bar{U}}$ is the admittance calculated in the absence of the outer layer, assuming that the potential at the bl/ol interface is $\bar{U}$ under the steady-state conditions. It is evident that $Y_F \to Y_F^0$ as $R_{ol} \to 0$ and $Y_F \to \frac{1}{R_{ol}}$ for $Y_F^0 \to \infty$ which means that the interphasial impedance becomes controlled by the outer layer in the limit of an infinitely large outer layer specific resistance.

The values of $\bar{U}$ and other steady-state values can be easily calculated. Assuming some arbitrary value of $\bar{U}$, we can immediately calculate $\bar{k}_i$, i = 1-7 from Eqs. (9) and (10). The rate of change of the barrier layer thickness for a layer that forms irreversibly on a metal surface can be expressed as

$$\frac{dL}{dt} = \frac{dL^+}{dt} - \frac{dL^-}{dt} = \Omega k_3^0 e^{a_3 V} e^{b_3 L} e^{c_3 pH} - \Omega k_7^0 e^{a_7 V} e^{c_3 pH}\left(\frac{C_{H^+}}{C_{H^+}^0}\right)^n \qquad (16)$$

By setting the left side of Eq. (16) equal to zero, the steady-state thickness of the barrier layer, L_{ss}, is readily derived as (for the system in which $\chi = \delta$)

$$L_{ss} = \left[\frac{1-\alpha}{\varepsilon}\right] V + \left[\frac{2.303n}{\alpha_3 \varepsilon \chi \gamma} - \frac{\beta}{\varepsilon}\right] pH + \frac{1}{\alpha_3 \varepsilon \chi \gamma} ln\left(\frac{k_3^0}{k_7^0}\right) \quad (17)$$

The values of the steady-state concentrations $\bar{C}_i^0$, $\bar{C}_v^L$ and $\bar{C}_O^0$ (concentrations of metal vacancies and interstitials at the bl/ol interface and anion vacancies at bl/ol interface) can be found by equating the rates at each location to yield

$$\bar{C}_v^L = \frac{\bar{k}_4}{\bar{k}_1} \quad (18)$$

$$\bar{C}_i^0 = \frac{\bar{k}_2}{\bar{k}_5} \quad (19)$$

and

$$\bar{C}_O^0 = \frac{\bar{k}_3}{\bar{k}_6} \quad (20)$$

Eqs. (18) to (20) follows from the conditions that steady-state fluxes of cation vacancies, cation interstitials, and anion vacancies, respectively, are constants (do not depend upon position inside the barrier layer).

Finally, we calculate the values of steady-state current density and potential as

$$\bar{I} = F\left\{\chi \bar{k}_1 \bar{C}_v^L + \chi \bar{k}_2 + \chi \bar{k}_3 + (\delta - \chi)\bar{k}_4 + (\delta - \chi)\bar{k}_5 \bar{C}_i^0 + (\delta - \chi)\bar{k}_7 \left(\frac{C_{H^+}}{C_{H^+}^0}\right)^n\right\} \quad (21)$$

and

$$\bar{V} = \bar{U} + R_{ol}\bar{I} \quad (22)$$

Obviously, if we have a code for calculating the admittance of the system in the absence of the outer layer, Y_F^0, we can calculate the admittance in the presence of the outer layer, Y_F, by using Eq. (12), assuming that Y_F^0 is calculated at the steady-state applied potential that equals $\bar{U}$ (but not $\bar{V}$).

3.6.1. Calculation of Y_F^0

As follows from Eq. (8) we have in the linear form:

$$Y_F^0 = \frac{\delta I}{\delta U} = \frac{\Delta I}{\Delta U} = I_U + I_L \frac{\Delta L}{\Delta U} + I_v^L \frac{\Delta C_v^L}{\Delta U} + I_i^0 \frac{\Delta C_i^0}{\Delta U} \quad (23)$$

Where

$$I_U = F\left[\chi a_1 \bar{k}_1 \bar{C}_v^L + \chi \bar{k}_2 a_2 + \chi \bar{k}_3 a_3 + (\delta - \chi)\bar{k}_4 a_4 + (\delta - \chi)\bar{k}_5 a_5 \bar{C}_i^0 + (\delta - \chi)\bar{k}_7 a_7\right] \quad (24)$$

$$I_L = F\left[\chi b_1 \bar{k}_1 \bar{C}_v^L + \chi \bar{k}_2 b_2 + \chi \bar{k}_3 b_3\right] \quad (25)$$

$$I_v^L = F\chi \bar{k}_1 \quad (26)$$

$$I_i^0 = F(\delta - \chi)\bar{k}_5 \quad (27)$$

Here, it is assumed that $U = \bar{U} + \delta U = \bar{U} + \Delta U e^{j\omega t}$ and we identify the four terms on the right side as arising from relaxations with respect to the applied potential V, the thickness of the barrier layer with respect to the voltage at the bl/ol interface, U, cation vacancies, $\bar{C}_v^L$, and cation interstitials, $\bar{C}_i^0$, respectively. Note the absence of a term for the relaxation of anion vacancies, because, again, the concentration of anion vacancies does not appear in the current [Eq. (8)], as a consequence of assuming Reaction (3), Figure 36, to be irreversible.

The next task is the calculation of $\frac{\Delta L}{\Delta U}$, $\frac{\Delta C_v^L}{\Delta U}$ and $\frac{\Delta C_i^0}{\Delta U}$. The rate of change of the thickness of the barrier layer is described by Eq. (16). Accordingly, by taking the total differential, we have

$$\frac{d\delta L}{dt} = j\omega\delta L e^{j\omega t} = \Omega\delta k_3 - \Omega\left(\frac{C_{H^+}}{C_{H^+}^0}\right)^n \delta k_7 = \Omega\left(\bar{k}_3 a_3 \delta U - \bar{k}_3 b_3 \delta L\right) - \Omega\bar{k}_7 a_7 \left(\frac{C_{H^+}}{C_{H^+}^0}\right)^n \delta U \quad (28)$$

or

$$L_U \equiv \frac{\Delta L}{\Delta U} = \frac{\Omega\left(\bar{k}_3 a_3 - \bar{k}_7 a_7 \left(\frac{C_{H^+}}{C_{H^+}^0}\right)^n\right)}{j\omega + \Omega\bar{k}_3 b_3} \quad (29)$$

3.6.2. Calculation of $\frac{\Delta C_i^0}{\Delta U}$

The flux density of interstitials is

$$J_i = -D_i \frac{\partial C_i}{\partial x} - \chi D_i K C_i \quad (30)$$

where D_i is the diffusion coefficient of the cation interstitials (cm^2 s^{-1}), $K = F\varepsilon/RT$, ε is the electric field strength inside the barrier layer (V cm^{-1}), R (=8.314 J mol^{-1} K^{-1}) is standard gas constant and T is the Kelvin temperature (K). The continuity equation is

$$\frac{\partial C_i}{\partial t} = D_i \frac{\partial^2 C_i}{\partial x^2} + \chi D_i K \frac{\partial C_i}{\partial x} \quad (31)$$

with the boundary conditions

$$-k_5 C_i = -D_i \frac{\partial C_i}{\partial x} - \chi D_i K C_i \quad at \quad x = 0$$
$$-k_2 = -D_i \frac{\partial C_i}{\partial x} - \chi D_i K C_i \quad at \quad x = L \quad (32)$$

Substitution $C_i = \bar{C}_i + \Delta C_i e^{j\omega t}$ into Eqs. (30) to (32) and linearization of boundary conditions relative to ΔU and ΔL yields:

$$j\omega\Delta C_i = \frac{\partial^2 \Delta C_i}{\partial x^2} + \chi D_i K \frac{\partial \Delta C_i}{\partial x} \quad (33)$$

or

$$-\bar{k}_5(\bar{C}_i^0 a_5 \Delta U + \Delta\bar{C}_i^0) = -D_i\left(\frac{\partial \Delta C_i}{\partial x}\right)_{x=0} - \chi D_i K \Delta C_i^0 \quad at\ x = 0 \tag{34}$$

$$-\bar{k}_2(a_2 \Delta U - b_2 \Delta L) = -D_i\left(\frac{\partial \Delta C_i}{\partial x}\right)_{x=L} - \chi D_i K \Delta C_i^L \quad at\ x = L \tag{35}$$

Analytical solution of the linear boundary problem 33 to 35 can be easily obtained and the sought value $\frac{\Delta C_i^0}{\Delta U}$ can be presented in the following form:

$$\frac{\Delta C_i^0}{\Delta U} = \frac{A+B}{\Delta U} = \Delta C_{iU}^0 + \Delta C_{iL}^0 \frac{\Delta L}{\Delta U} \tag{36}$$

where

$$\Delta C_{iU}^0 = \frac{b_{1U}(a_{22}-a_{21}) + b_{2U}(a_{11}-a_{12})}{a_{11}a_{22}-a_{12}a_{21}} \tag{37}$$

$$\Delta C_{iL}^0 = \frac{b_{2L}(a_{11}-a_{12})}{a_{11}a_{22}-a_{12}a_{21}} \tag{38}$$

$$r_{1,2} = \frac{-\chi K \pm \sqrt{\chi^2 K^2 + 4j\omega/D_i}}{2} \tag{39}$$

$$a_{11} = (r_1 + \chi K)D_i - \bar{k}_5 \quad and \quad a_{12} = (r_2 + \chi K)D_i - \bar{k}_5$$
$$a_{21} = (r_1 + \chi K)D_i e^{r_1 L} \quad and \quad a_{22} = (r_2 + \chi K)D_i e^{r_2 L} \tag{40}$$

$$b_{1U} = \bar{k}_5 a_5 \bar{C}_i^0 \quad and \quad b_{2U} = \bar{k}_2 a_2 \quad and \quad b_{2L} = -\bar{k}_2 b_2 \tag{41}$$

The reader should note that the expressions given above for cation interstitials are exactly the same for anion vacancies, with the oxidation number, χ, being replaced by 2, Subscript 2 being replaced by Subscript 3, and Subscript 5 being replaced by Subscript 6, so as to identify the correct reactions in Figure 36.

3.6.3. Calculation of $\frac{\Delta C_v^L}{\Delta U}$

By analogy it can be shown that:

$$\frac{\Delta C_v^L}{\Delta U} = \frac{Ae^{r_1 L} + Be^{r_2 L}}{\Delta U} = \Delta C_{vU}^L + \Delta C_{vL}^L \frac{\Delta L}{\Delta U} \Delta L \tag{42}$$

where

$$\Delta C_{vU}^L = \frac{(b_{1U}a_{22} - b_{2U}a_{12})e^{r_1 L} + (b_{2U}a_{11} - b_{1U}a_{21})e^{r_2 L}}{a_{11}a_{22}-a_{12}a_{21}} \tag{43}$$

$$\Delta C_{vL}^L = \frac{b_{2L}a_{11}e^{r_2 L} - b_{2L}a_{12}e^{r_1 L}}{a_{11}a_{22}-a_{12}a_{21}} \tag{44}$$

$$r_{1,2} = \frac{-\chi K \pm \sqrt{\chi^2 K^2 + 4j\omega/D_v}}{2} \tag{45}$$

where

$$a_{11} = (r_1 - \chi K)D_v \quad and \quad a_{12} = (r_2 - \chi K)D_v$$
$$a_{21} = \left[(r_1 - \chi K)D_v + \bar{k}_1\right]e^{r_1 L} \quad and \quad a_{22} = \left[(r_2 - \chi K)D_v + \bar{k}_1\right]e^{r_2 L} \tag{46}$$

$$b_{1U} = -\bar{k}_4 a_4 \quad and \quad b_{2U} = -\bar{k}_1 a_1 \bar{C}_v^L \quad and \quad b_{2L} = \bar{k}_1 b_1 \bar{C}_v^L \tag{47}$$

By substituting Eqs. (26), (29) and (42) into Eq. (23) we have the final result in the following form:

$$Y_F^0 = I_U + I_L L_U + I_v^L(\Delta C_{vU}^L + \Delta C_{vL}^L L_U) + I_i^0(\Delta C_{iU}^0 + \Delta C_{iL}^0 L_U) \tag{48}$$

The total impedance of the system, which comprises all of the contributory interfacial phenomena, including those at the metal/film/solution interphase plus the resistance of the solution between the surface of the outer layer and the tip of the Luggin probe can be represented by an electrical equivalent circuit. Figure 37 shows the equivalent circuit for the metal/film/solution interphasial system that is adopted here, in order to analyze the impedance response of the passive copper in deaerated 0.1 M *NaCl* solution containing sulphur species.

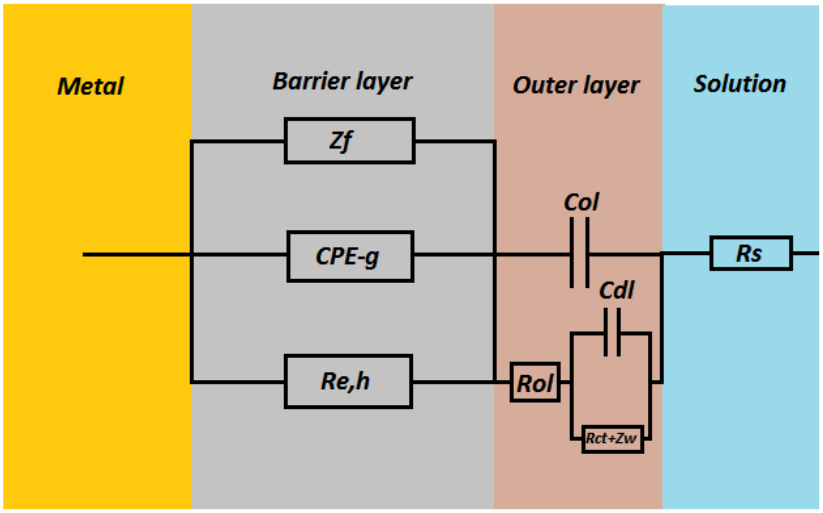

Figure 37. Equivalent electrical circuit describing the total impedance of the system, Z_f: faradaic impedance, *CPE-g*: geometrical constant phase element, $R_{e,h}$: electronic resistance, C_{ol}: outer layer capacitance, R_{ol}: outer layer resistance, C_{dl}: double layer capacitance, R_{ct}: charge transfer resistance, Z_w: Warburg impedance, R_s: solution resistance.

The total impedance of the system is expressed by Eq. (49):

$$Z = \left[\frac{1}{Z_F} + \frac{1}{Z_{CPE-g}} + \frac{1}{Z_{Re,h}}\right]^{-1} + \left[\frac{1}{Z_{Col}} + \frac{1}{Z_{Rol} + \left[\frac{1}{Z_{Cdl}} + \frac{1}{Z_{Rct+Z_W}}\right]^{-1}}\right]^{-1} + R_s \tag{49}$$

where Z_F is the faradaic impedance associated with the reactions occurring at the m/bl and bl/s interfaces. $Z_{CPE\text{-}g}$ is the geometric capacitance of the barrier layer. The geometric capacitance also incorporates the space charge capacitance and the two are assumed to be in parallel, because the semi-conductor junction lies within the "plates" (interfaces) of the barrier layer. As such, the larger of the two dominates

and that is reckoned to be the dielectric capacitance of the barrier layer, as given by the parallel plate capacitor formula. In the present analysis, we represent the geometrical capacitance by a constant phase element (*CPE*), because, on a polycrystalline substrate, there is expected a distribution of the passive film thickness to exist on the various grain faces exposed to the solution and hence it is expected that a distribution will also exist in the capacitance of the film. $R_{e,h}$ is the resistance against the movement of the free electrons and holes through the barrier layer, C_{ol} and R_{ol} are the capacitance and resistance of the outer layer respectively. Z_{Cdl} and R_{ct} are the double layer capacitance and charge transfer resistance associated with the redox reactions occurring at bl/s interface. This redox couple, which accepts the electronic charge, short-circuiting the barrier layer that is generated by ionization of the defects, might be H_2/H^+, or Cu^{2+}/Cu^+, for example, depending upon the potential and species present in the solution. Z_w is the Warburg impedance associated with diffusion of the ionic species in the electrolyte and R_s is the resistance of the electrolyte between the outer layer and the tip of the Luggin probe.

3.7. Extraction of model parameter values from EIS data

The Genetic curve fitting approach was selected for optimizing the PDM on the EIS experimental data, in order to extract values for the model parameters [68,69]. Briefly, curve fitting ("optimization") is the process of obtaining a representation of a multi-variate data set by an "objective function" that describes a physico-electrochemical system, at least as employed here. The main objective of optimization is to find the set of parameter values that minimize the total error determined from the difference between the observed dependent variable values, $Z(\omega)$, and those calculated from the derived parameter values over the considered data set. After selecting a functional form and setting up the error metrics, curve fitting becomes an optimization problem. It is a common method used to reconcile models to observations and for developing optimal solutions to different kinds of problems, such as simulation and statistical inference [68–71]. Even though there have been many ways proposed to approach curve fitting ("optimization") problems, there are few general techniques for complex functions with no derivative information and/or that are non-linear in form. Differential Evolution (DE) is a popular technique in evolutionary computation research [72]. It is capable of handling a large number of parameters and a rotated, multi-modal solution space. Evolutionary computation (EC) techniques seek to emulate the evolution of natural biological systems in order to find an optimal solution for a given problem. Genetic algorithms (GA) are used for the optimization of complicated problems in a wide range of applications such as engineering design, economic decisions, etc. Apparently, Holland was the first to employ genetic algorithms as described in the ground-breaking book on genetic algorithms, "Adaptation in Natural and Artificial Systems" [68]. A GA has been used in very few prior cases to fit impedance data, most notably by VanderNoot and Abrahams [69], and apart from work coming from this laboratory, DE has never been used. GA is not commonly used to fit impedance models, because they are computationally taxing and the functions are generally simple, making a gradient method more convenient. This is not the case with the PDM, however.

The optimization flow diagram employed in this study is shown in Figure 38. The important point is whether the parameter values that are obtained by optimization and used to calculate "theoretical impedance data", when combined with the experimental impedance data, satisfy the selected convergence criteria. If convergence is not satisfied, the calculation is returned to the step prior to optimization to begin the optimization anew, generally by assuming different initial estimates for the various

parameters in the model. It is important to note that there is no guarantee of finding the global optimum solution to a problem, even when using genetic algorithms like any other stochastic methods. However, DE is much more efficient than a purely random search, and given sufficient time and an appropriate objective function, excellent agreement can be found between the model and observation.

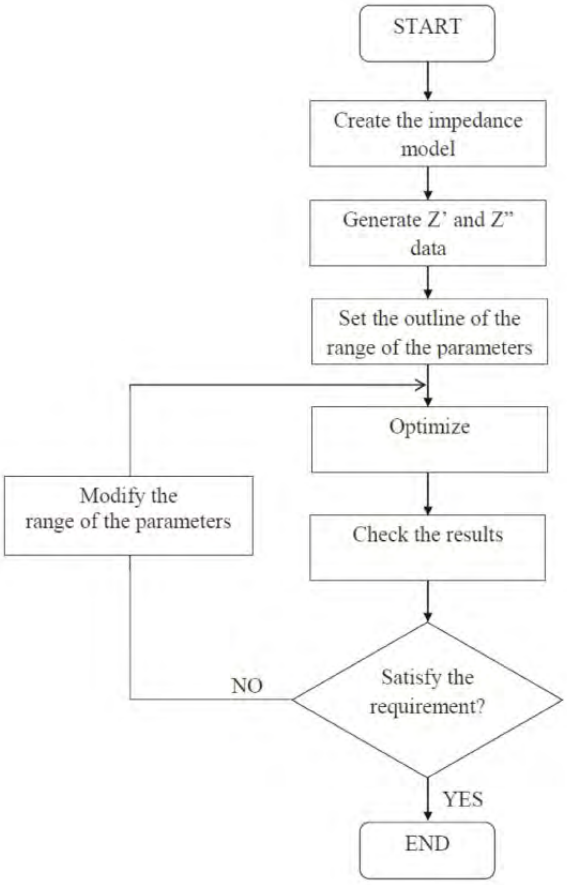

Figure 38. Optimization flow chart.

The optimization procedure ends if the result satisfies the selected convergence criteria and the following requirements: (1) All the parameter values are physically reasonable and should exist within known bounds; (2) The calculated $Z'(\omega)$ and $Z''(\omega)$ should agree with the respective experimental results in both the Nyquist and Bode planes; (3) The parameters, such as the polarizability of the barrier layer/outer layer interface (α), the electric field strength across barrier layer (ε), the standard rate constants, (k_i^{00}), the transfer coefficients for the point defect generation and annihilation at the barrier layer interfaces (α_i) , and the constant (Φ^0_{BOI}) should be potential-independent [35]; and (4) The calculated current density and barrier layer thickness, as estimated from the parameter values obtained from the optimization, should be in reasonable agreement with the steady-state experimental values. The most controversial issue with respect to the PDM is the postulated independence of the electric field strength of applied voltage. Thus, the PDM predicts that the steady-state thickness of the barrier layer varies linearly with voltage as

$$L_{ss} = \frac{1-\alpha}{\varepsilon}(V - V_0) \qquad (50)$$

where α is the polarizability of the bl/s interface and ε is the electric field strength (V cm^{-1}). This relationship is ubiquitous in anodic film studies [35] indicating that ε must be constant or that ε and $1-\alpha$ must vary with voltage in a complementary manner. The latter is rejected, because all of the data of which we are aware indicate that α is a constant, which is what it is assumed to be in the PDM. The second justification comes from the properties of tunnel diodes (Esaki junctions), which have many of the characteristics of the passive films, e.g., they are degenerately doped and have very narrow depletion regions characterized by an electric field strength that is buffered by Esaki (band-to-band) tunnelling, as is explained in Reference [35]. In this process, if any stress causes the electric field to increase (e.g., an increase in the applied voltage), an internal tunnelling current, which is a function of ε flows and produces a separation of charge that opposes the field. That is, the electric field strength is "buffered". Note that neither the steady-state current density nor the steady-state passive film thickness were employed in the optimization procedure. The *Igor Pro* (*Version 6.2.1.0, ©1988-2010 WaveMetrics, Inc*.) software with a custom software interface powered by Nelson's "gencurvefit" [73] package was used in this work for optimization, so as to obtain values for the standard rate constants (k_i^{00}), transfer coefficients (α_i) (for the *i* elementary interfacial reactions), the polarizability of the barrier layer/outer layer interface (α), the electric field strength across barrier layer (ε), and other parameters as described below. A freely distributed interface is now available to effectively leverage gencurvefit for the optimization of complex impedance functions [74].

Figures 39 through 44 show the typical experimental impedance spectra for the passive copper in a deaerated 0.1 M *NaCl* solution as a function of the applied potential, sulphide ion concentration, and solution temperature. The best fit results, calculated from the parameters obtained from the optimization of the proposed mechanism based on the PDM listed in Tables 4 and 5, are also included in these figures as solid lines. One can see that the correlation between the experiment and the model is fairly good, indicating that the proposed model can provide a reasonable account of the observed experimental data. It should be noted that, as stated before, the obtained parameters not only should reproduce the experimental impedance spectra, but also deliver the values with a reasonable physical meaning. Obtained kinetic parameters such as standard rate constants, transfer coefficients, and defect diffusivity listed in Tables 4 and 5, show no systematic dependency on the applied potential as required by the fundamental electrochemical kinetic theory. This is a good test of the viability of the proposed model and obtained parameters.

An important finding is that the rate constants for the reactions dealing with cation interstitials (k_2) and cation vacancies (k_1) formation have the lowest and highest value respectively. This indicates that cation vacancies are the dominant defect in the defective barrier layer structure, which is consistent with the p-type semiconductor character observed in the Mott-Schottky analysis. Another feature needs to be noted in Tables 4 and 5 is the smallest value of the transfer coefficient of Reaction 4 (i.e. α_4). From the fundamental theories of electrochemistry, it is known that transfer coefficient can have any value between 0 and 1, based on the energy state on the reaction coordinate. Since the transfer coefficient is defined as a measure of the fraction of the path from the initial state to the final state at which the activated complex occurs, the activated complex for Reaction 4 is judged to be more "initial state" –like than "final state" –like.

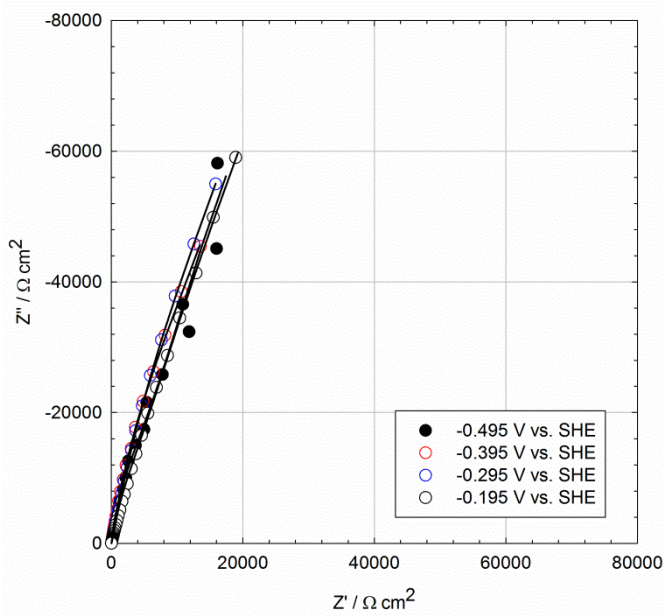

Figure 39. Experimental and simulated Nyquist plots for copper in a deaerated 0.1 M *NaCl* + 2×10^{-4} M $Na_2S.9H_2O$, T=25°C as a function of applied potential, solid lines show the best fit calculation according to the PDM.

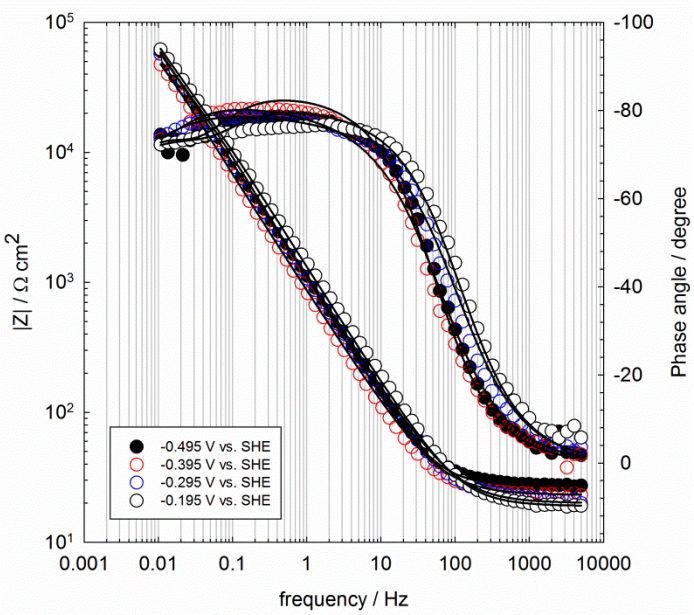

Figure 40. Experimental and simulated Bode plots for copper in a deaerated 0.1 M *NaCl* + 2×10^{-4} M $Na_2S.9H_2O$, T=25°C as a function of applied potential, solid lines show the best fit calculation according to the PDM.

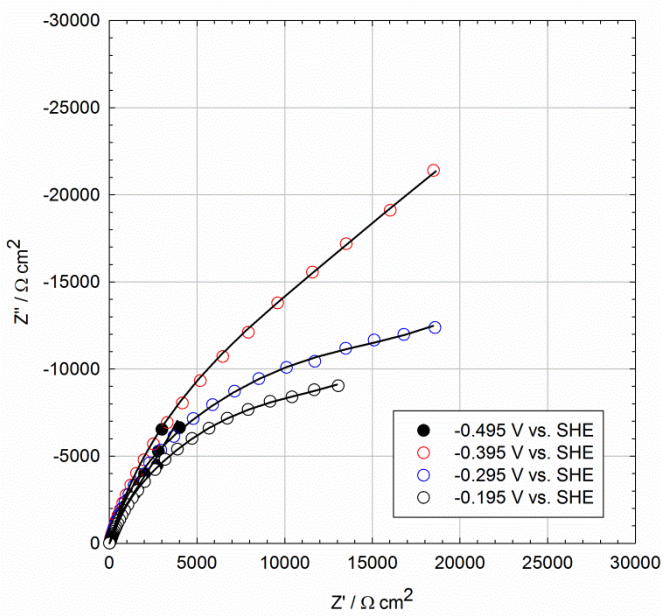

Figure 41. Experimental and simulated Nyquist plots for copper in a deaerated 0.1 M *NaCl* + 2×10^{-4} M $Na_2S.9H_2O$, T=50°C as a function of applied potential, solid lines show the best fit calculation according to the PDM.

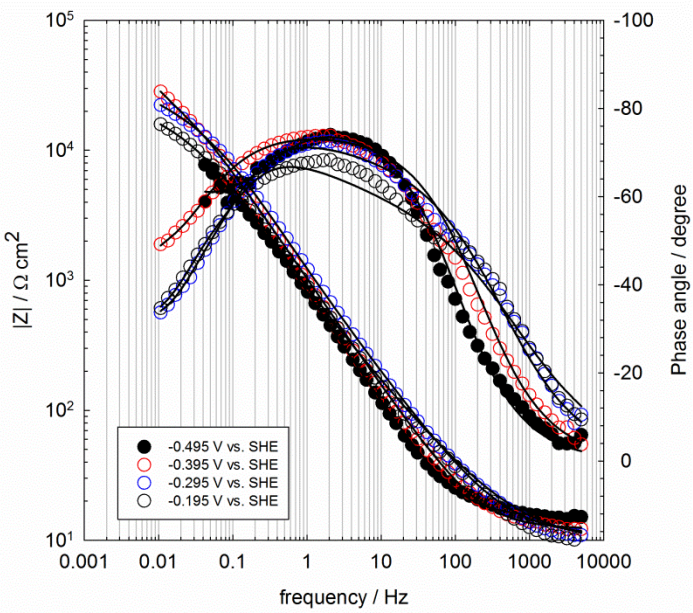

Figure 42. Experimental and simulated Bode plots for copper in a deaerated 0.1 M *NaCl* + 2×10^{-4} M $Na_2S.9H_2O$, T=50°C as a function of applied potential, solid lines show the best fit calculation according to the PDM.

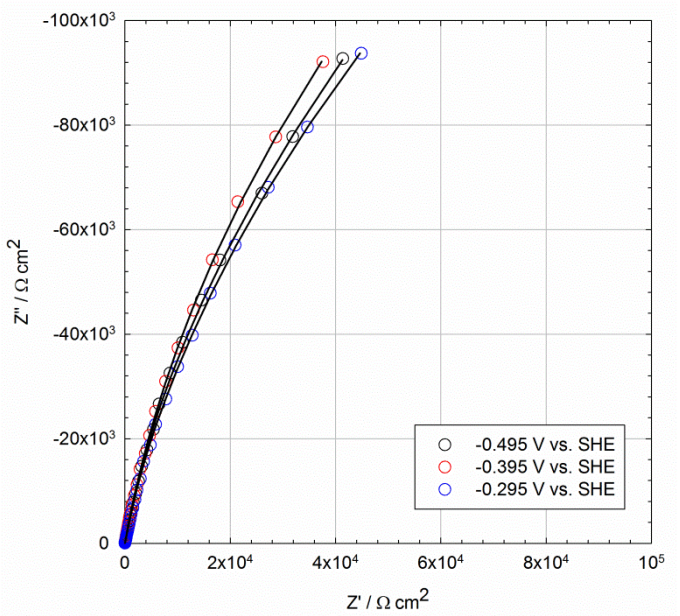

Figure 43. Experimental and simulated Nyquist plots for copper in a deaerated 0.1 M *NaCl* + 2×10^{-4} M $Na_2S.9H_2O$, T=75°C as a function of applied potential, solid lines show the best fit calculation according to the PDM.

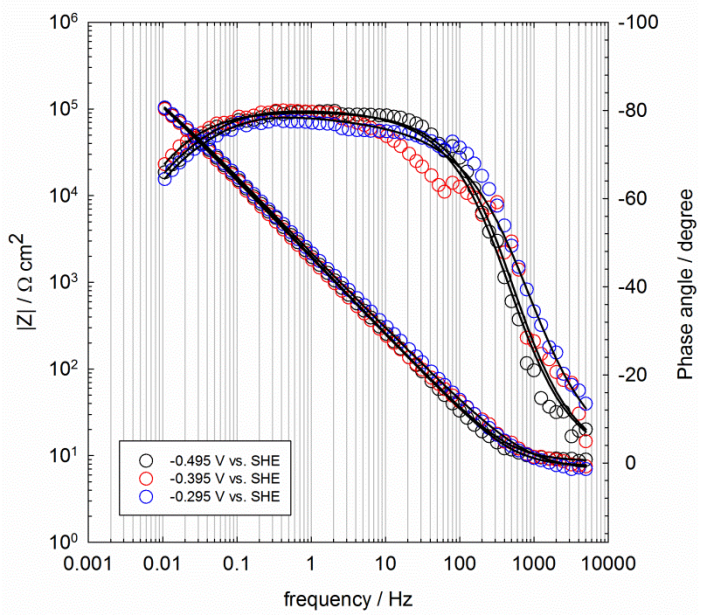

Figure 44. Experimental and simulated Bode plots for copper in a deaerated 0.1 M *NaCl* + 2×10^{-4} M $Na_2S.9H_2O$, T=75°C as a function of applied potential, solid lines show the best fit calculation according to the PDM.

Table 4. Averaged kinetic parameters obtained from the PDM optimization of copper in a deaerated 0.1 M *NaCl*+2×10^{-4} M $Na_2S.9H_2O$ as a function of temperature.

Parameter	T=25°C	T=50°C	T=75°C	Origin
α	0.26	0.20	0.13	1st stage optim
α_1	0.44±0.05	0.33±0.02	0.35±0.05	2nd stage optim
α_3	0.21±0.05	0.39±0.01	0.38±0.03	2nd stage optim
α_4	0.07±0.02	0.05±0.01	0.04±0.01	2nd stage optim
n	-0.15	-0.15	-0.15	1st stage optim
δ	1	1	1	Assumed
χ	1	1	1	Assumed
$\boldsymbol{k_1^{00}}$ (s^{-1})	4.23(±0.15)×10^{-09}	8.21(±0.01)×10^{-09}	1.82(±0.32)×10^{-08}	2nd stage optim
$\boldsymbol{k_2^{00}}$ (mol cm^2 s^{-1})	3.08(±0.34)×10^{-19}	5.83(±0.11)×10^{-19}	5.80(±0.43)×10^{-19}	2nd stage optim
$\boldsymbol{k_3^{00}}$ (mol cm^2 s^{-1})	3.10(±0.45)×10^{-12}	7.22(±0.15)×10^{-12}	1.00(±0.24)×10^{-11}	2nd stage optim
$\boldsymbol{k_4^{00}}$ (mol cm^2 s^{-1})	7.00(±0.17)×10^{-12}	3.02(±0.12)×10^{-10}	3.00(±0.22)×10^{-10}	2nd stage optim
$\boldsymbol{k_7^{00}}$ (mol cm^2 s^{-1})	7.31(±0.12)×10^{-13}	8.35(±0.02)×10^{-13}	5.31(±0.19)×10^{-13}	2nd stage optim
$\boldsymbol{k_1}$ (s^{-1})	3.52(±0.15)×10^{-07}	1.78(±0.01)×10^{-08}	1.64(±0.32)×10^{-08}	Calculated
$\boldsymbol{k_2}$ (mol cm^2 s^{-1})	1.85(±0.34)×10^{-16}	3.63(±0.11)×10^{-18}	4.61(±0.43)×10^{-19}	Calculated
$\boldsymbol{k_3}$ (mol cm^2 s^{-1})	2.46(±0.45)×10^{-11}	1.79(±0.15)×10^{-11}	8.96(±0.24)×10^{-12}	Calculated
$\boldsymbol{k_4}$ (mol cm^2 s^{-1})	7.85(±0.17)×10^{-13}	7.72(±0.12)×10^{-11}	1.22(±0.22)×10^{-10}	Calculated
$\boldsymbol{k_7}$ (mol cm^2 s^{-1})	7.31(±0.12)×10^{-13}	8.35(±0.02)×10^{-13}	5.31(±0.19)×10^{-13}	Calculated
CPE-g (S s^{φ} cm^{-2})	3.96(±1.33)×10^{-04}	3.87(±1.24)×10^{-04}	1.45(±0.25)×10^{-04}	2nd stage optim
CPE-φ	0.81(±0.01)	0.73(±0.09)	0.84(±0.03)	2nd stage optim
T (K)	298	323	348	Measured
pH	10.18	8.88	8.18	Measured
ε (V cm^{-1})	2.80(±0.10)×10^{+05}	2.55(±0.02)×10^{+05}	2.34(±0.23)×10^{+05}	1st stage optim
C_{dl} (F cm^{-2})	1.66(±0.38)×10^{-05}	1.62(±0.95)×10^{-05}	4.84(±2.89)×10^{-05}	2nd stage optim
R_s (Ω cm^2)	27	15	8.5	Estimated
D_v (cm^2 s^{-1})	4.22(±3.72)×10^{-13}	7.48(±4.90)×10^{-11}	9.20(±1.05)×10^{-11}	2nd stage optim
R_{ol} (Ω cm^2)	8.04(±5.55)×10^{+04}	6.64(±4.23)×10^{+03}	1.60(±0.93)×10^{+05}	2nd stage optim
C_{ol} (F cm^{-2})	3.52(±1.02)×10^{-04}	5.95(±2.77)×10^{-04}	3.69(±2.52)×10^{-04}	2nd stage optim

Table 5. Averaged kinetic parameters obtained from the PDM optimization of copper in a deaerated 0.1 M *NaCl* at T=25°C, as a function of total sulphur concentration.

Parameter	$[S_T]$=2×10^{-4} M	$[S_T]$=4×10^{-4} M	$[S_T]$=2×10^{-3} M	Origin
α	0.26	0.26	0.26	1st stage optim
α_1	0.44±0.05	0.44±0.02	0.44±0.04	2nd stage optim
α_3	0.21±0.05	0.18±0.02	0.17±0.02	2nd stage optim
α_4	0.07±0.02	0.05±0.01	0.05±0.01	2nd stage optim
n	-0.15	-0.15	-0.15	1st stage optim
δ	1	1	1	Assumed
χ	1	1	1	Assumed
$\boldsymbol{k_1^{00}}$ (s^{-1})	4.23(±0.15)×10^{-09}	4.20(±0.39)×10^{-09}	4.23(±1.11)×10^{-09}	2nd stage optim
$\boldsymbol{k_2^{00}}$ (mol cm^2 s^{-1})	3.08(±0.34)×10^{-19}	3.00(±2.55)×10^{-18}	7.08(±4.73)×10^{-17}	2nd stage optim
$\boldsymbol{k_3^{00}}$ (mol cm^2 s^{-1})	3.10(±0.45)×10^{-12}	3.00(±0.01)×10^{-13}	3.10(±0.01)×10^{-13}	2nd stage optim
$\boldsymbol{k_4^{00}}$ (mol cm^2 s^{-1})	7.00(±0.17)×10^{-12}	7.00(±0.10)×10^{-10}	3.00(±0.35)×10^{-09}	2nd stage optim
$\boldsymbol{k_7^{00}}$ (mol cm^2 s^{-1})	7.31(±0.12)×10^{-13}	7.31(±0.01)×10^{-14}	7.31(±0.01)×10^{-14}	2nd stage optim
$\boldsymbol{k_1}$ (s^{-1})	3.52(±0.15)×10^{-07}	1.00(±0.39)×10^{-06}	2.40(±1.11)×10^{-06}	Calculated
$\boldsymbol{k_2}$ (mol cm^2 s^{-1})	1.85(±2.34)×10^{-16}	8.80(±2.55)×10^{-15}	7.24(±4.73)×10^{-13}	Calculated
$\boldsymbol{k_3}$ (mol cm^2 s^{-1})	2.46(±0.45)×10^{-11}	2.78(±0.01)×10^{-12}	3.53(±0.01)×10^{-12}	Calculated
$\boldsymbol{k_4}$ (mol cm^2 s^{-1})	7.85(±0.17)×10^{-13}	1.33(±0.10)×10^{-10}	5.31(±0.35)×10^{-10}	Calculated
$\boldsymbol{k_7}$ (mol cm^2 s^{-1})	7.31(±0.12)×10^{-13}	7.31(±0.01)×10^{-14}	7.31(±0.01)×10^{-14}	Calculated
CPE-g (S s^{φ} cm^{-2})	3.96(±1.33)×10^{-04}	2.07(±0.8)×10^{-04}	1.56(±0.01)×10^{-02}	2nd stage optim
CPE-φ	0.81(±0.01)	0.76(±0.05)	0.38(±0.05)	2nd stage optim
T (K)	298	298	298	Measured
pH	10.18	10.54	11.23	Measured
ε (V cm^{-1})	2.80(±0.10)×10^{+05}	2.40(±0.10)×10^{+05}	3.77(±0.45)×10^{+05}	1st stage optim
C_{dl} (F cm^{-2})	1.66(±0.38)×10^{-05}	3.66(±2.53)×10^{-03}	1.15(±0.77)×10^{-02}	2nd stage optim
R_s (Ω cm^2)	27	23	17	Estimated
D_v (cm^2 s^{-1})	4.22(±3.72)×10^{-13}	7.74(±4.49)×10^{-12}	2.99(±4.67)×10^{-11}	2nd stage optim
R_{ol} (Ω cm^2)	8.04(±5.55)×10^{+04}	3.86(±2.55)×10^{+03}	3.85(±2.17)×10^{+02}	2nd stage optim
C_{ol} (F cm^{-2})	3.52(±1.02)×10^{-04}	2.31(±0.89)×10^{-03}	2.58(±1.90)×10^{-03}	2nd stage optim

As mentioned in the previous section, the rate of change of the barrier layer thickness that forms on a metal surface can be expressed as

$$\frac{dL}{dt} = \Omega k_3^0 e^{a_3 V} e^{b_3 L} e^{C_3 pH} - \Omega k_7^0 \left(\frac{C_{H^+}}{C_{H^+}^0}\right)^n e^{a_7 V} e^{C_7 pH} \qquad (51)$$

where Ω is the molar volume of the barrier layer per cation, C_{H^+} is the concentration of hydrogen ion, $C_{H^+}^0$ is the standard state concentration, and "n" is the kinetic order of the barrier layer dissolution reaction with respect to H^+. Definitions of the other parameters are listed in Tables 2 and 3. It should be mentioned that, since the pH of the solution was higher than the pH of zero charge for Cu_2S and CuS dissolution (PZC<3.5 [75]), "n" should be a negative value as it is obtained in the optimization. Another point to be noticed is that the rate of the dissolution reaction is potential dependent if the oxidation state of copper in the barrier layer is different from its oxidation state in the solution. However, under an anoxic condition, the oxidation state of copper in both phases is +1. Therefore, the rate of film dissolution is considered to be potential independent.

Under the steady-state condition, $\frac{dL}{dt} = 0$ and the steady-state thickness of the barrier layer can be derived as

$$L_{ss} = \left[\frac{1-\alpha}{\varepsilon}\right] V + \left[\frac{2.303n}{\alpha_3 \varepsilon \chi \gamma} - \frac{\beta}{\varepsilon}\right] pH + \frac{1}{\alpha_3 \varepsilon \chi \gamma} ln\left(\frac{k_3^0}{k_7^0}\right) \qquad (52)$$

Figures 45 (a) and (b) show a comparison between the calculated steady-state thicknesses of the barrier layer with the experimental results as a function of applied potential for different experimental conditions. The parameters obtained from the PDM optimization listed in Tables 4 and 5 were used to calculate the steady-state properties of the barrier layer, such as film thickness and current density, using Eqs. (52) and (8).
In order to calculate the experimental steady-state thickness, we used a well-known parallel plate capacitance formula (Eq. (53)) and assumed the value of the capacitance from the high frequency (1 kHz) imaginary part of the experimental impedance data.

$$C = \frac{\varepsilon \varepsilon^0}{d} \qquad (53)$$

Where ε is the dielectric constant (calibrated based on the obtained thickness), ε^0=8.85×10^{-14} (F cm^{-1}), d is the thickness of the film (cm), and C is the capacitance (F cm^{-2}). While the simulated thickness of the barrier layer is close to the values calculated based on the parallel plate capacitor for the lowest sulphide ion concentration (e.g. 2×10^{-4} M) for all of the three temperatures, obtained values for the higher concentrations of sulphide ion show a major discrepancy for some of the applied potentials. As can be seen, the thickness of the barrier layer increases with applied potential as predicted by the PDM [76].

The evolution of the steady-state thickness is shown as a function of temperature and sulphide ion concentration in Figures 46 (a) and (b). It is evident that steady-state thickness is increasing linearly with increases in solution temperature. Analysis of the obtained parameters from the optimization revealed that the $ln(\frac{k_3^0}{k_7^0})$ term shows an increase from approximately 4.75 to 7 with increases in temperature from 25°C to 75°C. This means that an increase of the film thickness as a result of a tem-

perature rise is probably due to an increase in the rate of film formation reaction (Reaction 3 in Figure 36).

The steady-state thickness is plotted against the sulphide concentration in solution in Figure 46 (b). In this case, the $ln(\frac{k_3^0}{k_7^0})$ term is calculated to be constant and around 4.5 and not a controlling factor on the thickness evolution. It seems that the pH of the solution, in this case, plays the most important role on the observed behavior, which is consistent with the PDM diagnostic criteria [76].

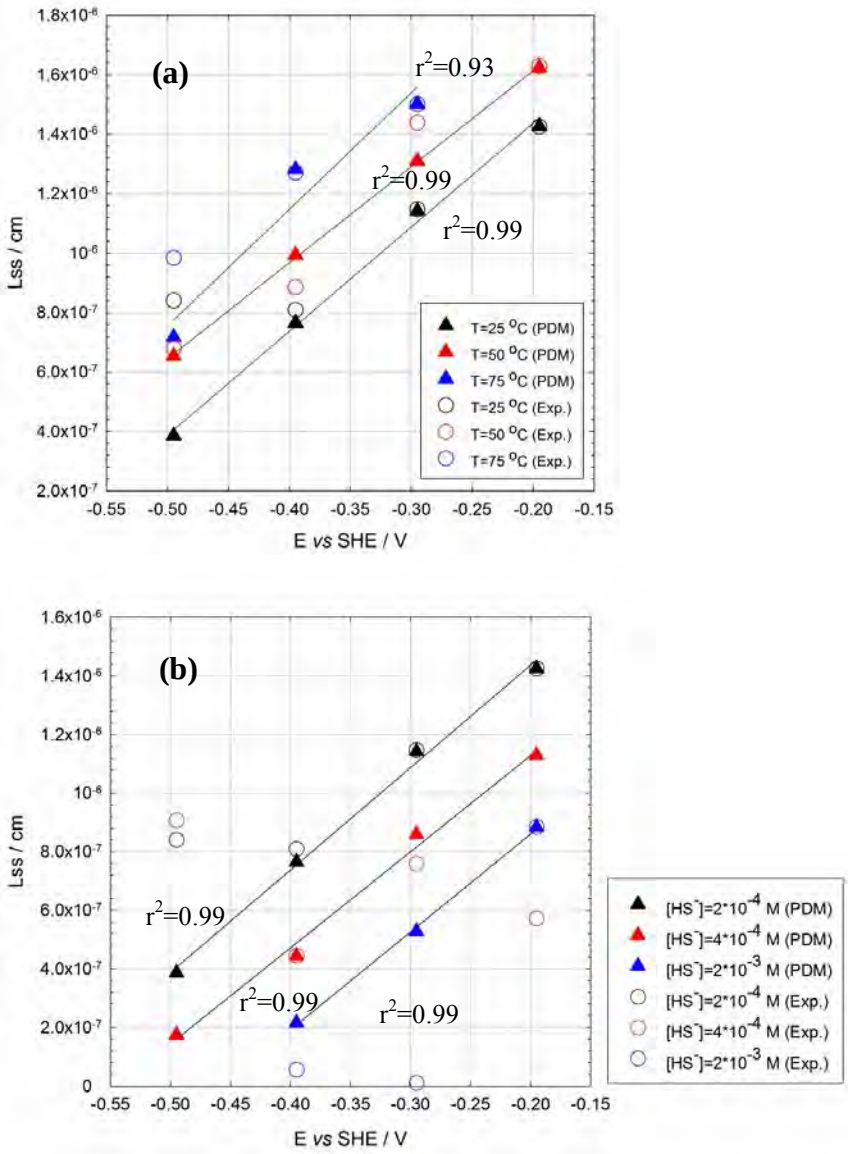

Figure 45. Plots of the calculated and experimental steady-state barrier layer thickness as a function of potentials for copper in (a) deaerated 0.1 M *NaCl*+2×10^{-4} M $Na_2S.9H_2O$ at different temperatures and (b) sodium chloride solution containing different concentration of sulphide species at 25°C.

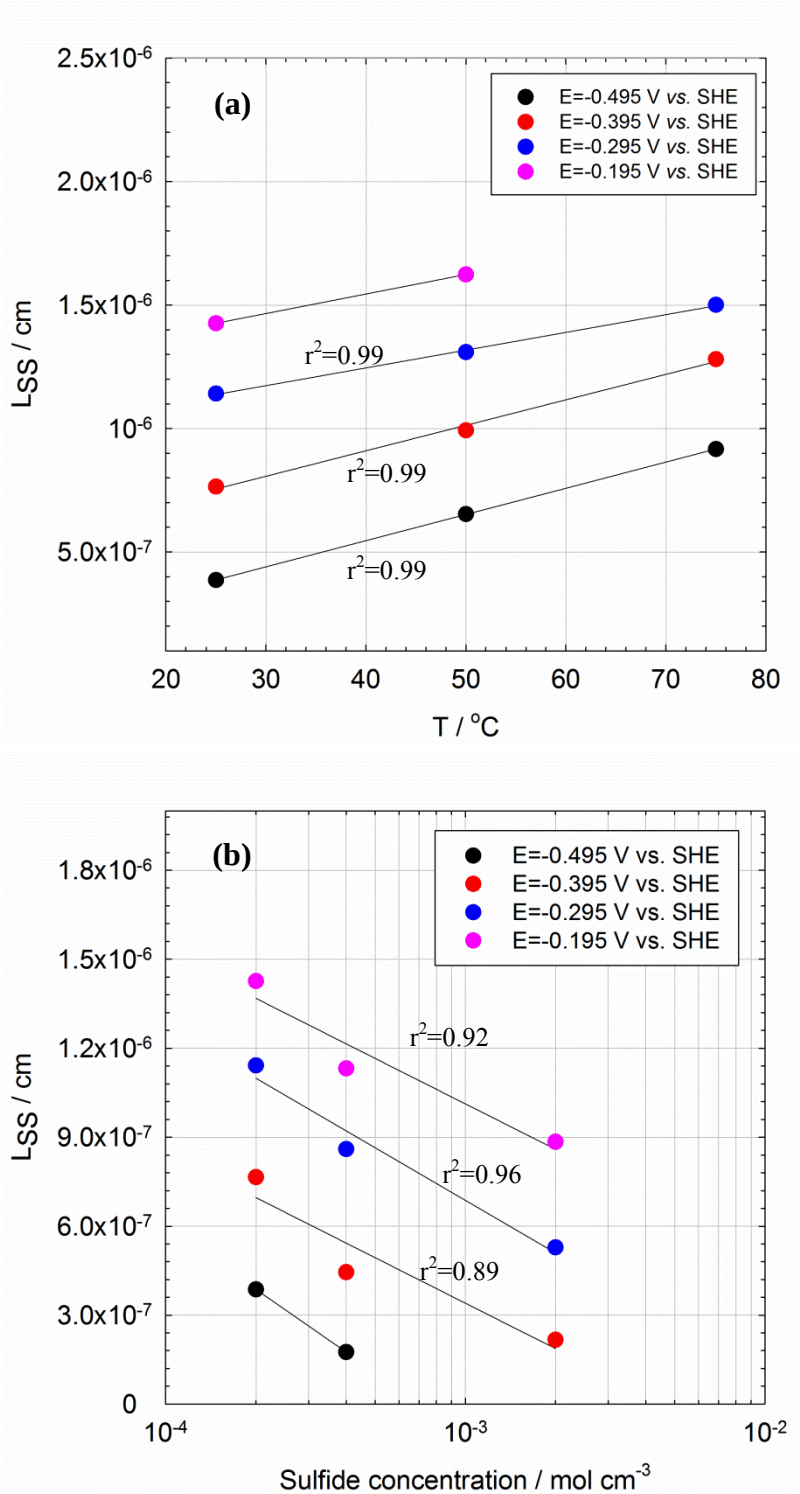

Figure 46. Plots of the calculated steady-state barrier layer thickness for copper as a function of (a) solution temperature and (b) sulphide concentration.

As stated earlier, the total current density, I_{ss}, is the sum of the contribution of all the interfacial reactions in Figure 36. As the Mott-Schottky results revealed, the sulphide passive films on copper exhibit a p-type semiconductor property; hence, the flux of cation vacancies through the barrier layer is higher than that of sulphur va-

cancies/copper interstitials and, as a result, the current density should be most significantly controlled by the interfacial reactions involved in cation vacancies generation and annihilation, i.e. reactions (1) and (4) in Figure 36. To achieve the steady-state condition, the PDM postulates that ($J_{V'_{Cu}}^{m/f} = J_{V'_{Cu}}^{f/s} = J_{V'_{Cu}}$):

$$I_{SS} = F\chi J_{V'_{Cu}}^{m/f} + F(\delta - \chi)J_{V'_{Cu}}^{f/s} = FJ_{V'_{Cu}} \qquad (54)$$

where $\chi = \delta = 1$ for Cu, $J_{V'_{Cu}}^{f/s}$ and $J_{V'_{Cu}}^{m/f}$ are the fluxes of copper vacancies at the f/s and m/f interfaces, respectively. One can see from Eq. (54) that the flux of copper vacancies at the f/s, m/f, and their transport through the film play the most important role in determining the steady-state current. We know that the flux of the copper vacancies at the f/s interface is a function of the vacancy generation rate (k_4) and we found that the rate constant of reaction 4, k_4, increases with increases in solution temperature, verifying that the formation of cation vacancies at the f/s interface was accelerated by rising the solution temperature, and therefore their flux increased with the temperature rise as well.

Since the passive sulphide film exhibits a p-type semiconductor character, sulphur vacancies are considered as the minority defects in the barrier layer with a small contribution to total current density. The preponderance of cation vacancies in the p-type passive films could be attributed to the fact that the energy of formation of V'_{Cu} is smaller relative to the energy of formation of $V_S^{\circ\circ}$ [52]. Even so, they can play a role in increasing the concentration and flux of copper vacancies. Considering the Schottky-pair reaction at the f/s interface, we postulate that the flux of copper vacancies is a function of the sulphur vacancies concentration. Thus, any decrease in the sulphur vacancies concentration will result in an increase in the copper vacancies flux. One possible scenario for a decrease in sulphur vacancies concentration is due to the incorporation of chloride ions (Cl^-) into sulphur vacancies sites. Another possibility could be the increase of adsorption of other anions presented in the solution to the sulphur vacancies as a result of increase in temperature.

The steady-state current for the passive sulphide film on copper in a sodium chloride solution containing different concentrations of sulphide species at different temperatures calculated based on the parameters obtained from the PDM optimization is shown in Figures 47 (a) and (b). As seen from these figures, there is a linear dependence between $log(I_{ss})$ and the applied potential, which is consistent with the PDM diagnostic criteria for p-type passive films.

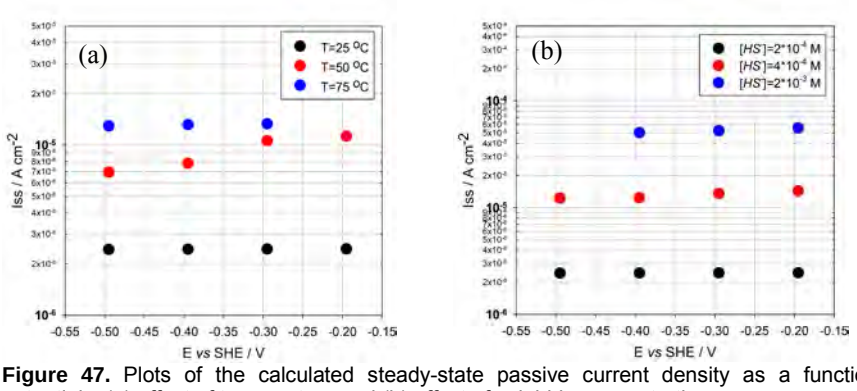

Figure 47. Plots of the calculated steady-state passive current density as a function of potentials, (a) effect of temperature and (b) effect of sulphide concentration.

Based on the PDM, the cation vacancies generated at the f/s interface move toward the m/f interface and the driving force for this transport phenomenon is primarily the electric field (ε) (i.e., migration). The diffusivity of copper vacancies through the passive layer was obtained directly from the optimization of the PDM as a function of temperature and is plotted in Figure 48. The diffusivity of copper vacancies (presumed dominant point defect) is in the range of 10^{-11} to 10^{-13} cm^2 s^{-1} and essentially independent of the applied potential. From this Arrhenius plot the activation energy (E_a) of copper vacancies in the passive sulphide film on copper was determined to be approximately 95 ($kJ\ mol^{-1}$) (=0.95 eV).

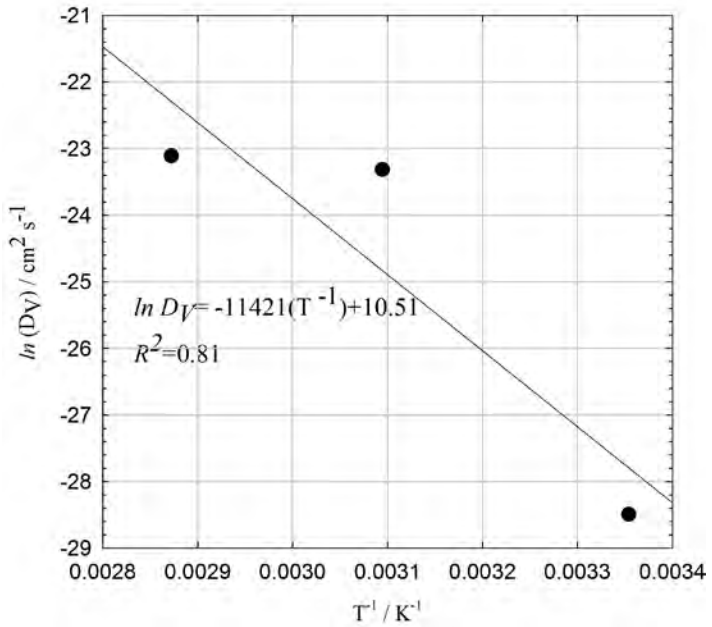

Figure 48. Diffusivity of copper vacancies as a function of temperature in a deaerated 0.1 M *NaCl*+2×10^{-4} M $Na_2S.9H_2O$ at Eapp. =-0.395 V vs. SHE.

From Figure 48 one can see that $D_{V_{Cu}'}$ increased significantly with increases in solution temperature. Systematic study of Cassaignore et al.[77] on diffusivity of copper in copper sulphide has revealed that diffusivity of copper vacancies depends strongly on the composition and its value falls in the range of 1.0×10^{-6} $cm^2.s^{-1}$ to 1.2×10^{-10} $cm^2.s^{-1}$ (at room temperature). It should be mentioned that, all of the reported values in the literature were measured on either natural copper sulphide electrodes or on electrodes prepared by pressing of the copper sulphide pellets. However, in the current work, the copper sulphide films were grown electrochemically.

Another interesting finding of the impedance analysis was the effect of the outer layer on the impedance response of the system. The effect of temperature on the resistance and capacitance of the outer layer is given in Figure 49 (a). As seen, both resistance and capacitance of the outer layer show dependency on the solution temperature, although not a major effect, which could provide some insight into the observed behavior as a result of increases in temperature. On the other hand, the effect of the outer layer on the impedance response of the system in solutions containing the higher concentration of sulphide species is much more important than in the lower concentration. Form Figure 49 (b) one can see that as a result of an increase in sulphide concentration the resistance of the outer layer decreases drastically from about 10^5 Ω cm^2 (at $[HS^-]=2\times10^{-4}$ M) to approximately 10^3 Ω cm^2 (at $[HS^-]=2\times10^{-3}$ M) and its capacitance shows an increase from approximately 4×10^{-4} F cm^{-2} (at $[HS^-]=2\times10^{-4}$ M) to about 2.5×10^{-3} F cm^{-2} (at $[HS^-]=2\times10^{-3}$ M). Observa-

tion of such a high capacitance is probably associated with the electrochemical adsorption of sulphide ions into the surface of the electrode or even its entrance into the barrier layer.

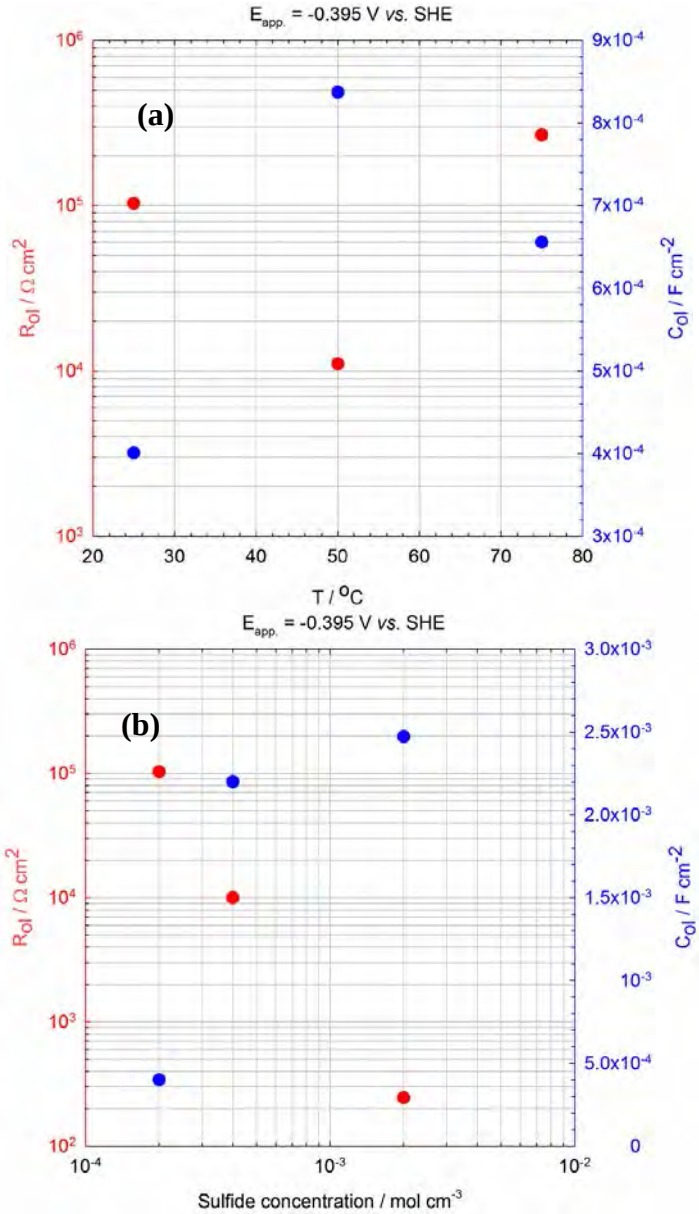

Figure 49. Evolution of outer layer resistivity and capacitance as a function of (a) temperature and (b) sulphide concentration.

3.8. Sensitivity Analysis

To determine the effect of different parameters on the overall impedance spectra, sensitivity analyses were performed by systematically varying each parameter in turn over wide ranges. Sensitivity analysis is a common methodology used to study the effect of parameter variations on the behavior of the proposed mathematical model [78]. In Figure 50, the impact of the values of some of the more important parameters on the impedance is displayed. To accurately ascertain the impact, the experimental impedance data are also included in these plots. It is evident that the

kinetic parameters for Reactions 1, 3, 4 and 7 and the corresponding transfer coefficients, have a major effect on the calculated impedance, particularly at low frequencies where the impedance is most sensitive to defect kinetic/transport phenomena (in contrast to high frequencies, where capacitive effects dominate). This sensitivity analysis, therefore, emphasizes the need to obtain accurate impedance data at very low frequencies, at least for frequencies as low as 10^{-3}Hz. On the other hand, outer layer resistance and capacitance play an important role in the wider frequency range (from medium to low frequency) than the kinetic parameters.

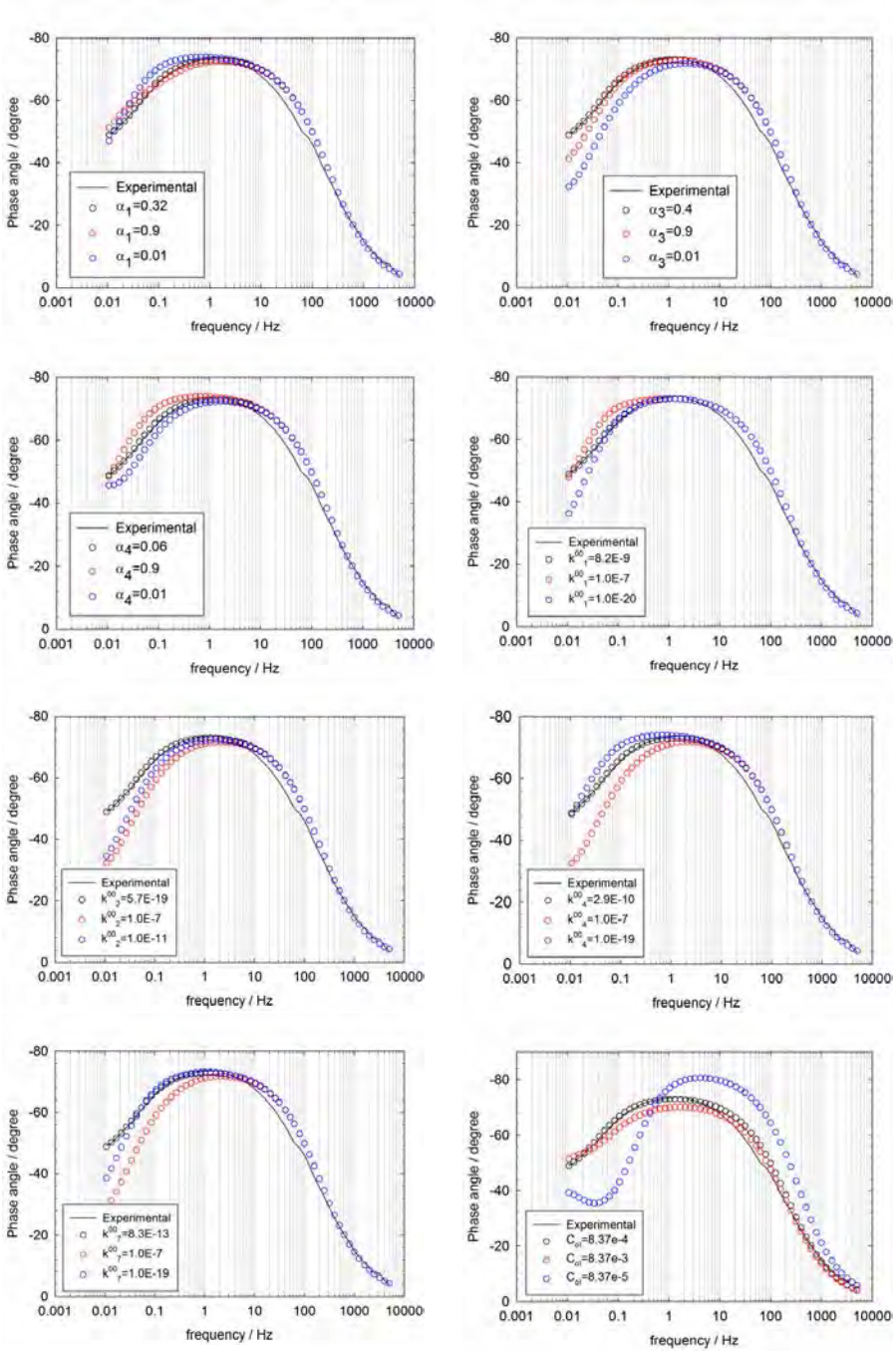

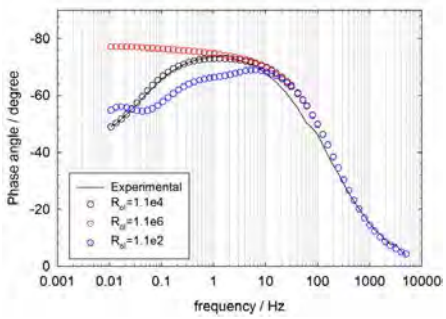

Figure 50. Sensitivity analysis showing the effect of model parameters on the calculated impedance.

4. Summary and conclusions

The corrosion behavior of pure copper in a deaerated sodium chloride solution containing sulphide species has been studied as a function of applied potential, solution temperature and sulphide ion concentrations by means of potentiodynamic and potentiostatic polarization, electrochemical impedance spectroscopy, Mott-Schottky analysis as well as X-ray photoelectron spectroscopy. The findings of this work are summarized as follows:

- The passive sulphide film formed potentiostatically on pure copper in a deaerated sodium chloride solution containing sulphide species is a p-type semiconductor due to the predominance of copper vacancies in the barrier layer. However, n-type character at potentials more negative than the passive potential were observed in the Mott-Schottky analysis at 25^{o}C and 50^{o}C, which may be attributed to the interfering effect of other electrochemical/chemical reactions such as water reduction/hydrogen evolution on the surface of the electrode or any change in the surface states of the barrier layer.
- The surface of the passive film formed on pure copper was examined by XPS. *Cu*, *S*, *O,* and *C* were detected from the survey scan. Analyses of the high resolution peak of *Cu*-2p, *S*-2p, and *Cu*-LMM revealed the possibility of the presence of both *CuS* and Cu_2S on the surface of the film.
- Electrochemical impedance spectroscopy data for the passive sulphide film formed on pure copper are interpreted in terms of the proposed model based on the PDM by optimizing the model onto the experimental data using a genetic algorithm approach.
- Analysis of the obtained kinetic parameters form optimization revealed that the rate constant for the reactions dealing with generation and annihilation of cation vacancies have the highest value in agreement with the p-type semiconductor character observed experimentally in the Mott-Schottky analysis.
- The steady-state thickness of the barrier layer, as calculated from the obtained parameters, increased linearly with applied potential as predicted by the PDM and was in good agreement with the experimental result of the lower sulphide concentration. In the case of the higher sulphide concentration, the model failed to predict the evolution of the barrier layer thickness with applied potential, which could be related to the higher corrosion rate and loss of passivity.

- The steady-state thickness showed an increase with an increase in solution temperature. This phenomenon can be attributed to the increase in the rate of the film formation reaction (Reaction 3) with the temperature rise.
- A linear dependence between the logarithm of steady-state current and applied potential was observed, which is consistent with the diagnostic criteria of the PDM for the p-type passive films.
- The diffusion coefficient of cation vacancies was obtained directly from the optimization of the proposed model onto the EIS experimental data and found to be essentially independent from the applied potential within the passive range. The diffusivity of the predominance defects (cation vacancies) increased with a rise in solution temperature from approximately 10^{-13} (cm^2 s^{-1}) at 25°C to 10^{-11} (cm^2 S^{-1}) at 75°C.
- The outer layer plays a role in the observed impedance data, especially at the higher concentrations of sulphide species (e.g. 2×10^{-3} M). Higher capacitance and lower resistance of the outer layer obtained from optimization of the proposed model can be attributed to the adsorption of sulphide/bisulphide species into the electrode surface and the higher porosity of the layer.

5. References

1. F. King, L. Ahonen, C. Taxén, U. Vuorinen, and L. Werme, *Swedish Nucl. Fuel Waste Manag. Co. Report, SKB TR 01-23, 2001* and *Posiva Oy Rep. POSIVA report 2002-01* (2002) (similar reports).
2. F. King, *Corrosion*, **69**, 986–1011 (2013).
3. F. King, C. Lilja, and M. Vähänen, *J. Nucl. Mater.*, **438**, 228–237 (2013).
4. D. D. Macdonald and S. Sharifi-Asl, *Swedish Radiation Safety Authority Report 2011:09*, 256 (2011).
5. S. De Sanchez and D. Schiffrin, *Corros. Sci.*, **22**, 585–607 (1982).
6. J. Bates and J. Popplewell, *Corrosion*, **31**, 269–275 (1975).
7. B. Syrett, *Corrosion*, **33**, 257–262 (1977).
8. B. Syrett, *Corros. Sci.*, **21**, 187–209 (1981).
9. J. Gudas and H. Hack, *Corrosion*, **35**, 67–73 (1979).
10. J. Gudas and H. Hack, *Corrosion*, **35**, 259–264 (1979).
11. B. C. Syrett, D. D. Macdonald, and S. S. Wing, *Corrosion*, **35**, 409–422 (1979).
12. D. D. Macdonald, B. C. Syrett, and S. S. Wing, *Corrosion*, **34**, 289–301 (1978).
13. E. Khairy and N. Darwish, *Corros. Sci.*, **13**, 141–147 (1973).
14. A. M. Alfantazi, T. M. Ahmed, and D. Tromans, *Mater. Des.*, **30**, 2425–2430 (2009).
15. M. G. De Chialvo and A. Arvia, *J. Appl. Electrochem.*, **15**, 685–696 (1985).
16. T. Eriksen, P. Ndalamba, and I. Grenthe, *Corros. Sci.*, **29**, 1241–1250 (1989).
17. B. Rosborg and J. Pan, *Electrochim. Acta*, **53**, 7556–7564 (2008).
18. V. Moll, *Electrochim. Acta*, **30**, 1011–1016 (1985).
19. E. Khairy and N. Darwish, *Corros. Sci.*, **13**, 149–164 (1973).
20. D. D. Macdonald, B. Syrett, and S. Wing, *Tech. Report, Off. Nav. Res.* (1978).
21. D. D. Macdonald, B. C. Syrett, and S. S. Wing, *Corrosion*, **35**, 367–378 (1979).
22. J. Chen, Z. Qin, and D. W. Shoesmith, *J. Electrochem. Soc.*, **157**, C338 (2010).
23. J. Chen, Z. Qin, and D. W. Shoesmith, *Electrochim. Acta*, **56**, 7854–7861 (2011).
24. J. M. Smith, J. C. Wren, M. Odziemkowski, and D. W. Shoesmith, *J. Electrochem. Soc.*, **154**, C431 (2007).

25. J. Smith, Z. Qin, F. King, and D. Shoesmith, *Sulphur-assisted Corros. Nucl. Dispos. Syst.*, 109–123 (2008).
26. J. Smith, Z. Qin, and D. Shoesmith, *17th Proc. Int. Corros. Cong.*, 1–9 (2009).
27. I. Betova et al., *Electrochem. Solid-State Lett.*, **6**, B19 (2003).
28. M. Bojinov and T. Laitinen, *MRS . Res. Soc. Symp. Proc.*, **807**, 1–6 (2004).
29. *Outokumpu Res.* (1997) www.hsc-chemistry.net.
30. S. Ahn, H. Kwon, and D. D. Macdonald, *J. Electrochem. Soc.*, **152**, B482 (2005).
31. D. D. Macdonald and M. Urquidi-Macdonald, *J. Electrochem. Soc.*, **137**, 2395–2402 (1990).
32. G. Kear, B. D. Barker, and F. C. Walsh, *Corros. Sci.*, **46**, 109–135 (2004).
33. J. Huang, X. Wu, and E.-H. Han, *Corros. Sci.*, **51**, 2976–2982 (2009).
34. A. Nozik and R. Memming, *J. Phys. Chem.*, **100**, 13061–13078 (1996).
35. D. D. Macdonald, *Pure Appl. Chem.*, **71**, 951–978 (1999).
36. I. Grozdanov and M. Najdoski, *J. Solid State Chem.*, **114**, 469–475 (1995).
37. J. Garche, C. Dyer, P. Moseley, and Z. Ogumi, *Encyclopedia of electrochemical power sources*, Elsevier B.V., (2009), p. 751–761.
38. V. Krylova and M. Andrulevičius, *Int. J. Photoenergy*, **2009**, 1–8 (2009).
39. D. Perry and J. Taylor, *J. Mater. Sci. Lett.*, **5**, 384–386 (1986).
40. M. Romand, M. Roubin, and J. Deloume, *J. Electron Spectros. Relat. Phenomena*, **13**, 229–242 (1978).
41. C. Wagner, *Faraday Discuss. Chem. Soc.*, **60**, 291–300 (1975).
42. V. I. Nefedov, Y. V. Salyn, P. M. Solozhenkin, and G. Y. Pulatov, *Surf. Interface Anal.*, **2**, 170–172 (1980).
43. V. Bhide and S. Salkalachen, *J. Phys. D Appl. Phys.*, **14**, 1647–1656 (1981).
44. J. C. W. Folmer and F. Jellinek, *J. Less Common Met.*, **76**, 153–162 (1980).
45. S. W. Goh, A. N. Buckley, and R. N. Lamb, *Miner. Eng.*, **19**, 204–208 (2006).
46. I. Nakai, Y. Sugitani, K. Nagashima, and Y. Niwa, *J. Inorg. Nucl. Chem.*, **40**, 789–791 (1978).
47. H. Kramers, *Zeitschrift fuer Phys.*, **53**, 422–428 (1929).
48. R. Kronig, *JOSA*, **12**, 547–557 (1926).
49. M. Urquidi-Macdonald, S. Real, and D. Macdonald, *Electrochim. Acta*, **35**, 1559–1566 (1990).
50. D. D. Macdonald and M. Urquidi-Macdonald, *J. Electrochem. Soc.*, **132**, 2316–2319 (1985).
51. M. Urquidi-Macdonald, S. Real, and D. D. Macdonald, *J. Electrochem. Soc.*, **133**, 2018–2024 (1986).
52. E. Sikora and D. D. Macdonald, *Electrochim. Acta*, **48**, 69–77 (2002).
53. C. Y. Chao, L. F. Lin, and D. D. Macdonald, *J. Electrochem. Soc.*, **129**, 1874–1879 (1982).
54. C. Y. Chao, L. F. Lin, and D. D. Macdonald, *J. Electrochem. Soc.*, **128**, 1187–1194 (1981).
55. L. F. Lin, C. Y. Chao, and D. D. Macdonald, *J. Electrochem. Soc.*, **128**, 1194–1198 (1981).
56. D. D. Macdonald, *J. Electrochem. Soc.*, **153**, B213 (2006).
57. H. Song and D. D. Macdonald, *J. Electrochem. Soc.*, **138**, 1408–1410 (1991).
58. D. D. Macdonald, E. Sikora, M. W. Balmas, and R. C. Alkire, *Corros. Sci.*, **38**, 97–103 (1996).
59. D. D. Macdonald and G. R. Englehardt, *ECS Trans.*, **28**, 123–144 (2010).
60. M. Urquidi and D. D. Macdonald, *J. Electrochem. Soc.*, **132**, 555–558 (1985).
61. L. Zhang and D. D. Macdonald, *Electrochim. Acta*, **43**, 2661–2671 (1998).
62. J. Ai, Y. Chen, M. Urquidi-Macdonald, and D. D. Macdonald, *J. Electrochem. Soc.*, **154**, C52 (2007).

63. J. Ai, Y. Chen, M. Urquidi-Macdonald, and D. D. Macdonald, *J. Electrochem. Soc.*, **154**, C43 (2007).
64. D. D. Macdonald and A. Sun, *Electrochim. Acta*, **51**, 1767–1779 (2006).
65. D. D. Macdonald, A. Sun, N. Priyantha, and P. Jayaweera, *J. Electroanal. Chem.*, **572**, 421–431 (2004).
66. S. Sharifi-Asl et al., *Electrochim. Acta*, **102**, 161–173 (2013).
67. S. Sharifi-Asl, D. D. Macdonald, a. Almarzooqi, B. Kursten, and G. R. Engelhardt, *J. Electrochem. Soc.*, **160**, C316–C325 (2013).
68. S. N. Sivanandam and S. N. Deepa, *Introduction to Genetic Algorithms*, Springer Verlag, (2007).
69. T. J. VanderNoot and I. Abrahams, *J. Electroanal. Chem.*, **448**, 17–23 (1998).
70. L. G. McMillion, A. Sun, D. D. Macdonald, and D. A. Jones, *Metall. Mater. Trans. A*, **36**, 1129–1141 (2005).
71. M. Gulsen, A. Smith, and D. Tate, *Int. J. Prod. Res.*, **33**, 1911–1923 (1995).
72. O. Kanoun, U. Tröltzsch, and H.-R. Tränkler, *Electrochim. Acta*, **51**, 1453–1461 (2006).
73. (2012) http://www.igorexchange.com/project/gencurvefit.
74. (2012) http://www.igorexchange.com/project/Ellis2.
75. M. Kosmulski, *Surface charging and points of zero charge*, CRC Press-Taylor & Francis Group, Boca Raton, FL, (2010), p. 1696.
76. D. D. Macdonald, S. R. Biaggio, and H. Song, *J. Electrochem. Soc.*, **139**, 170–177 (1992).
77. S. Cassaignon, T. Pauporté, J.-F. Guillemoles, and J. Vedel, *Ionics (Kiel).*, **4**, 364–371 (1998).
78. L. K. Bieniasz and B. Speiser, *J. Electroanal. Chem.*, **441**, 271–285 (1998).

Estimation of Maximum Possible Values of Corrosion Current Density and Corrosion Potential under Conditions of Copper Corrosion in a Swedish High Level Nuclear Waste Repository

1. Introduction

One of the main aims of the current report is the development of mixed potential models (MPMs) to predict the corrosion potential, E_{corr}, and corrosion rate (expressed as the corrosion current density, i_{corr}, or the rate of removal of the metal surface, V_{corr}) of copper canisters contained in the granitic rock repository being developed in Sweden for the disposal of high level nuclear waste (HLNW). These models are designed to provide estimates of E_{corr}, and i_{corr} as the system evolves along the corrosion evolutionary path (CEP). Comparison of E_{corr} with critical potentials for various localized corrosion processes, such as pitting corrosion, stress corrosion cracking, and crevice corrosion, is expected to indicate whether any of these localized corrosion processes are likely to occur in the repository at any time along the CEP. Integration of the corrosion rate, V_{corr}, yields the weight loss of copper and the dimensional change of the canister due to corrosion.

An example of such comprehensive model can be found in previous reports [1]. In accordance with the model considered in [1] the following electrochemical reactions take place at the copper/solution interface.

1.1. Anodic reaction

It is assumed that that copper metal loses much of its corrosion resistance in the presence of sulphide ion and other sulphur-containing species with the metal forming Cu_2S:

$$2Cu + HS^- + OH^- \xrightarrow{k_1} Cu_2S + H_2O + 2e^- \qquad (1)$$

1.2. Cathodic reactions

$$H_2 + 2OH^- \xleftrightarrow{k_2, k_{-2}} 2H_2O + 2e^- \quad (2)$$

$$4OH^- \xleftarrow{k_{-3}} O_2 + 2H_2O + 4e^- \quad (3)$$

$$2OH^- \xleftarrow{k_{-4}} H_2O_2 + 2e^- \quad (4)$$

1.3. Homogeneous reactions

$$HS^- + O_2 \xrightarrow{k_5} SP_1 \quad (5)$$

$$HS^- + H_2O_2 \xrightarrow{k_6} SP_2 \quad (6)$$

$$2H_2 + O_2 \xrightarrow{k_7} 2H_2O \quad (7)$$

$$H_2 + H_2O_2 \xrightarrow{k_8} 2H_2O \quad (8)$$

where SP_1 and SP_2 are unspecified bisulphide oxidation products that were considered to be inert at least at present analysis. Production of H_2, O_2 and H_2O_2 species due to the radiolysis of water were taken into account. Examples of numerical solution of corresponding systems of transport equations can be found in Ref. 1.
However, it is clear that not all kinetic parameters that are required for numerical or analytical solution of transport equations are known. Thus, for example, we have no information about rates of the chemical reactions (1) to (5) and accordingly our calculations will have only model character. However, it would be worth finding an upper estimate of the loss of copper from the wall of the container and an upper estimate of the corrosion potential during the period of 100,000 years, which is generally accepted as being the storage horizon for HLNW in Sweden. If it is found that this loss is negligible and the corrosion potential is much less than the critical potential for any localized corrosion process, we will be able to conclude that within the framework of the adopted model, the container will not fail within the storage horizon of 100,000 years.

Equation (1) which can be rewritten in the form [2-7]:

$$2Cu + HS^- \xrightarrow{k_1} Cu_2S + H^+ + 2e^- \quad (9)$$

shows from its stoichiometry that corrosion current density may be limited by the transport of HS^- ions. This possibility depends on the fate of Cu_2S species. Limiting diffusion current conditions can be realized if, for example, Cu_2S species participate in the reactions [8]:

$$Cu_2S + HS^- + H^+ \longrightarrow 2CuHS(aq) \quad (10)$$

or

$$Cu_2S + 3HS^- + H^+ \longrightarrow 2Cu(HS)_2^- \quad (11)$$

In combination with Reaction (9), Reactions (10) and (11) yield the following overall anodic reactions:

$$Cu + HS^- \longrightarrow CuHS(aq) + e^- \quad (12)$$

and

$$Cu + 2HS^- \longrightarrow Cu(HS)_2^- + e^- \quad (13)$$

It is clear that the rates of Reactions (12) and (13) are limited by transport of HS^- ions.
In addition, if we assume that HS^- ions are used for the formation of the porous outer layer in the form of Cu_2S or CuS, it is also clear that diffusion limitations connected with the transport of HS^- ions also exist in this process as well.
On the other hand, if the compound Cu_2S dissolves in accordance with the classical PDM reaction

$$Cu_2S + H^+ \longrightarrow 2Cu^+ + HS^- \quad (14)$$

the total anodic reaction can be rewritten as

$$Cu \longrightarrow Cu^+ + e^- \quad (15)$$

as a result of combination of Reactions (9) and (14) with the Cu_2S barrier layer existing as a semi-permeable membrane. It is evident that, in this case, no diffusion limitations for the anodic reaction may be observed. In the current report, we will consider the case when a diffusion limitation exists.

2. Estimation of maximum possible value of corrosion current density

Figure 1 yields schematic of canister located in the repository. The copper canisters are located in holes drilled into the floor of the drifts (tunnels), with the canisters being encased in bentonite, a clay mineral. Upon resaturation, after the tunnels are backfilled with crushed rock or other material, water penetrates into the bentonite, causing it to swell. Swelling decreases the porosity, thereby reducing the diffusivities of species to or from the canister surface. Additionally, clays generally possess high absorption capacities, which further impede the transport of ionic species through the bentonite matrix. Thus, the bentonite acts as an engineered barrier to the movement of corrosive species, such as HS^-, which activates copper by giving rise to an anodic process [the formation of Cu_2S, Reaction (9)] that occurs at a potential that is more negative than the potential of reduction of water to form hydrogen [reverse of Reaction (2)]. Thus the reduction of water becomes a viable partial cathodic reaction, thereby giving rise to the corrosion of copper in anoxic environments.

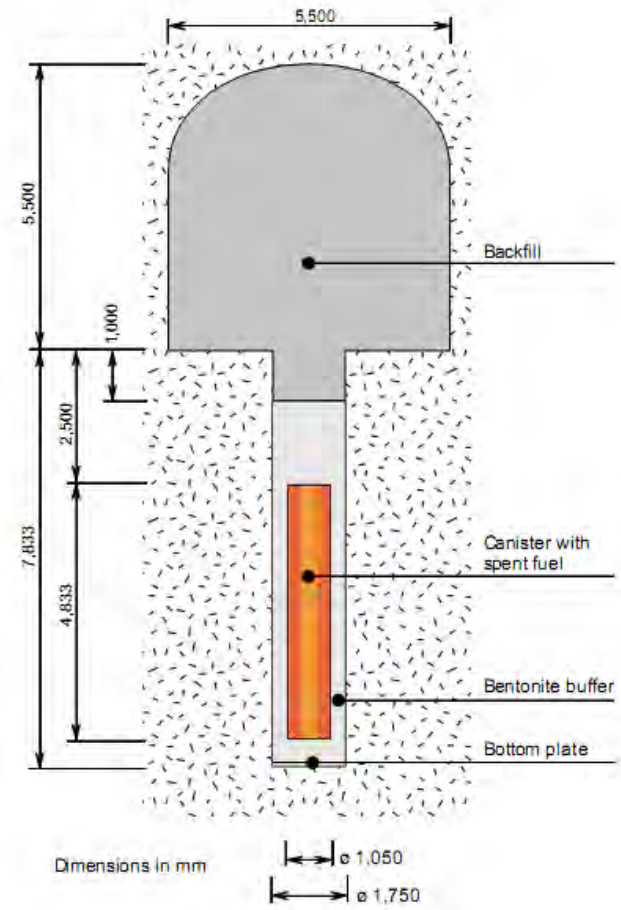

Figure 1. Schematic of canister emplaced concentrically with the bentonite buffer located in a cylindrical hole in the floor of a tunnel in the repository [9].

We solve the problem for the following idealized system: inside region of the infinite hollow cylinder with the inner radius r_c = 52.5 cm (external radius of canister) and an outer radius r_b = 87.5 cm (external radius of bentonite buffer). [r_b/r_c = 1.666, $r_b - r_c$ = 35 cm.].
Let us denote by ε porosity of bentonite. In the general case, ε is a function of the radial coordinate, r, and time, t. The corresponding mass balance equation is:

$$\frac{\partial \varepsilon C_{HS^-}}{\partial t} = \frac{1}{r}\frac{\partial}{\partial r} D^p_{HS^-} r \frac{\partial C_{HS^-}}{\partial r} - \varepsilon k_5 C_{HS^-} C_{O_2} - \varepsilon k_6 C_{HS^-} C_{H_2O_2} \qquad (16)$$

where, $D^p_{HS^-}$ is the diffusion coefficient of HS^- in the porous medium (bentonite), which can be presented in the form [10]:

$$D^p_{HS^-} = \frac{\varepsilon}{\tau^2} D_{HS^-} \qquad (17)$$

here D_{HS^-} is the bulk aqueous phase diffusion coefficient of HS^- ions in groundwater and τ is the tortuosity of the bentonite. In the case when the tortuosity of the

bentonite is not known, we will use the Bruggeman's approximation $\tau = \varepsilon^{-0.25}$ [11], i.e.:

$$D^{p}_{HS^-} = \varepsilon^{3/2} D_{HS^-} \qquad (18)$$

In the general case, when the pores of the bentonite are not fully filled with water, in all equations we have to use, instead of porosity, ε, the product εS, where S ($0 < S < 1$) is the saturation of liquid in the pores, i.e. the fraction of the pores filled with water. In the current report, we will assume that S = 1 (the most dangerous case, because it maximizes the supply of HS^- to the copper surface).
Initial and boundary conditions are:

$$C_{HS^-} = C^{b}_{HS^-} \quad \text{at } t = 0 \qquad (19)$$

and

$$C_{HS^-} = 0 \quad \text{at } r = r_c,$$
$$C_{HS^-} = C^{b}_{HS^-} \quad \text{at } r = r_b. \qquad (20)$$

where $C^{b}_{HS^-}$ is the concentration of HS^- ions in the bulk ground-water.

In Equation (16), the bulk terms describe only the sink of HS^- ions and, accordingly, these terms can only reduce the flux density of HS^- to the canister surface. Accordingly, the upper estimate of the flux density of HS^- will be obtained via the solution of the equation

$$\frac{\partial \varepsilon C_{HS^-}}{\partial t} = \frac{1}{r}\frac{\partial}{\partial r}\varepsilon^{3/2} D_{HS^-} r \frac{\partial C_{HS^-}}{\partial r} \qquad (21)$$

i.e. by solution Equation (16) without the chemical terms.
The linear Equation (21), with corresponding boundary and initial conditions, can be easily solved numerically assuming that the porosity, ε, the diffusion coefficient, D_{HS^-}, and bulk concentration of HS^- are arbitrary but known functions of the radial coordinate, r, and time. Thus, the diffusion coefficient, D_{HS^-}, is assumed to change only due to changes of temperature in the repository. However, for estimation purposes, we will assume that the diffusion coefficient D_{HS^-}, porosity, ε, and bulk concentration of HS^- ions in groundwater, $C^{b}_{HS^-}$ are constants.

It is convenient to introduce dimensionless variables:

$$R = \frac{r}{r_c},\ \tau = \frac{t}{t_0}, t_0 = \frac{r_c^2}{\varepsilon^{1/2} D_{HS^-}},\ \mathrm{C} = \frac{\mathrm{C}_{\mathrm{HS^-}}}{\mathrm{C}^{b}_{\mathrm{HS^-}}} \qquad (22)$$

In these variables our boundary problem has the form:

$$\frac{\partial C}{\partial \tau} = \frac{1}{R}\frac{\partial}{\partial R} R \frac{\partial C}{\partial R} \qquad (23)$$

$$C = 1 \quad \text{at } \tau = 0 \tag{24}$$

and

$$C = 0 \quad \text{at } R = R_c = 1, \quad C = 1 \quad \text{at } R = R_b = 1.666 \tag{25}$$

Analytical solution of this equation is:

$$C(R,\tau) = 1 + \frac{\ln(R)}{\ln(R_b)} + \sum_{n=1}^{\infty} A_n U_0(R\beta_n) e^{-\beta_n^2 t} \tag{26}$$

where

$$U_0(R\beta_n) = J_0(R\beta_n)Y_0(\beta_n R_b) - J_0(R_b\beta_n)Y_0(R\beta_n)$$

$$Y_\nu(z) = \frac{J_\nu(z)\cos(\nu\pi) - J_{-\nu}(z)}{\sin(\nu\pi)}$$

and

$$A_n = -\frac{\pi J_0(\beta_n) J_0(R_b\beta_n)}{J_0^2(\beta_n) - J_0^2(R_b\beta_n)}$$

$J_\nu(z)$ is the Bessel function of the first kind and β_n is the root of the equation

$$J_0(\beta_n)Y_0(R_b\beta_n) - J_0(R_b\beta_n)Y_0(\beta_n) = 0$$

Accordingly, the molar flux density of HS^- on the container surface, j_{HS^-}, is expressed as:

$$j_{HS^-} = -\varepsilon^{3/2} D_{HS^-} \left(\frac{\partial C_{HS^-}}{\partial r} \right)_{r=r_c} = -\frac{\varepsilon^{3/2} D_{HS^-} C^b_{HS^-}}{r_c} J \tag{27}$$

where

$$J(\tau) = \left(\frac{\partial C}{\partial R} \right)_{R=1} = \frac{1}{\ln(R_b)} + \sum_{n=1}^{\infty} A_n \left(\frac{dU_0(R\beta_n)}{dR} \right)_{R=1} e^{-\beta_n^2 \tau} \tag{28}$$

And

$$\left(\frac{dU_0(R\beta_n)}{dR} \right)_{R=1} = -\beta_n J_1(\beta_n) Y_0(\beta_n R_b) + \beta_n J_0(\beta_n R_b) Y_1(\beta_n)$$

In spite of the fact that the analytical solution of Boundary Problem (23)-(25) was obtained, it is much easier to perform practical calculations of the dimensionless flux density, *J(τ)*, by direct numerical solution of the corresponding system of equations.

Figure 2 shows the results of numerical calculation of absolute value of the dimensionless flux density of HS^- at the canister surface, $J = \left(\frac{\partial C}{\partial R} \right)_{R=1}$. Numerical

calculations were performed by using the finite difference method (fully implicit numerical scheme).

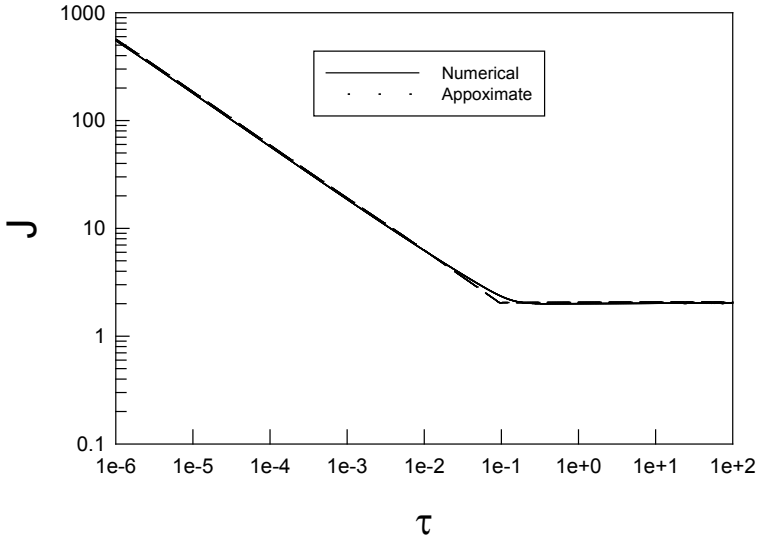

Figure 2. Absolute value of dimensionless flux density calculated numerically and by using approximate analytical Solution (31).

As we can see, the exact solution can be approximated by two asymptotes:

$$J_{tr} = \frac{1}{\sqrt{\pi\tau}} \tag{29}$$

which corresponds to non-stationary diffusion from semi-infinite space and

$$J_{st} = \frac{1}{\ln(R_b)} \tag{30}$$

which corresponds steady-state diffusion inside of a hollow cylinder. The approximate solution shown in Figure 2 corresponds to a combination of these two exponents:

$$J = J_{tr} \text{ at } J_{tr} \geq J_{st} \text{ and } J = J_{st} \text{ at } J_{tr} \leq J_{st} \tag{31}$$

Accordingly, the transient time to establish steady-state conditions, t_{tr}, can be estimated from the relation $J_{tr} = J_{st}$ or $\tau_{tr} = \frac{[\ln R_b]^2}{\pi}$. In our case, ($R_b$ = 1.666) we have $\tau_{tr} = 0.0829 \approx 0.1$, or for the dimension transient time, we have

$$t_{tr} \approx 0.1 \frac{r_c^2}{\varepsilon^{1/2} D_{HS^-}} \tag{32}$$

It is evident that the maximum possible flux density of copper dissolution, $j_{Cu,max}$ is

$$j_{Cu,\max} = n\left|j_{HS^-}\right| = \frac{n\varepsilon^{3/2} D_{HS^-} C^b_{HS^-}}{r_c} J \qquad (33)$$

where n is the number of electrons transferred in any copper dissolution reaction that involves HS^-. In all of our calculation, we will accept $n = 2$ [as follows for example from Reaction (9)].

Accordingly, for the maximum possible thickness of the corroded layer as a function of time we have

$$d_{\max}(t) = \frac{M_{Cu}}{\rho_{Cu}} \int_0^t j_{Cu,\max} dt = \frac{\varepsilon^{3/2} D^0_{HS^-} M_{Cu} C^b_{HS^-} t}{\rho_{Cu} r_c \ln(r_b / r_c)} + \frac{M_{Cu} \varepsilon r_c C^b_{HS^-}}{\rho_{Cu}} \sum_{n=1}^{\infty} \frac{A_n}{\beta_n^2} \left(\frac{dU_0(R\beta_{nc})}{dR} \right)_{R=1} [1 - e^{-\varepsilon^{1/2} D^0_{HS^-} \beta_n^2 t / r_c^2}] \qquad (34)$$

Here M_{Cu} = 63.546 g/mol is the atomic weight of copper and ρ_{Cu} = 8.96 g/cm^3 is the density of copper.

In order to estimate the maximum possible loss of metal thickness, we have to substitute into Equation (34) the maximum possible bulk concentration of HS^- ions and the maximum possible diffusion coefficient, D_{HS^-}.

In accordance with Table 1 the maximum value of $C^b_{HS^-}$ is 10^{-5} M = 10^{-8} mol/cm^3.

Table 1. Chemical composition of the groundwater at repository depth in the Forsmark-North Uppland area estimated within the SR-Can project [9].

Constituent		At closure	After resaturation (< 100y after closure)	10,000 years into the future
pH		**6–9**	**7.1–8.7**	**6.7–8.3**
Eh	**mV**	**0 to –280**	**–190 to –280**	**–150 to –260**
Na^+	mg/L	90–3,750	90–3,750	65–2,860
	M	$(4–163)\cdot10^{-3}$	$(4–163)\cdot10^{-3}$	$(3–124)\cdot10^{-3}$
K^+	mg/L	1–136	1 –136	6–104
	M	$(0.3–35)\cdot10^{-4}$	$(0.3–35)\cdot10^{-4}$	$(2–27)\cdot10^{-4}$
Ca^{2+}	mg/L	58–1,900	58–1,900	56–1,580
	M	$(1.4–47)\cdot10^{-3}$	$(1.4–47)\cdot10^{-3}$	$(1.4–39)\cdot10^{-3}$
Mg^{2+}	mg/L	0.1–460	0.1–460	12–345
	M	$(0.01–19)\cdot10^{-3}$	$(0.01–19)\cdot10^{-3}$	$(0.5–14)\cdot10^{-3}$
HCO^{3-}	mg/L	5–290	5–290	19–290
	M	$(0.1–4.8)\cdot10^{-3}$	$(0.1–4.8)\cdot10^{-3}$	$(0.3–5)\cdot10^{-3}$
Cl^-	**mg/L**	**95–6,900**	**95–6,900**	**16–5,500**
	M	**$(2.7–194)\cdot10^{-3}$**	**$(2.7–194)\cdot10^{-3}$**	**$(0.3–154)\cdot10^{-3}$**
SO_4^{2-}	mg/L	19–900	19–900	19–690
	M	$(0.2–9.4)\cdot10^{-3}$	$(0.2–9.4)\cdot10^{-3}$	$(0.2–7.2)\cdot10^{-3}$
HS^-	**mg/L**	**0–0.3**	**0–0.30**	**0–0.23**
	M	**$0–10^{-5}$**	**$0–10^{-5}$**	**$0–10^{-5}$**

In addition, Figure 3 yields predicted variation of temperature as a function of time near the canister surface.

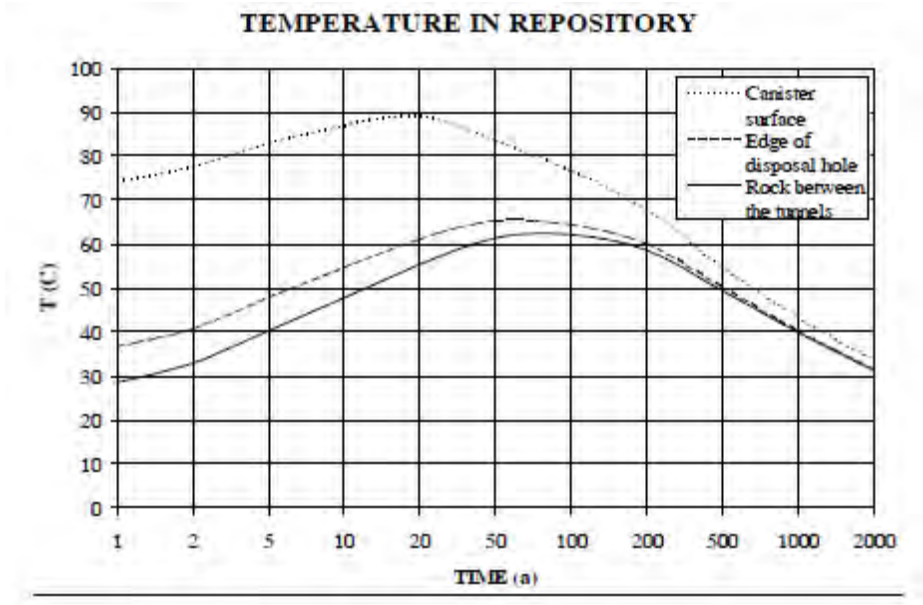

Figure 3. Predicted variation of temperature with time at the canister surface (r_c), edge of the disposal hole (r_b), and rock between the tunnels. After King et al. [9].

Figure 4 shows the diffusion coefficient of HS^- in dilute aqueous solutions as a function temperature. The calculations were made by using OLI's models and software [12].

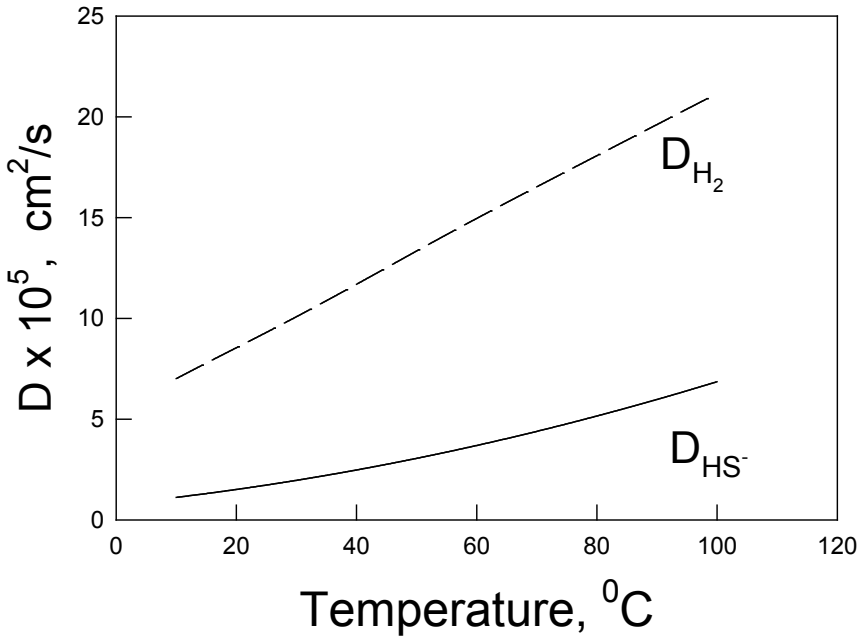

Figure 4. Diffusion coefficient of HS^- and H_2 in dilute aqueous solutions as a function of temperature.

As we can see, the maximum possible temperature in our system is 90^0C, which corresponds maximum possible value of diffusion coefficient $D_{HS^-} = 5.97 \times 10^{-5}$ cm^2/s.

Figure 5 yields maximum possible loss in thickness of the copper canister for different values of porosity of bentonite.

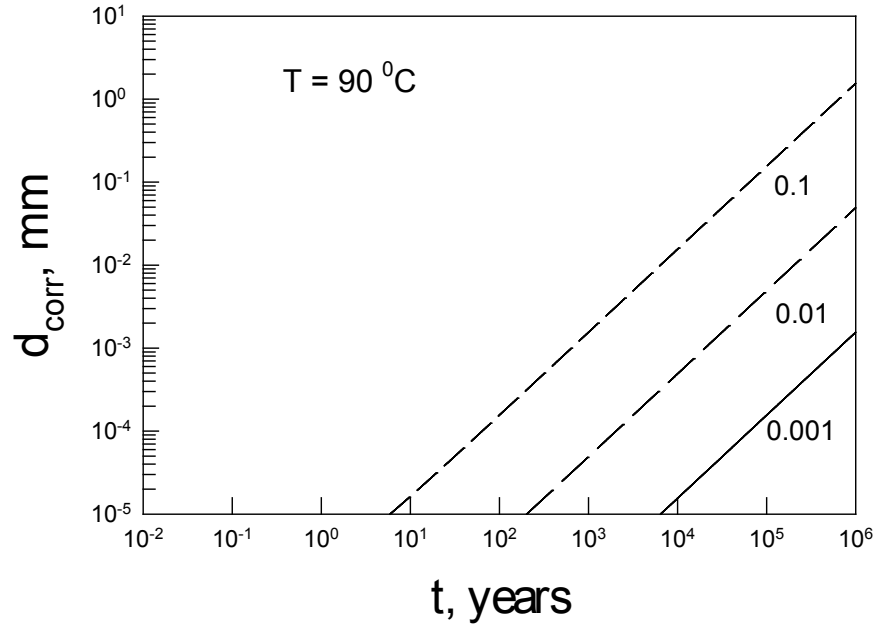

Figure 5. Maximum possible thickness of corroded layer as a function of time for different values of the porosity of bentonite.

The linear character of $d_{cort}(t)$ shows that only the steady-state of mass transfer [first term on the right side of Equation (34)] must be taken into account for estimating corrosion damage. Taking into account that the thickness of copper container is 5 cm we can conclude that general corrosion in not a threat to canister integrity in the repository even, for a period of time of 1 million years if, of course, the bentonite covers is not damaged and remains an effective engineered barrier.
Figure 6 shows the maximum possible corrosion current density at the copper canister, as given by

$$i_{corr} = -nFj_{HS^-} = \frac{n\varepsilon^{3/2} D_{HS^-} C^b_{HS^-}}{r_c} J \qquad (35)$$

The corrosion current density was calculated by assuming that the temperature of the system is 90 ^{0}C for different assumptions concerning the porosity of bentonite.

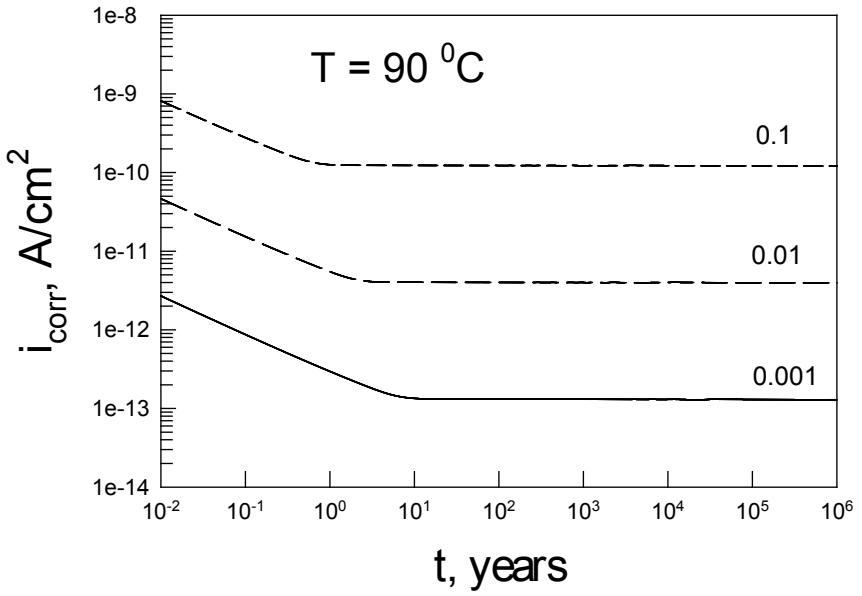

Figure 6. Maximum possible corrosion current density on the copper canister calculated by assuming that the temperature of the system is 90^0C for different values of the porosity of bentonite.

Below, for comparison purposes, Figure 7 and 8 show the results of numerical calculations [the results of direct numerical solution of Equation (21)] obtained for the case when the temperature on the copper canister, T_c, and on the outer surface of the bentonite hollow cylinder, T_b, change with time in accordance with data on Figure 3. Taking into account that thermal diffusivity of bentonite is higher by two orders of magnitude than the diffusion coefficient of HS^- we can assume that, at any moment in time, the temperature distribution corresponds to the steady-state distribution of temperature inside a hollow cylinder, i.e.:

$$T(r,t) = \frac{T_c \ln(r_b / r) + T_b \ln(r / r_c)}{\ln(r_b / r_c)} \qquad (36)$$

If the temperature distribution in bentonite is known we can calculate diffusion coefficient of HS^- by using the relation:

$$D_{HS^-} = D_0 e^{-\frac{E_D}{RT}} \qquad (37)$$

where $D_0 = 0.0172$ cm^2/s and $E_D = 17118$ J/mol (see Figure 4). As was noted above, numerical calculations were performed by using the finite difference method (a fully implicit numerical scheme).

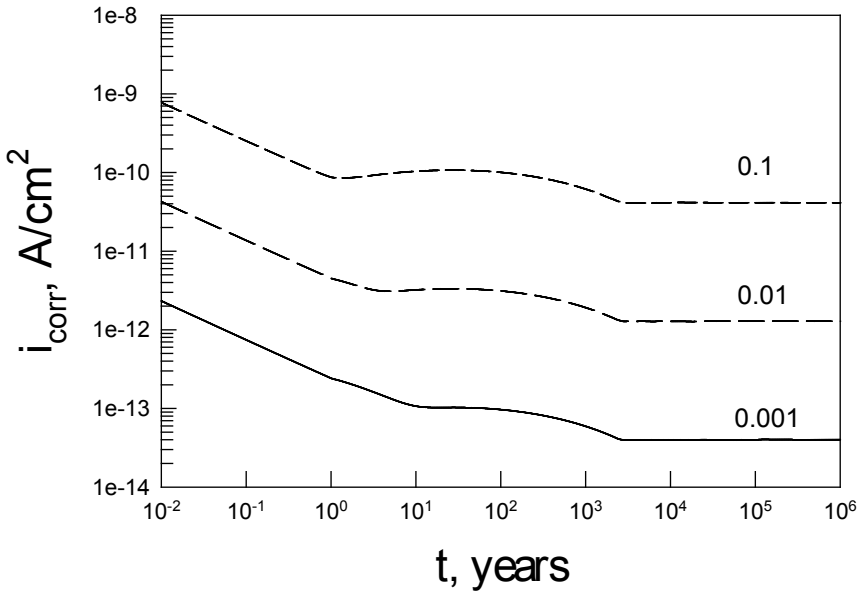

Figure 7. Corrosion current density at the copper canister as a function of time calculated for different values of the porosity of bentonite. The hump in the figure arises from the variation of the temperature of the canister surface (see Figure 3).

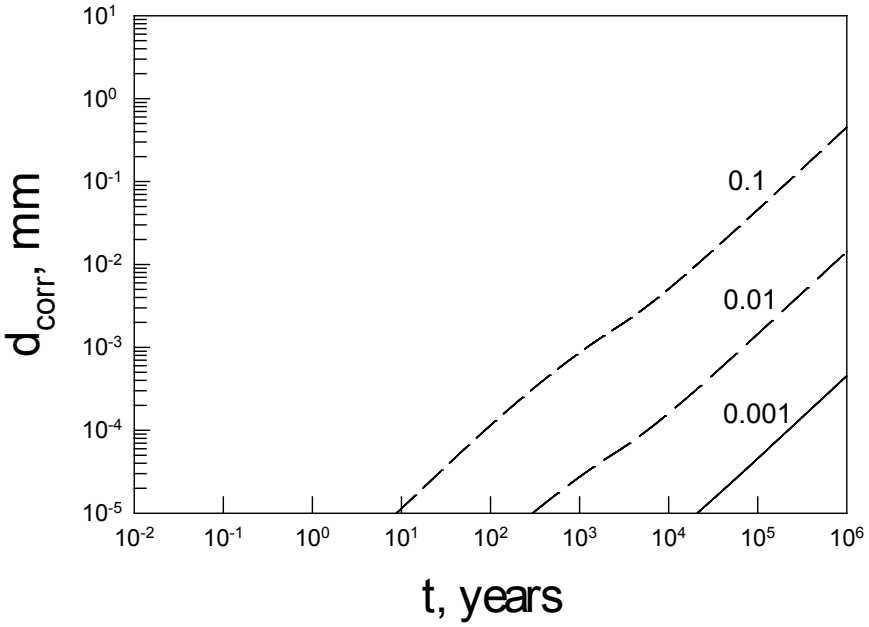

Figure 8. Thickness of corroded layer as a function of time for different values of the porosity of bentonite. The hump in the figure arises from the variation of the temperature of the canister surface (see Figure 3).

As we might expect, calculation of the corrosion current density and corrosion metal loss determined under "real" conditions (variable temperature as a function of coordinate and time) yield values that are lower than the maximum possible estimates of these values (see Figures 5 and 6). These calculations confirm once again our con-

clusion that general corrosion is not a threat to container integrity in the repository even for the period of time of 1 million year if bentonite cover will be not damaged.

3. Estimation of maximum possible value of corrosion potential

In a previous report [1], it was noted that, according to the criterion derived from the Second Law of Thermodynamics, which states that for a corrosion process to be viable $E_a^e < E_{corr} < E_c^e$; where E_a^e is the equilibrium potential of the partial anodic reaction [Reaction (9)] and E_c^e, is the equilibrium potential of the partial cathodic reaction [Reaction (2)]. We will try to reduce essentially the interval of possible changing of corrosion potential, $\Delta E_{corr} = E_{corr,max} - E_{corr,min}$ for our particular system.

Taking into account that cathodic current density, i_{cat}, is a decreasing function of applied potential we can conclude that in accordance with the Mixed Potential Model (MPM), the minimum possible values of corrosion potential, $E_{corr,min}$ can be estimated from the condition:

$$i_{cat}(E_{corr,\min}) = i_{corr,\max} \qquad (38)$$

where $i_{corr,max}$ is the maximum possible corrosion current density that can be observed at the canister surface in the repository. The last value is determined by the transport limitations of HS^- ions and it has been estimated in the previous part of the report.

In turn, the method of calculating $i_{cat}(E_{corr,\min})$ depends on the structure of the border of corroding surface and nonconductive bentonite (or more generally on the structure of outer boundary layer). It can be suggested the following structure (see Figure 9).

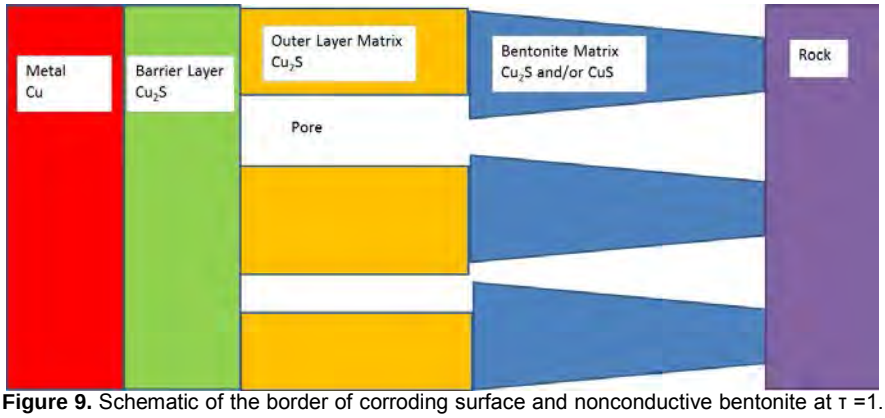

Figure 9. Schematic of the border of corroding surface and nonconductive bentonite at τ =1. It is assumed that in general case the porosity of the bentonite near outer layer/bentonite can be less than in the volume of bentonite due to the stress applied by the growing outer layer and a concomitant decrease in the porosity.

In Figure 9 we see the situation when the outer layer is still porous and is abutting the bentonite buffer, while this occurs, because the Pilling-Bedworth ratios of Cu_2S and CuS are 2.00 and 2.83, respectively (see below). Note that, at a sufficiently long time, the continued growth of the porous outer layer will result in the porosity be-

coming zero; thereby representing an additional barrier against the movement of HS^- to the canister surface. This concept that corrosion might be "self-limiting", because of compression of the outer layer, has been invoked by the authors in analyzing the corrosion of the carbon steel overpack in the supercontainer specified for the disposal of Belgian HLNW. If so, the limiting factor in the accumulation of corrosion damage to a copper canister in the Swedish KBS-3 plan may be the corrosion process itself.

Let us assume that the dependence $i_{cat}(E, C_{HS^-})$ is known for some fixed temperature and pH. Let us also denote $i^0_{\lim}$ is the limiting corrosion current density on the free surface (without any deposit) and E^0_{corr} is the corresponding corrosion potential.

It is suggested that the following algorithm of calculation be used for calculating the corrosion current density, i_{corr} and corrosion potential, E_{corr}, of the system. In the first step, we calculate the limiting current density without taking into account that the surface might be partially blocked by the existence of the solid (bentonite) matrix (i.e. at ε =1), $i^0_{\lim}$. The method of calculation has been described in the previous part of the report.

In the second step, we declare the anodic current density inside each pore to be $i_p = \varepsilon^{1/2} i^0_{\lim}$. The factor $\varepsilon^{1/2}$ appears, because, due to the tortuosity effective, the effective length of the pores increases in comparison with the geometrical thickness of the matrix (bentonite).

In the third step, we declare $i_{corr} = \varepsilon i_p = \varepsilon^{3/2} i^0_{\lim}$ as a general corrosion current density on the copper surface. Here, we assume that the active area of the surface $S_{act} = \varepsilon S$, where S is the geometric area of the metal surface and ε is the porosity.

In the fourth step, we calculate the copper corrosion potential inside the pore, $E_{p,corr}$ as a solution of the equation

$$i_{cat}(E_{p,corr}, 0) = i_p = \varepsilon^{1/2} i^0_{\lim} \tag{39}$$

Here, we assume that the mixed potential model (MPM) is applicable inside each pore and that the dependence $i_{cat}(E, C_{HS^-})$ is known.

In the fifth step, assuming that, because of the very high conductivity of the metal, the whole metal surface must have the same potential (under both open pores and under blocked regions, as well). We declare $E_{p,corr}$ equals to the corrosion potential of the copper, i.e.:

$$E_{corr} = E_{p,corr} \tag{40}$$

In Ref. 1, it was shown that the rate of cathodic Reaction (2) can be accurately described by classical Tafel equation:

$$i_{cat} = i_0 \exp\left(-\frac{\alpha n F \eta}{RT}\right) \tag{41}$$

where

$$\alpha = -0.069 + 6.81\times10^{-4}T \quad (42)$$

is the symmetry factor, and

$$i_0 = 0.2e^{-\frac{31268.9}{RT}}[H_2]^{0.31}[H^+]^{-0.13} \quad (43)$$

is the exchange current density, and n = 2 is the number of electrons transferred in the metal electro-dissolution reaction. In Equation (43), i_0 is expressed in A/cm^2 when concentration $[H_2]$ and $[H^+]$ are expressed in m or M (solutions are dilute).
In order to estimate the value of exchange current density, i_0, we must estimate the concentration of dissolved H_2 near the copper surface. This can be done by solving transport equations for hydrogen inside the bentonite pores:

$$\frac{\partial C_{H_2}}{\partial t} = \frac{1}{r}\frac{\partial}{\partial r}\varepsilon^{1/2}D_{H_2}r\frac{\partial C_{H_2}}{\partial r} \quad (44)$$

with corresponding initial and boundary conditions:

$$C_{H_2} = C^b_{H_2} \quad \text{at t = 0} \quad (45)$$

and

$$-D_{H_2}\frac{\partial C_{H_2}}{\partial r} = D_{HS^-}\frac{\partial C_{HS^-}}{\partial r} \quad \text{at r = } r_c,$$
$$C_{H_2} = C^b_{H_2} \quad \text{at r = } r_b \quad (46)$$

where $C^b_{H_2}$ is the concentration of HS^- ions in the groundwater. The value of $C^b_{H_2}$ is estimated by using Henry's law:

$$C_{H_2} = p_{H_2}/k_{H_2} \quad (47)$$

where Henry's constant, k_{H_2}, can be expressed as:

$$k_{H_2} = k_{H_2}(T_0)\exp\left[-\gamma\left(\frac{1}{T}-\frac{1}{T_0}\right)\right] \quad (48)$$

and T_0 = 298.15 K, $k_{H_2}(T_0)$ = 1282.05 L atm/mol, and γ = 500 K. It was assumed that the partial pressure of hydrogen in the repository, p_{H_2} is 7x10^{-9} bar.
The boundary condition at $r = r_c$ reflects the fact that, in accordance with Equations (2) and (9), the molecular flux densities of HS^- and H_2 have equal absolute values, but occur in opposite directions. Mass transport problems for HS^- and H_2 species must be solved simultaneously. However, it is possible to separate these problems,

because the transport of HS^- species does not depend on transport of H_2 species under limiting current conditions. Practically, at each time step, we initially solve the mass balance equation for HS^- ions. Then, after calculating flux density of HS^- on the copper surface, we solve the mass balance equation for H_2 with the stated boundary conditions. Figure 4 yields the diffusion coefficient of the HS^- and H_2 species in dilute aqueous solutions as a function of temperature. Prediction of the diffusivities were made by using OLI's models and software [12].
Figure 10 yields concentrations of dissolved hydrogen molecules near surface of the copper canister calculated for different values of the bentonite porosity.

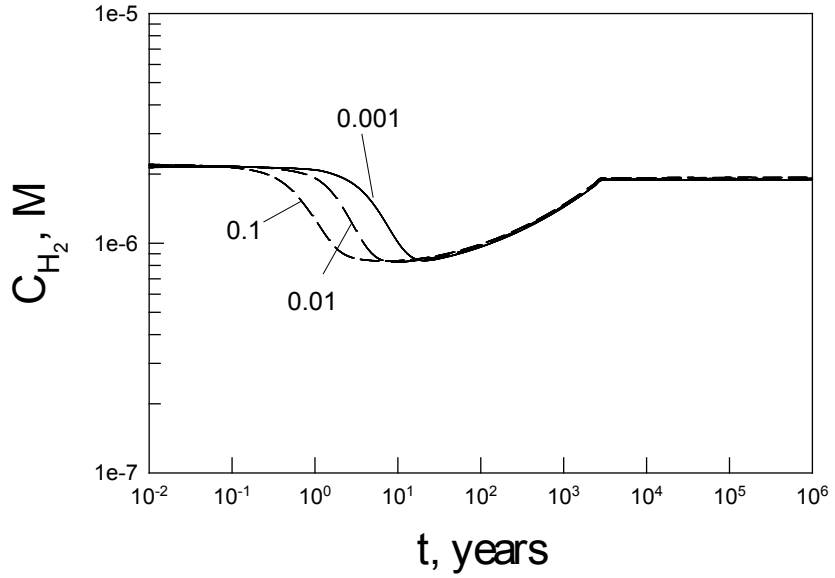

Figure 10. Concentrations of dissolved hydrogen near the surface of the copper canister as a function of time for different values of the bentonite porosity.

Now we are able to estimate the exchange current density from Reaction (2) by using Equation (43) (see Figure 11).

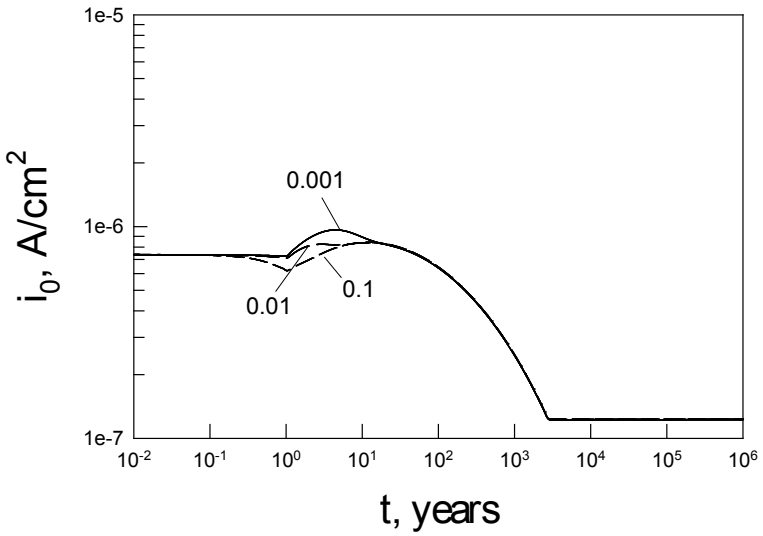

Figure 11. Exchange current density for Reaction (2) as a function of time for different values of the bentonite porosity and for pH = 8.

Due to the fact that the corrosion current density is very low, even inside the pores, it seems reasonable to assume that corrosion potential is near the equilibrium potential of the hydrogen electrode reaction.
Thus, as is well known, for η << RT/F (near equilibrium), the current density corresponding an electrochemical reaction, *i*, can be described by the linear relation

$$i \approx i_0 \frac{F\eta}{RT} \tag{49}$$

or

$$\eta \approx \frac{RT}{F}\frac{i_p}{i_0} = \frac{RT}{F}\frac{(i_{corr}/\varepsilon)}{i_0} \tag{50}$$

Here, we took into account that, in accordance with MPM, the current density of the cathodic reaction inside any pore must be equal to the corrosion current density inside the same pore.
Figure 12 displays the overpotential of Reaction (2) for different values of the bentonite porosity. In accordance with Figure 9, we will substitute into Equation (50) $i_p = i_{corr}/\varepsilon$, where can i_{corr} be found from Figure 7.

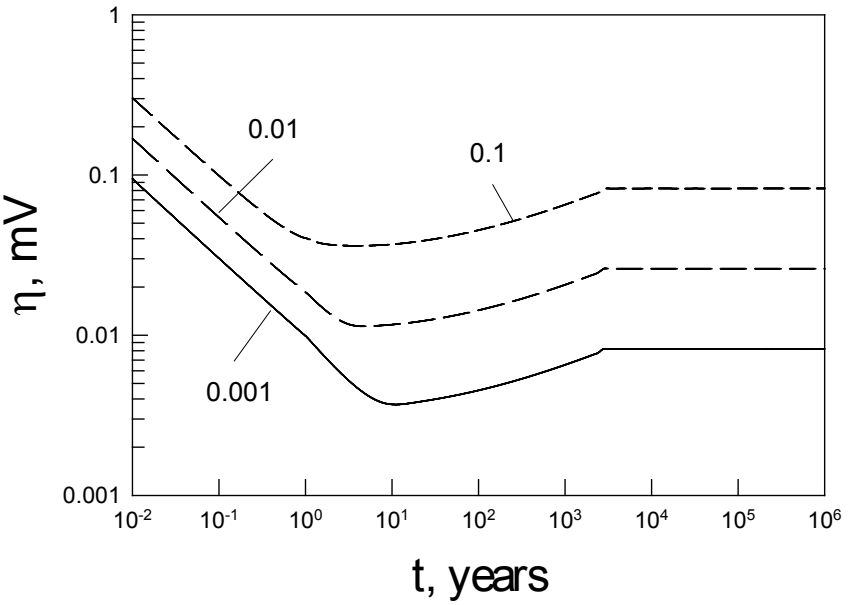

Figure 12. Overpotential of Reaction (2) as a functions of time for different values of the bentonite porosity and for pH = 8.

As we can see, the overpotential of Reaction (2) is really negligible. Consequently, calculation of the equilibrium potential of the hydrogen electrode reaction, E_c^e, (which we show above to be practically coincidental with the corrosion potential of the copper canister in contact with bentonite) can be made by using the Nernst's equation:

$$E_c^e = E_c^0 - \frac{RT}{2F}\ln\left(p_{H_2} a_{OH^-}^2\right) \qquad (51)$$

where E_c^0 is the standard equilibrium potential of Reaction (2). However, it is more comfortable, in our case, to calculate the equilibrium potential of Reaction (2) by using the circumstance that Reaction (2) is thermodynamically equivalent to the reaction of the hydrogen electrode:

$$2H^+ + 2e^- \leftrightarrow H_2 \qquad (52)$$

because, we can omit the calculation of E_c^0, which by definition equals zero at any temperature. Accordingly, we have

$$E_c^e = \frac{RT}{2F}\ln\left(a_{H^+}^2 / p_{H_2}\right) = -\frac{2.303RT}{F}pH - \frac{2.303RT}{2F}\log p_{H_2} \qquad (53)$$

where T is expressed in K and p_{H_2} in atm. The results of the calculations are shown in Figure 13.

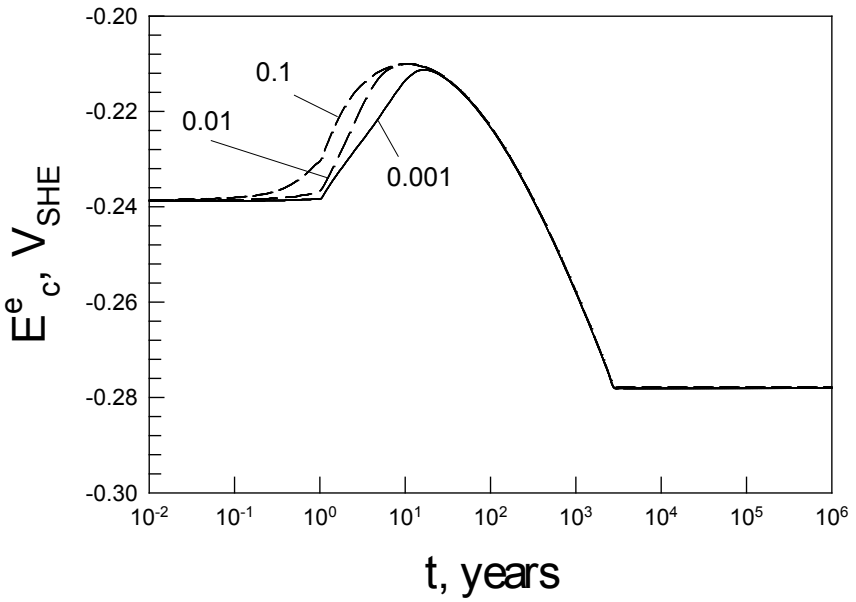

Figure 13. Equilibrium potential of the hydrogen electrode reaction as a function of time for different values of the bentonite porosity for pH = 8. As it was previously shown, this value practically coincides with the corrosion potential of the copper canister in the repository.

Finally, we investigate the situation that might exist in the event of fracture of the bentonite layer resulting in groundwater reaching the surface of the copper container. However, this scenario is only valid if the bentonite buffer were an unconstrained cylinder, when, in fact, the outer surface of the buffer is constrained by the rock wall. Additionally, as the bentonite hydrates, the bentonite swells placing the buffer and the copper canister under compression, which further impedes the transport of HS^- to the canister surface. This, coupled with compression of the outer layer of the passive film, is postulated to cause the cessation of corrosion, thereby

ensuring that the copper canister will survive the planned storage period of 100,000 years. It is important to note that this conclusion applies strictly to general corrosion of the canister; it does not consider localized corrosion processes, such as pitting corrosion. The pitting factor (ratio of the depth of the deepest pit to the general corrosion loss) for metals range from 2 to >100 and is currently unknown for copper in the repository environment. If the pitting factor would be equal to 10, then the effective wall thickness of the canister would be reduced from 50 mm to 5 mm, as far as wall penetration is concerned. However, the growth of pits will also be inhibited by compression of the outer layer as well, because the pits require a continual supply of either HS^- or H_2O to remain active. Stress corrosion cracking can probably be discounted, because the canister is expected to be under compression after buffer hydration.

In the highly unlikely event that the copper canisters were exposed directly to the groundwater the experimental data obtained in this study indicate that the passive (partial anodic) current density of copper dissolution as a function of $[HS^-]$ can be approximated by the following equation:

$$i_p = Ae^{-E_p/RT}[Na_2S]^{\alpha}\exp\left(\frac{2\alpha_p F\eta}{RT}\right) \tag{54}$$

where A = 1.72×10^4 A/cm^2, E_p = 29305 J/mol, α_p = –0.0645 + 0.00334×T_c – 3.41×10^{-6}×T_c^2, (T_c is the temperature expressed in ^{0}C), α=1.23, and $\eta = E - E_a^e$ is the overpotential of Reaction (9). Potential, E, as reported above, approximately equals equilibrium potential of Reaction (2) (see Figure 14) and the equilibrium potential of Reaction (9) can be calculated as:

$$E_a^e = E_a^0 - \frac{2.303RT}{2F}pH - \frac{2.303RT}{2F}\log a_{HS^-} \tag{55}$$

The standard equilibrium potential of Reaction (9), E_a^0 as a function of temperature can be found in previous reports [1]. Calculations show that for T = 90 ^{0}C and pH = 9, the corrosion current density equals 5.07×10^{-7} A/cm^2 (i.e. the corrosion rate is 5.89 μm/year). It means that the wall of the canister with the thickness of 5 cm would be penetrated within about 8500 years. The analogous calculations performed at T = 25 ^{0}C and pH = 9 yield 8.95×10^{-8} A/cm^2 (i.e. the corrosion rate is 1.04 μm/y) and canister with the thickness of 5 cm will be penetrated within about 48,000 years.

However, these calculations assume that the HS^-/H_2O being transported through the buffer to the canister surface is unimpeded by the bentonite buffer and by compression of the passive film that is formed at the interface against the buffer. Furthermore, no account is taken of the decrease in the porosity of the bentonite buffer as the buffer hydrates and ages. As shown below (Figure 16), the porosity of the outer layer of the passive film is a sensitive function of the initial porosity and the thickness of the corroded copper, which is converted into Cu_2S, having a Pilling-Bedworth ratio (PBR) of 2. The PBR is defined as the volume of the corrosion product produced divided by the volume of the metal consumed to form that product. PBR = 2 means that the Cu_2S formed occupies twice the volume of the metal that it replaces. Because the corrosion product is formed in a volume that is constrained by the inner surface of the buffer and the outer surface of the canister, it will become compressed and the porosity will decrease as corrosion proceeds. Eventually, the porosity is expected to be reduced to zero and corrosion ceases. Thus, from

Figure 16 (see below), we estimate that, for an initial porosity of the outer layer of the passive film of 1 %, the outer layer will become impervious after the loss of about 4 mm of copper. Accordingly, the 50,000 year time for the complete corrosion of the copper canister estimated above is considered to be not representative of the actual life of the canister and is surely low by several orders of magnitude. On this basis, we expect that the copper canister will survive until the storage horizon of 100,000 years and perhaps much longer.

Taniguchi and Kawasaki [13] have studied the influence of sulphide concentration on the corrosion behavior of pure copper in synthetic seawater. They performed immersion tests in simple saline solutions and bentonite-sand mixtures in saline solutions to simulate buffer material. They calculated the average corrosion depth from the mass losses of the coupons as a function of time, which was approximated by a linear equation using the least squares method. Surprisingly, they reported no corrosion in solutions containing 0.001M Na_2S at 80°C, which is not in agreement with reported corrosion rates by other researchers. For example, Chen et al. and Smith and co-workers [8,14,15] studied the corrosion behavior of oxygen-free copper in an anoxic 0.1 M $NaCl$ + 10^{-5} to 10^{-3} M Na_2S solution using electrochemical impedance spectroscopy, scanning electron microscopy equipped with a focused ion beam, X-ray photoelectron spectroscopy, and micro X-ray diffraction. As we can see in Table 2, they observed corrosion of copper in solutions containing sulphide ion as low as 10^{-5} M. On the other hand, Rosborg et al. [16] also studied the corrosion of copper in an oxic bentonite/saline groundwater environment and their EIS measurements revealed a corrosion rate of 0.4-0.7 μm/year after three years of exposure. On the contrary, the calculated corrosion rate in this study, is somewhat higher than those reported at ambient temperature by other researchers. However, the values calculated in this work can be regarded as initial corrosion rates for bare metal, because of the short duration of the experiments (typically less than one hour) and it is expected that the corrosion rate will decrease significantly as the passive film develops on the surface [13]. This is so, because one of the important factors controlling the corrosion rate is the formation of a corrosion product film, since it represents a barrier to the transport of reactant (HS^-) to and corrosion product (Cu^+) from the metal surface. Lower corrosion rates than those calculated in this study, are assumed to be due to the occurrence of more protective corrosion product films on the metal surface, due to longer exposure times.

Table 2. Summary of the corrosion rate measurements in various studies.

[Na_2S], M	Corrosion rate (μm/year)	Temperature	pH	Reference
0	0 (solution) - 0.088 (bentonite)	80 °C	7.9-8.4	Taniguchi et al. [13]
0.001	0 (solution) - 0.55 (bentonite)	80 °C	7.9-8.4	Taniguchi et al. [13]
0.005	3.8 (solution) - 2.2 (bentonite)	80 °C	7.9-8.4	Taniguchi et al. [13]
0.1	9.7 (solution) - 15 (bentonite)	80 °C	7.9-8.4	Taniguchi et al. [13]
5×10^{-4}	3.6	22 ± 2°C	9.96	Chen et al. [14]
5×10^{-5}	0.5	22 ± 2°C	8.2	Chen et al. [6]
5×10^{-6}	0.4-0.7 (oxic bentonite/saline groundwater)	25 °C	6.9±0.1	Rosborg et al.[16]
10^{-5}	5.89	90 °C	9	This work
10^{-5}	1.04	25 °C	9	This work

4. Corrosion of copper in the confined space between the canister and the bentonite

In Ref. 13, the case of the corrosion of iron in physically constrained locations was explored. In particular, a model was developed to calculate the impact of compression of the porous outer layer of the passive film on the corrosion rate of the carbon steel overpack and on the structural integrity of the concrete in the annulus of the super container of the Belgian High Level Nuclear Waste (HLNW) disposal concept. Because the corrosion product occupies 2 – 6.5 times the volume of the iron from which it forms (i.e., the Pilling-Bedworth ratio), the development of the outer layer in the confined space between the carbon steel overpack and the concrete will result in the compression of the outer layer and a concomitant decrease in the porosity and will subject the ID surface of the concrete to a tensile hoop stress. If the porosity decreases to a sufficiently low value, the growth of the outer layer ceases and further corrosion is prevented. If the thickness of the corroded layer exceeds a critical value, the concrete will crack, because of the poor tensile strength of cementations materials under tensile loading. Accordingly, it becomes of interest to check if these same effects can play a significant role in the case of the corrosion of copper in the confined space between the canister and the bentonite buffer in the proposed Swedish High Level Nuclear Waste Repository.

As a first step, we estimate the Pilling-Bedworth ratio of the copper corrosion products. In this case, the outer layer has been identified as comprising Cu_2S or CuS or some mixture of copper sulphides and the barrier layer is exclusively Cu_2S. By definition, the Pilling-Bedworth ratio, η, of the outer layer can be calculated as:

$$\eta_{CuS} = \frac{M_{CuS}\rho_{Cu}}{\rho_{CuS}M_{Cu}} \approx 2.83 \qquad \text{and} \qquad \eta_{Cu_2S} = \frac{M_{Cu_2S}\rho_{Cu}}{\rho_{Cu_2S}M_{Cu}} \approx 2.00$$

(see also Figure 15). Here, M and ρ are the molecular weight and the density of the compounds. A comparison of the Pilling-Bedworth ratios of Cu_2S and CuS is presented in Figure 14.

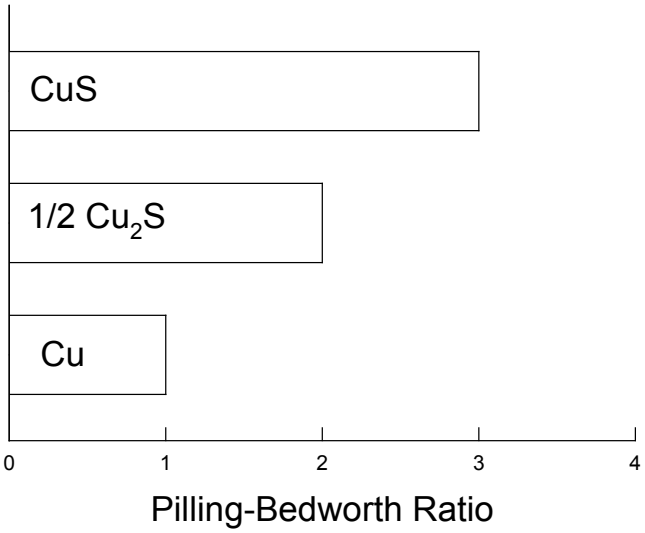

Figure 14. The relative volumes of copper and its corrosion products (Pilling-Bedworth ratio, η).

In accordance with the results of Ref. 13, we have the following estimates for the radial, σ_r, and tangential (hoop) stress, σ_θ, applied at the interface between the outer layer and the bentonite that exists due to the growth of outer layer as a result of corrosion and its impingement upon the bentonite:

$$\sigma_{\mathrm{r}} = -\frac{E_b[r_c^2(1+\nu_b)+r_b^2(1-\nu_b)]}{(r_b^2-r_c^2)(1-\nu_v^2)r_c}(\eta-1)d_{corr} \qquad (56)$$

and

$$\sigma_\theta = -\frac{E_b[r_c^2(1+\nu_b)-r_b^2(1-\nu_b)]}{(r_b^2-r_c^2)(1-\nu_v^{2\,2})r_c}(\eta-1)d_{corr} \qquad (57)$$

where E_b is Young's modulus and ν_b is Poisson's ratio of the bentonite, respectively. Because, values for Young's modulus and Poisson's ratio for bentonite are not known, the present analysis yields only "model estimates" of the expansive pressure, $p_c = -\sigma_r$ at the interface between the outer layer and the bentonite as a function of the thickness of corroded layer that were made by assuming the corresponding values for concrete, namely at E_b = 45 GPa and ν_b = 0.23 [17].

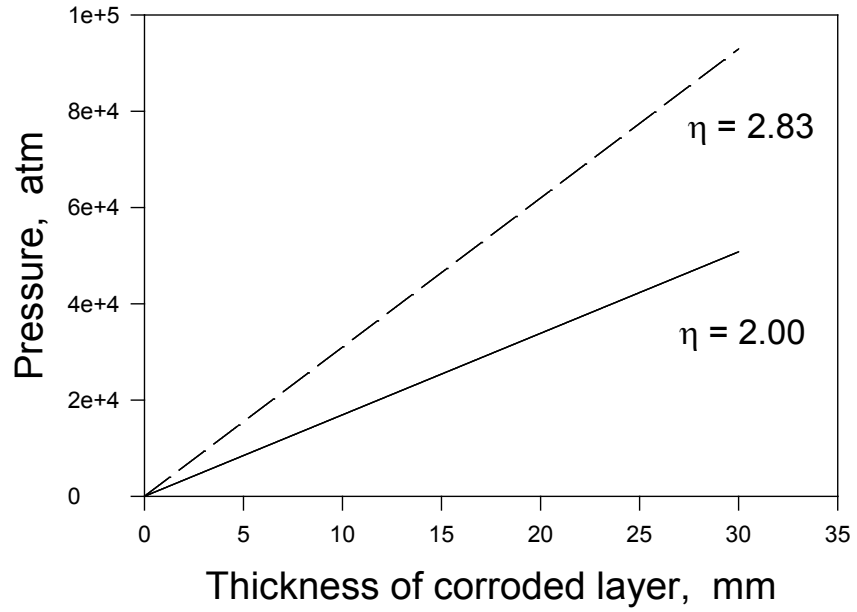

Figure 15. Pressure, $p_c = -\sigma_r$, that the outer layer exerts on the bentonite as a function of the thickness of corroded layer (loss of metal) for Cu_2S (η = 2) and CuS (η = 2.83).

In Ref. 13, it was also shown that the expansive pressure at the outer layer/bentonite interface leads (in accordance with Hook's law) to the applied volumetric strain of the thin outer as:

$$\varepsilon_T = \frac{p_c}{E_c}(1-2\nu_c) \tag{58}$$

where, E_c is Young's modulus and ν_c is Poisson's ratio of the outer layer (patina). In turn, if the resulting strain is small, the following dependence of the porosity of the outer layer on the strain is obtained:

$$\phi = \frac{\phi_0 - \alpha\varepsilon_T}{1-\varepsilon_T} \tag{59}$$

where ϕ_0 is the porosity of the outer layer at the reference state, e.g. at normal pressure (1 atm.) and α is the Biot-Willis coefficient (which describes the compressibility of the solid matrix) [18].

Figure 16 displays the variation of porosity of the outer layer as a function of the thickness of the corroded layer of the canister. Calculations were made assuming that E_b = 45 GPa, ν_b = 0.23, η = 2 (outer layer of Cu_2S) and α = 1 (Biot-Willis coefficient of the solid matrix of the outer layer of zero porosity, which is assumed to be non-compressible).

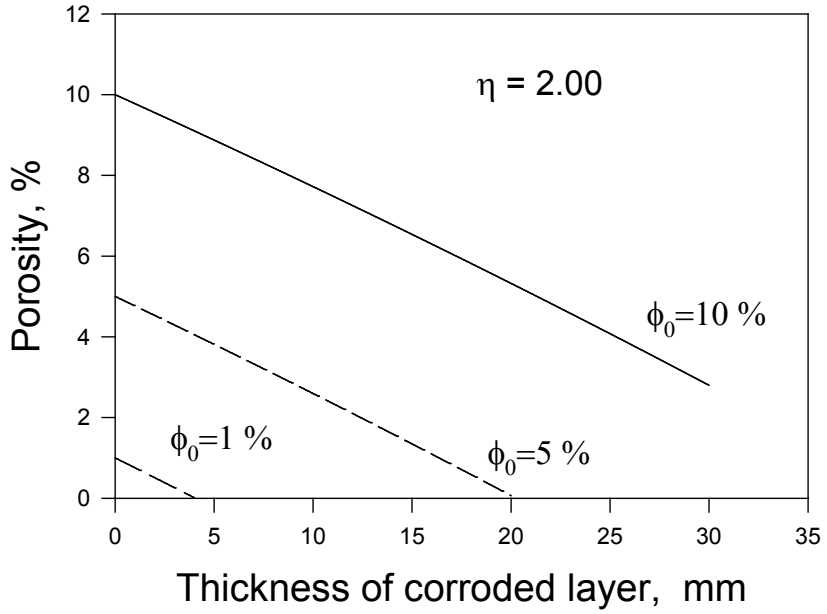

Figure 16. Porosity of the outer layer as a function of the thickness of corroded layer for different initial values of the outer layer porosity.

As we can see, for ϕ_0 = 10 %, the pores of the outer layer will not be closed before the canister will be consumed by general corrosion (the thickness of canister is 50 mm). However, for ϕ_0 = 5 %, it is predicted that general corrosion will stop (pores will be closed) when the thickness of corroded layer is around 20 mm, and at ϕ_0 = 1 % corrosion damage will be less than 5 mm before corrosion is stifled. These examples show that, in principle, the canister may be protected by the reduction of porosity of the outer layer by compression caused by the growing corrosion product layer impinging upon the canister. In other words, corrosion damage to the

canister is predicted to be self-limiting, a conclusion that was previously unknown, but one that is obviously important in repository engineering.

However, it is important to note that, if the tangential (hoop) stress on the outer layer/bentonite interface, σ_0, exceeds the tensile strength on the bentonite, f_t, cracking of the bentonite may occur. Let us introduce the critical width of corroded layer, d_{cr}, by the condition that $d_{corr} > d_{cr}$ at $\sigma_\theta > f_t$. As we can see in Figure 17, in this case, d_{cr} is of the order of 0.04 mm, which is much less than the thickness of the canister. It is not clear if such cracking will really occur and what the consequences will be, in this case. Thus, in principle, such cracking can lead to the appearance of "shortcuts" between the canister and the rock, but a full analysis of this problem requires a finite element analysis of the stress distribution subjected to a constrained outer boundary of the buffer, so that the hoop and radial components of the stress can be fully resolved as the cracks grow through the buffer.

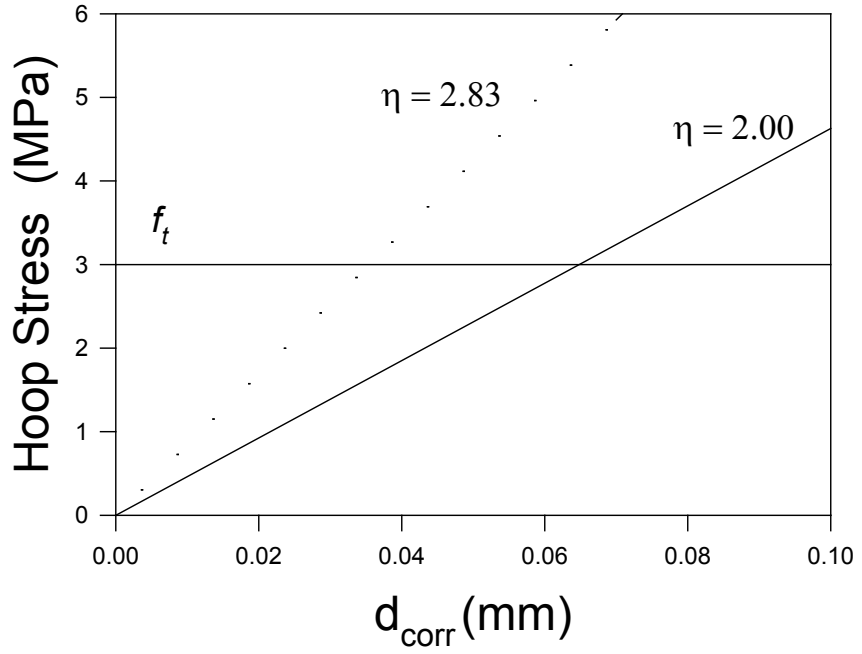

Figure 17. The tangential (hoop) stress at the interface between the outer layer and bentonite as a function of the thickness of corroded layer of *Cu* for the formation of Cu_2S (η = 2) and *CuS* (η = 2.83). For comparison purpose, a typical value of the tensile strength of concrete, f_t = 3 MPa, is shown.

We would like to mention that another mechanical criterion has been used in Ref. 13 for estimating the probability of concrete cracking. Namely, it was assumed that the critical width of corroded layer, d_{cr}, can be found by the condition that $d_{corr} > d_{cr}$ at $p_c = -\sigma_r > f_c$., where f_c is the compressive strength of bentonite. Figure 18 illustrates this criterion.

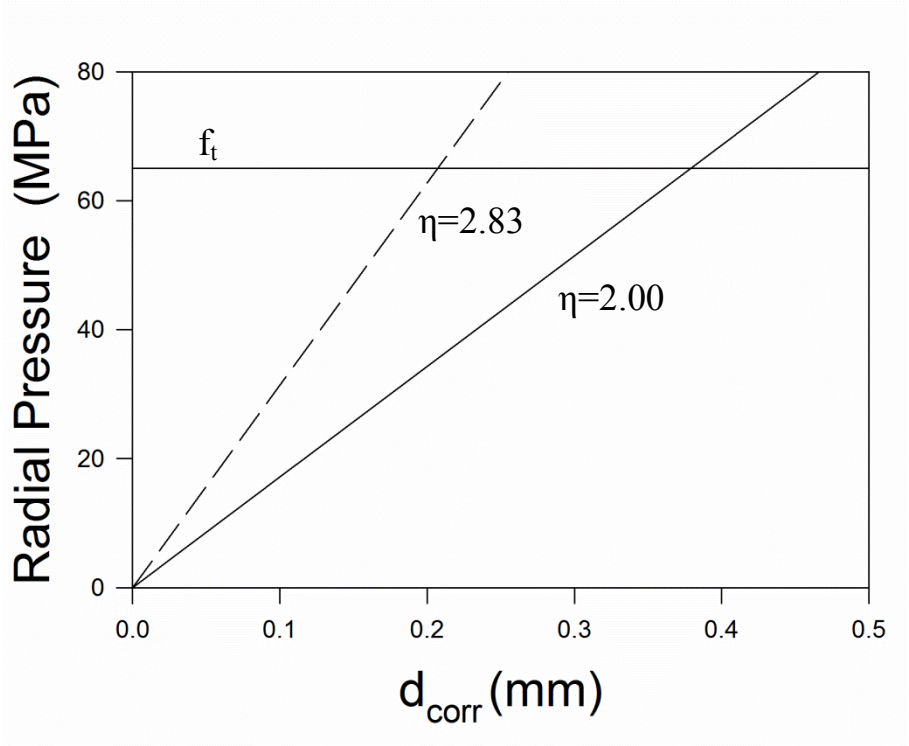

Figure 18. The radial pressure, $p_c = -\sigma_r$, at the interface between the outer layer and bentonite as a function of the thickness of corroded layer of *Cu* for the formation of Cu_2S (η = 2) and *CuS* (η = 2.83). For comparison purpose a typical value of compressive strength for concrete, f_t = 65 MPa is shown.

As we can see the criteria connected with the tensile stress is more conservative than the criteria connected with the compressive stress and, accordingly, the tensile stress criterion must be used for estimating the probability of cracking.

It is important to note that all analyses that have been performed above can be considered as to being only "model" in nature, because we have no experimental data for the elastic properties and initial porosity of the bentonite buffer and the outer layer. It is our opinion that it is important to perform the appropriate measurements and repeat all of the analyses using real data.

5. Summary and Conclusions

1. In the case when the bentonite buffer between the copper canister and the granitic rock is not damaged, we can neglect the possibility of general corrosion damage being a threat to canister integrity over a 100,000 year storage period. However, if the bentonite buffer is destroyed for any reason, and does not act as an engineered barrier, we predict that the ready access of sulphide species to the canister surface will degrade the canister within the period of 8,500 to 48,000 years, depending upon the temperature.
2. Due to the fact that the corrosion current density is very low, even inside pores in the bentonite buffer, it appears reasonable to use as an upper estimate of the corrosion potential, E_{corr}, the thermodynamically-determined

values of the equilibrium potential of the hydrogen electrode reaction [Reaction (2)], E_c^e. This estimate will not be over-conservative. For the most probable scenarios of the corrosion process, the error will be less than 1 mV.

3. It will be worth comparing E_c^e with the critical potentials for various localized corrosion processes, such as pitting corrosion, stress corrosion cracking, and crevice corrosion, in order to indicate whether any of these localized corrosion processes are likely to occur in the repository. Of course, in order to perform such comparison, the corresponding models for estimating the critical potentials for the localized corrosion processes must be developed along with the respective experimental investigations or the critical potentials must be measured directly.
4. Model predictions show that, in principle, the canister can be protected by the reduction of porosity of the outer layer of the passive film by compression caused by impingement of the growing corrosion product layer against the buffer. Model calculations show also that the tangential (hoop) stress on the outer layer/bentonite interface can become greater than the tensile strength of the bentonite and cracking of the bentonite may occur. Such cracking can cause, for example, the appearance of "shortcuts" between the canister and the rock, which might lead to accelerated corrosion. However, all estimates that were performed can be considered as being only "model" in nature, because we have no experimental data on the elastic properties and initial porosity of bentonite and outer layer of the passive film in this system. In our opinion, it is important to measure the required data and repeat all predictions using real mechanical data, because of the evident importance of passive layer and near-field buffer compression.
5. The most important finding of this analysis is that general corrosion of the copper canister may be self-limiting, because of the compression of the outer layer of the passive film and the near-field buffer, resulting in the porosity of one or both phases going to zero and thereby denying access of water and sulphide ion to the canister surface, which is required for continued corrosion.

6. References

1. D.D. Macdonald, S. Sharifiasl and Y. Ling, "Issues of the Corrosion of Copper in a Swedish High Level Nuclear Waste Repository", Stockholm, Sweden, 2011, 2012. Phase II and III.
2. D. D. Macdonald and S. Sharifiasl, "Is Copper Immune When in Contact With Water and Aqueous Solutions", TR 2011: 09, SSM, Stockholm, Sweden, 2011, Phase I report
3. J. Smith, Z. Qin, F. King, L. Werme, and D. W. Shoesmith, "The electrochemistry of copper in aqueous sulphide solutions", *Scientific Basis for Nuclear Waste Management XXIX. Symposium (Materials Research Society Symposium Proceedings Vol.932)*, p 869-75, 2006
4. J. Chen, Z. Qin, and D. W. and Shoesmith, "Rate controlling reactions for copper corrosion in anaerobic aqueous sulphide solutions", *Corrosion Engineering Science and Technology*, 46(2), 138-141 (2011).
5. J. Smith, Z. Qin, D. W. Shoesmith, F. King, and L. Werme, "Source: Corrosion of copper nuclear waste containers in aqueous sulphide solutions",

Scientific Basis for Nuclear Waste Management XXVII (Materials Research Society Symposium Proceedings Vol.824), p 45-50, (2004).
6. J. Chen, Z. Qin, and D. W. Shoesmith, "Long-term corrosion of copper in a dilute anaerobic sulphide solution"**,** *Electrochim. Acta*, **56**(23), 7854-7861 (2011).
7. F. King, L. Ahonen, C. Taxén, U. Vuorinen, L. Werme, **"**Copper corrosion under expected conditions in a deep geologic repository", Swedish Nuclear Fuel and Waste Management Co., Report, Technical Report, SKB TR-01-23 (2001).
8. F. King, Swedish Nuclear Fuel and Waste Management Co. Technical Report, TR-02-25 (2002).
9. F. King, C. Lilja, K. Pedersen, P.Pitkänen and P. Posiva*, SKB-TR-10-67, Svensk Kärnbränslehantering AB,* (2010).
10. J. Newman and K.Thomas-Alyea, Electrochemical Systems, 3rd ed.; Prentice Hall: Englewood Cliffs,NJ, 2004.
11. D. Bruggeman. *Annalen der Physik*, ser. 5, **24**, 636-664 (1935).
12. olisystems.com.
13. N. Taniguchi, M. Kawasaki, Influence of sulphide concentration on the corrosion behavior of pure copper in synthetic seawater, *J. Nucl. Mater*. **379** (2008) 154–161.
14. J. Chen, Z. Qin, D.W. Shoesmith, Kinetics of Corrosion Film Growth on Copper in Neutral Chloride Solutions Containing Small Concentrations of Sulphide, *J. Electrochem. Soc*. **157** (2010) C338-C345.
15. J. Smith, Z. Qin, F. King, L. Werme, D. Shoesmith, Sulphide film formation on copper under electrochemical and natural corrosion conditions, *Corrosion*. **63** (2007) 135–144.
16. B. Rosborg, T. Kosec, A. Kranjc, J. Pan, A. Legat, Electrochemical impedance spectroscopy of pure copper exposed in bentonite under oxic conditions, *Electrochim. Acta*. **56** (2011) 7862–7870.
17. D. D. Macdonald, B. Kurstenc, and G. R. Engelhardt, *ECS Transactions*, 50 (31) 457-468 (2013).
18. C.O. Li, W. Lawamwisut, J.J. Zheng and W, Kijawatworawet, *International Journal of Materials & Structural Reliability*, V. 3 pp. 87-94 (2005).

2014:57

The Swedish Radiation Safety Authority has a comprehensive responsibility to ensure that society is safe from the effects of radiation. The Authority works to achieve radiation safety in a number of areas: nuclear power, medical care as well as commercial products and services. The Authority also works to achieve protection from natural radiation and to increase the level of radiation safety internationally.

The Swedish Radiation Safety Authority works proactively and preventively to protect people and the environment from the harmful effects of radiation, now and in the future. The Authority issues regulations and supervises compliance, while also supporting research, providing training and information, and issuing advice. Often, activities involving radiation require licences issued by the Authority. The Swedish Radiation Safety Authority maintains emergency preparedness around the clock with the aim of limiting the aftermath of radiation accidents and the unintentional spreading of radioactive substances. The Authority participates in international co-operation in order to promote radiation safety and finances projects aiming to raise the level of radiation safety in certain Eastern European countries.

The Authority reports to the Ministry of the Environment and has around 315 employees with competencies in the fields of engineering, natural and behavioural sciences, law, economics and communications. We have received quality, environmental and working environment certification.

Strålsäkerhetsmyndigheten
Swedish Radiation Safety Authority

SE-171 16 Stockholm
Solna strandväg 96

Tel: +46 8 799 40 00
Fax: +46 8 799 40 10

E-mail: registrator@ssm.se
Web: stralsakerhetsmyndigheten.se